Discrete Analysis of the Role of Pore Fluids in the Genesis of Opening Mode Fractures in the Shallow Crust

by

David Francis Boutt

Submitted in Partial Fulfillment

of the Requirements for the Degree of

Doctor of Philosophy in Earth and Environmental Science

with Dissertation in Hydrology

New Mexico Institute of Mining and Technology

Socorro, New Mexico

May, 2004

ABSTRACT

The work presented in this dissertation focuses on specific problems of coupled fluid-solid mechanics in porous media. These types of problems have been studied for many years with continuum methods. Continuum methods yield information about the behavior of systems but rarely provide significant insight into underlying physics. The work presented here is a departure from continuum methods and explores the application of discrete physics to coupled fluid-solid mechanics in porous media. I use these discrete methods to examine the behavior of both dry and fluid saturated rock. My specific interest is in identifying the role of fluids in the genesis of natural hydraulic fractures (NHFs) in the subsurface.

Much debate exists over the importance of NHFs, with a considerable amount of effort devoted towards understanding the conditions under which they form. The goal of this dissertation was to explore what control fluids and hydrologic properties of rocks exert on the initiation and propagation of opening mode fractures. I present porous media analyses using the coupled fluid-solid mechanics code LBDEM. Novel comparisons to classic poroelasticity problems (such phenomena as pressurization from an applied stress) indicate that this approach captures the essential physics. The LBDEM is used to explore the

detailed physics of natural hydraulic fracturing, through the conceptualization of laboratory experiment. Results of the tests indicate that fluid permeability and porosity either inhibit or prohibit the intensity of fracturing depending on the magnitude of each. Heterogeneities pore throat size (local fluid permeability) are considered, and are shown to increase the formation of fractures where pore throats are increased relative to the surrounding matrix. The experimental approach I developed is subsequently shown to produce fluid-induced extension fractures. For a bedding perpendicular sample of the Abo formation, one large macroscopic fracture and many microscopic extension fractures were formed. These results indicate that hydrologic heterogeneities, which cause pore fluid pressure gradients, are important for the genesis of natural hydraulic fractures. This implies that rocks with different hydraulic diffusivities will exhibit unique mechanical behavior under similar stress conditions, as rocks with lower diffusivity can maintain higher pore fluid pressure.

TABLE OF CONTENTS

LIST OF TABLES viii

LIST OF FIGURES ix

1. INTRODUCTION 1

1.1 Coupled Processes in Hydrogeology 3

1.1.1 Linear Poroelasticity 5

1.2 Effects of Crustal Deformation on Fluid Flow 7

1.3 Effects of Fluid Pressure on Crustal Mechanics 9

1.4 Literature Review 12

1.4.1 Genesis and Propagation of Fractures 15

1.4.2 Natural Hydraulic Fractures 20

1.4.3 Pore Pressure Gradients 23

1.5 Modeling of Coupled Fluid-Solid Mechanics 25

1.5.1 Discrete Element Method 25

1.5.2 Lattice-Boltzmann and Coupled Model Theory 26

1.5.3 Previously Used Techniques 27

1.6 Relationships between Micromechanical Properties and Macroscopic Concepts 29

1.6.1 Porosity 30

1.6.2 Permeability 30

1.6.3 Storage Capacity and Hydraulic Diffusivity 31

1.7 Purpose, Goals, and Scope 32
1.8 Organization of this Dissertation 35

2. SIMULATION OF SEDIMENTARY ROCK DEFORMATION: LAB-SCALE MODEL CALIBRATION AND PARAMETERIZATION 47

Abstract 47
2.1 Introduction 48
2.2 Modeling Approach 49
2.2.1 Limitations of Previous DEM Studies 49
2.2.2 Selection of Parameters to Calibrate 49
2.2.3 Methods 50
2.3 Results and Discussion 53
2.3.1 General Relationships Among Microparameters and Macroparameters 53
2.3.2 Calibration of Failure Mode 55
2.3.3 Strength Envelopes 58
2.3.4 Stress-Strain Curves 58
2.4 Conclusions 60

3. APPLICATION OF DISCRETE ELEMENT MODELING TO UNDERSTANDING THE FORMATION OF SHEAR FRACTURES IN THE SPRABERRY TREND, MIDLAND BASIN 66

Abstract 66
3.1 Introduction 67
3.2 Geologic Setting and Background 69

3.2.1 Observed Fractures 70
3.2.2 Possible Fracture Mechanism 72
3.3 Role of Laramide Compression in Fracture Formation 73
3.3.1 DEM Model of Laramide Compression 74
3.3.2 Fracture Variability: DEM Model Simulations 77
3.4 Conclusions 84

4. NUMERICAL MODELING OF COUPLED FLUID-SOLID MECHANICS: MODEL PROPERTIES AND LIMITATIONS 91

4.1 Introduction 91
4.2 Modeling Approach 92
4.2.1 Discrete Element Method 92
4.2.2 Coupled Model Theory 93
4.3 Why Navier-Stokes and the LBDEM technique? 97
4.4 Model Boundary Conditions 99
4.4.1 Pressure Boundary Condition 99
4.4.2 No Slip 100
4.5 Model Properties 100
4.5.1 Grid Resolution 103
4.5.2 Relaxation Time 104
4.5.3 Computational Mach Number 106
4.5.4 Fluid Compressibility 109

5. NUMERICAL INVESTIGATION OF THE MICROMECHANICS OF FLUID SATURATED ROCKS **117**

Abstract 117

5.1 Introduction 118

5.2 Fluid-solid Coupling in Porous Media 120

5.3 Modeling Approach 123

5.3.1 Discrete Element Method 123

5.3.2 Coupled Model Theory 124

5.3.3 LB Boundary Conditions 125

5.3.4 Model Two-Dimensionality 126

5.4 Fluid Flow Through Periodic Arrays of Cylinders 126

5.4.1 Low Reynolds Number Flows 127

5.4.2 High Reynolds Number Flows 129

5.5 Steady Flow Through Stationary Porous Media 131

5.5.1 Darcy's Law 132

5.5.2 Porosity-Permeability Relationships 132

5.6 Unsteady Flow Through Non-Stationary Media 134

5.6.1 Fluid Flow in Slightly Compressible Porous Media 136

5.6.2 Transient Fluid Flow Through Porous Media With LB-DEM Model 139

5.6.3 Conceptual Model of 1-D Consolidation 142

5.6.4 Results of 1-D consolidation With LBDEM Model 145

5.7 Conclusions 151

5.A Appendix: Lattice-Boltzmann and Coupled Model Theory (excerpted with permission from *Cook* [2001] 154

6. NUMERICAL AND EXPERIMENTAL INVESTIGATION OF THE ROLE OF FLUID PRESSURE GRADIENTS IN FRACTURE GENESIS 163

Abstract . . . 163

6.1 Introduction . . . 164

6.2 Previous Work . . . 165

6.3 Theory of Natural Hydraulic Fracturing . . . 168

6.3.1 Fluid Pressure and Confining Stresses . . . 169

6.3.2 Fluid Pressure Gradients and Drag Forces . . . 175

6.4 Numerical Test Design . . . 177

6.5 Modeling Approach . . . 180

6.5.1 Discrete Element Method . . . 180

6.5.2 Lattice-Boltzmann and Coupled Model Theory . . . 181

6.6 LBDEM Conceptual Model . . . 182

6.7 Fluid-Induced Fracture Results . . . 185

6.7.1 Fracture Initiation . . . 188

6.7.2 Fracture Propagation . . . 190

6.8 Role of Rock Permeability . . . 192

6.8.1 Hydrologic Heterogeneity . . . 199

6.9 Experimental Demonstration of Numerical Simulations . . . 202

6.9.1 Sample Characteristics . . . 204

6.9.2 Experimental Setup . . . 206

6.9.3 Testing Results . . . 207

6.10 Discussion . . . 211

6.11 Conclusions . . . 215

7. CONCLUSIONS AND RECOMMENDATIONS 224

7.1 Conclusions 224

7.1.1 Contributions to the Scientific Community 226

7.2 Limitations and Future Work 231

7.2.1 Limitations 231

7.2.2 Future Work 234

LIST OF TABLES

1.1 Summary of previously used coupling techniques 28

2.1 Input Microparameters for DEM Models. Parameters notation is consistent with the notation of *Potyondy and Cundall* [In Press] to allow for comparison. 54

3.1 Elastic and in-elastic data for units used in the 1-layer and 3-layer models. 77

4.1 Parameters of fluid compressibility simulations 111

5.1 Summary of previously used coupling techniques 122

5.2 Parameters for transient fluid flow and consolidation problem. . 139

5.3 Fluid wave speeds for simulated fluid and real fluids (at STP) . 147

6.1 Parameters of Solid Assembly 184

6.2 Parameters of Fluid Lattice 184

6.3 Properties of models used for permeability sensitivity study . . . 194

LIST OF FIGURES

1.1 Coupled processes in hydrogeology, adapted from *Yow and Hunt* [2002]. 4

1.2 Observed fluid pressure-depth profile in Altamont field, Uinta Basin, Utah (adapted from *Bredehoeft et al.* [1994]). Shown for reference is a freshwater hydrostatic pressure profile (dashed line). This specific plot of fluid pressure vs. depth is probably not a direct result of sediment compaction, but may be more related to oil and gas generation, another source of hydrodynamic disequilibria that is not related to hydromechanical coupling. This illustrates the magnitude of fluid over-pressures observed in the field. 8

1.3 Selected research dealing with fracture formation and propagation in the presence of elevated fluid pressure 13

1.4 Three fundamental modes of fractures. Mode I - tensile, Mode II - in-plane shear, Mode III - anti-plane shear 16

1.5 A mode I fracture of length $2a$ loaded by a remote compressive stress (σ_3) and fluid pressure (p). 17

1.6 Plots of normalized fracture half-length (with respect to initial flaw length) versus dimensionless time show that rocks with higher ratios (ϕ) of amount of fluid required to sustain propagation (i.e., the change in area of the fracture per unit extension) to amount of fluid readily available (i.e., matrix storage) have fractures that grow slower. From *Renshaw and Harvey* [1994]. . 21

1.7 Deviation of fracture induced by pore pressure gradient. Adapted from *Bruno and Nakagawa* [1991]. 23

2.1 A histogram of the distribution of cluster sizes in a 3 cluster model indicates that not all of the clusters are 3 large. A small number of 2 clusters and single elements are present. 54

2.2 Time series of displacement gradients (see text) for sample 5U-4 at 0 MPa confining pressure. The localization in the modeled sample evolves from a distributed mode (darker colors) with very little deformation to a highly localized deformation (lighter colors) just after peak stress. This zone is approximately 4 particles wide. 57

2.3 Simulated and observed compressive failure envelopes for 4 different groups of sedimentary rocks from the Midland Basin. Failure envelopes were determined by plotting peak stress at the given confining pressure. A good match is achieved through adjusting the main parameters controlling the slope of the compressive failure envelope, particle friction (0.5 in all models) and cluster size. Note the difference in slope between the unclustered material and the models in this study. 59

2.4 Simulated and observed differential stress and volumetric strain versus axial strain curves for sample 5U-4. Solid lines represent observed laboratory data at the confining pressure marked on the plot and dashed lines represent simulations. Differences in the position of the curves along the x axis are due to a choice in elastic parameter calibration (intrinsic versus damaged rock properties). The general trends in the curves are captured. . . . 61

3.1 Structure contour map of upper Spraberry Formation, (right; from *Bai* [1989]) illustrating the relatively simple structure of the area. Location of contour map area shown on map of Texas (left). Shown on the contour map are fracture orientations (determined by *Bai* [1989]); shown on the map of Texas are major horizontal compressive stress orientations (from *Zoback and Zoback* [1989]). Outline of Spraberry trend shown in center schematic. Also shown on center schematic is the location of the cross-section A-A'. 71

3.2 Rose diagram showing the trends of observed fracture sets in the Spraberry Formation. 72

3.3 Results of the 5U simulation plus boundary conditions. Spraberry Formation strata consist of thin reservoir sands surrounded by thicker fine grained silts and shales. Resultant displacement gradient contours of the 5U model show significant deformation. It is possible that the properties of the surrounding units may influence how individual units behave mechanically. 78

3.4 DEM simulation results. (A) Cumulative particle displacements and associated displacement vectors, (B) spatial displacement gradients, (C) residual displacement gradients of middle layer. . 81

3.5 Stress perpendicular to loading v.s. simulation time for assemblies composed of the stated percentages of 1U and 5U units. The different percentages of the units tend to lower the affect both the strength of the unit and the timing of failure. 83

4.1 The coupling between lattice-Boltzmann and DEM is a function of both element location and velocity. Resulting forces from the fluid are applied to the solid and integrated for new position and velocity. 94

4.2 Convergence from an initial condition of rest towards steady state for velocity and pressure using pressure boundary condition of *Zou and He* [1997] compared to an analytical solution for steady-state Poiseuille flow. The top gives the density difference and the bottom plot shows the relative flux difference. 101

4.3 The mean velocity error associated with increasing density differences along channel is significantly higher. The points, connected by straight lines, represent the actual error between the simulation and the analytical solution for Poiseuille flow. 102

4.4 Problem space and analytical solution for Poiseuille flow. Comparisons of model results were made to this solution. 103

4.5 Comparisons of LB solutions (stars) to analytical solutions (lines) for 3, 4, 5, and 37 nodes in the channel. These errors allow the determination of the required number of nodes for numerically accurate resolution of flow. 105

4.6 A log-log plot of error vs. number of nodes shows roughly first order numerical convergence. The influence of relaxation time, τ^*, on relative flux error is relatively small, but observable. . . 106

4.7 The relative flux error for Poiseuille flow increases as the Mach number squared. It is important that this number be small (i.e. much less than 1.0). A computational Mach number greater than one implies that fluid velocity is traveling faster than the method can transfer information causing instability. 107

4.8 Conceptual model (left) and screenshot (right) of fluid compressibility problem. The screenshot depicts the platens and a filled contour plot of fluid pressure at early time. 111

4.9 In LBDEM, a constant stress boundary condition is used to determine parameters defining the fluid compressibility. As a result of an applied stress, a volume of fluid will come to equilibrium as the fluid resists a change in volume. The corresponding density change yields information about how the fluid responds to changes in pressure. 112

4.10 When a stress is applied to a volume of compressible fluid, a corresponding density change takes place. In the LBDEM, the velocity of the fluid accelerates until an equilibrium condition is reached. At late times the fluid density curve is the upper curve and the fluid velocity curve is the lower. 113

5.1 The coupling between lattice-Boltzmann and DEM is a function of both element location, velocity, and rotation. Resulting forces from the fluid are applied to the solid and integrated for new position and velocity. 125

5.2 Dimensionless drag vs. solid concentration for low Reynolds flow around a periodic array of cylinders for solid concentrations ranging from 0.2 to 0.6. As solid concentration increases so does the drag on the cylinder. 128

5.3 Qualitative comparison of pressure contours at a solid concentration of 0.5 for FEM results of *Edwards et al.* [1990] and our LBDEM results. A good match between the two solutions is achieved. 129

5.4 Dimensionless pressure drop vs. Reynolds number for flow around a periodic array of cylinders for a solid concentrations of 0.5. As the Reynolds number increases, the pressure drop decreases, as viscous dissipation is lessened. 131

5.5 (a) Fluid flow through a finite number of stationary cylinders showing the acceleration and deceleration of fluid through pore throats. (b) A plot of volumetric flux vs. pressure gradient shows a linear relationship, as predicted by Darcy's law. 133

5.6 Permeability-Porosity relationships for simple models show a good match to what is predicted via Kozeny-Carmen theory. . . 135

5.7 Conceptual model for 1-D fluid flow problem through non-stationary media. Line A to A' indicates cross-section depicted in Figure 5.8. 138

5.8 The solid ratios along cross-section A-A' in Figure 5.7. An averaging scheme was used such that only completely fluid-filled nodes are analyzed. Gray filled areas are solids. 141

5.9 Plots of normalized pressure vs. distance for the LBDEM solution are shown as different symbols for eight times during the simulation. Also plotted are the analytical solutions (solid lines) at the same times using a diffusivity of $7.9\frac{cm2}{s}$. Inset: Sum of least squares of diffusivity for model results. 143

5.10 Analytical solution and LBDEM solution for Terzaghi's consolidation problem. Analytical solution assumes ideal poroelastic response therefore solutions are not identical. 145

5.11 Conceptual model for consolidation problem. Top boundary condition is drained and held at constant fluid pressure. 146

5.12 The sensitivity of the time for the fluid pressure to reach its peak value is a function of the solid wave speed. With small changes in element stiffness, the time to reach the peak fluid pressure in the system is much smaller. 149

5.13 The time for the fluid pressure to reach its peak value is much less sensitive to fluid wave speed than solid wave speed. Relative to the solid wave speed sensitivity, the time quickly levels out and fluid speeds well below that of water can approximate this response well. 150

5.14 Additional data from the consolidation test can give insight into the physics of the coupled system. Shown here are contact forces (A) and fluid speeds (B) for the consolidation test. Normal contact forces are depicted as thick lines parallel to contact normal. Higher fluid velocities are represented as brighter contours that converge on the draining boundary. 152

6.1 Plots of normalized fracture half-length (with respect to initial flaw length) versus dimensionless time show that rocks with higher ratios (ϕ) of amount of fluid required to sustain propagation (the change in area of the fracture per unit extension) to amount of fluid readily available (matrix storage) have fractures that grow slower. From *Renshaw and Harvey* [1994]. 166

6.2 Deviation of fracture induced by pore pressure gradient. Adapted from *Bruno and Nakagawa* [1991]. 167

6.3 Schematic of commonly used conditions to evaluate the likelihood of natural fracturing in sedimentary basins. These conditions assume a very long basin relative to it's height with no applied confining stress and minimum stress only a result of the vertical load. On left hand side of the figure are the assumed pore pressure (dotted line) and stress (solid line) vs. depth curves. No horizontal flow is allowed. 170

6.4 The least minimum stress (σ_3) in a tectonically relaxed basin is a strong function of σ_1 and fluid pressure. Poroelastic effects severely influence the resulting effective stress distribution (σ_3^*). This is shown for values of ν and α as a function of fluid pressure using Equation (6.7). Critical fluid pressure values, where effective stress = 0, are the same for all ν. 172

6.5 Plots illustrating the effect of fluid pressure on confining stress in a tectonically relaxed basin. Contours are results of solving Equation (6.7) neglecting the last term. This reduces the critical fluid pressure needed to drop effective stress (σ_3^*) to 0. 174

6.6 Initial and boundary conditions for experimental approach to generating natural hydraulic fractures. Fluid pressure in the system is kept elevated relative to the minimum stress by the lag time that occurs as a result of fluid flow (pressure gradients). 179

6.7 Base discrete element model for all fracture simulations. Roughly 1,000 ellipse-shaped elements were packed into a 7 by 3.5 cm area. 183

6.8 Time series of fracture initiation and propagation under realistic laboratory boundary conditions show a complex evolution of the model. In this and all models presented in this section, element color is % bonds broken and color shading behind elements is fluid pressure. 187

6.9 Time series of particle speeds (hot element colors indicate higher speed) illustrating fracture development as the simulation progresses. Outer blocks are moving at higher rates than inner blocks. 188

6.10 Element long axes are plotted in a rose diagram to visualize trends. The numbers correspond to the quantity of elements with the indicated orientation This preferred orientation of elements is coincident with the orientation of some of the major fractures in the model. 189

6.11 Pre- and post-bond (shaded particles) breakage is illustrated (top images) for a pair of particles in the central portion of the assembly. In the bottom images velocity magnitudes (dark shading is low velocity) and velocity vectors indicate a bulk extensional loading on the assembly. The bottom images are of the same region indicated in the top image, but blown up to show vectors more cleary. 191

6.12 Contact forces and fluid-induced forces for two particles central to the model (See Figure 6.11) are shown here. After initial bond breakage, local fluid pressure in the fracture is lower, giving rise to fluid pressure gradients that are towards the fracture. Fluid loading on the assembly appears to be responsible for further fracture propagation. 193

6.13 Results of fracturing simulations for $k = 1.2E-4cm^2$ (top) and $k = 7E-5cm^2$ (bottom) permeability models. Contoured fluid pressure results are also plotted on axes of time vs. distance for a stationary line along the center of the each model domain. In the center of each figure is a screenshot of the model state at 0.2 s. To the right of the screenshots is a filled contoured plot of fluid speed on axes of time vs. distance along the same centerline. All plots are scaled to the same ranges in order to compare differences between models. 196

6.14 Results of fracturing simulations for $k = 2.39E-5cm^2$ (top) and $k = 1E-6cm^2$ (bottom) permeability models. In the center of each figure is a screenshot of the model state at 0.2 s. Contoured fluid pressure results are also plotted on axes of time vs. distance for a stationary line along the center of the each model domain. To the right of the screenshots is a filled contoured plot of fluid speed on axes of time vs. distance along the same centerline. All plots are scaled to the same ranges in order to compare differences between models. 197

6.15 Interpretation of fractures for the permeability sensitivity study. Colors correspond to models with different permeabilities, 1 the highest and 4 the lowest. The thickest solid lines indicate large open fractures, whereas thin solid and dashed lines indicate smaller and minor fractures respectively. 199

6.16 Results from increasing the pore throat size relative to the matrix. Black lines indicate the location of changes in pore throat size, where from left to right the lines enclose the changes. Models with imposed heterogeneities have similar porosities. Large differences between the "homogeneous" and heterogeneous models are evident. See text for further discussion. 201

6.17 Results from decreasing the pore throat size relative to the matrix. Models with imposed heterogeneity have similar porosities. Very small differences in fracture patterns between the models are observed. See text for further discussion. 203

6.18 A log-log plot of sample time constants and fluid permeability defines the lower limit in which the stress on the rock can be removed. Four curves are shown here, each for a unique fluid viscosity. The lowermost curve is for that of water and the upper curves are for a viscosity of 10x, 100x, and 1000x of water. The solid line at 1 second is the assumed response time of the laboratory equipment. 205

6.19 The endcaps used in the extension tests are able to support differential stresses, such that the maximum stress is the confining stress. Total assembly height is approximately 20 inches tall. . . 207

6.20 Pressure vessel and load frame used for generating hydraulic fractures. Tubing on right hand side allows for the simultaneous dropping of fluid pressure at top and bottom end caps. 208

6.21 A plot of percent axial strain vs. axial stress for a dry extensional test. A small amount of elastic strain takes place as the axial stress is dropped. Arrows indicate unloading and reloading of the speciment. A small amount of hysteresis is observed. 208

6.22 A plot of pore pressure, confining pressure, and axial stress, vs. time shows the relative timing of dropping the fluid pressure and the axial stress. Two prominent increases in axial stress after the start of the test mark the extensional fracturing and the slippage of a major extension fracture. A dip in the confining stress is coincident with the slippage due to perturbation of the confining fluid. 209

6.23 As the sample is unloaded, measurable extension (negative strain) of the rock occurs. The strain in the fluid saturated test is 4 times greater than the dry test. A sharp increase in the axial stress marks the time where the extension fractures were formed. 210

6.24 Generation of a shear fracture along a pre-existing extension fracture is the result of the angle of the extension fracture. The slip on the fracture is limited by the amount of stretching in the jacket of the specimen. 212

6.25 As the rock is relieved of axial load, the rock compresses in the lateral direction. This plot of axial stress vs. lateral strain shows this relationship. The fracturing of the sample cause local changes in the amount of compression. 212

6.26 Large numbers of extension fractures are observed parallel to bedding and sub-parallel to the fluid pressure gradient. Thin section analysis will be used to quantify the number of fractures in the future. 213

CHAPTER 1

INTRODUCTION

The coupling between fluid flow and deformation of rocks and sediments is a key component of many fundamental processes in the Earth's shallow crust. The effects of this hydromechanical coupling are ubiquitous in geology and hydrogeology. Examples include deposition and erosion, faulting and earthquakes, earth tides, and barometric loading, all of which induce local rock strain that may alter fluid pressure. Fluid pressure changes as a result of the above processes affect hydrodynamics and sometimes cause extreme pressure anomalies [*Neuzil*, 1995; *Bredehoeft et al.*, 1994] that can occur over a vast range of spatial and temporal scales. This coupling is also relevant to many significant societal problems, from subsidence and other effects of mining groundwater supplies [*Galloway et al.*, 2000] to the mitigation of earthquake hazards (San Andreas Fault Observatory at Depth). The attention of the scientific community to these issues is increasing as evidenced by recent issues of scientific journals dedicated to this specific subject (see *Kumpel* [2003]; *Stephansson* [2003]).

Fluid pressure has been found to offset crustal stresses and affect mechanical processes at depth. The concept of fluid pressure offsetting total stress was first applied to geological problems by *Hubbert and Rubey* [1959]. This concept, usually called effective stress, was first studied by *Terzaghi* [1925], and

forms the foundation of our understanding of mechanical interactions between fluid pressure and solid. *Biot* [1941] applied this concept together with theory from solid mechanics and groundwater flow to form the basis of the field of linear poroelasticity. The last 80 years produced significant advances in our understanding of these couplings, leading to theories of consolidation and transient groundwater flow. It has since been shown that fluid pressure plays a large role in the behavior of almost all mechanical processes in the shallow crust. The importance of these fundamental theories is paramount; however it is difficult to apply them to realistic field problems due to our inability to characterize and conceptualize real systems. Despite this acknowledged role of fluid pressure in crustal rock mechanics, we still have only limited understanding of the complete coupling between rock deformation and fluid flow.

This dissertation examines the pore-scale hydromechanical system where strong deformations not only change fluid permeability but fluid may also change the state of stress within the deforming rock matrix. Specifically, I examine the case of opening mode fractures (or joints) that are driven by elevated fluid pressure. The formation of fractures is theorized to influence mechanical and hydrologic behavior within sedimentary basins. I have used a coupled discrete model of deformation and fluid flow to simulate the complex hydromechanical system represented by a porous sedimentary rock subjected to differential stress. Corresponding deformation experiments help elucidate the role of fluid flow properties (such as fluid permeability and storage) in a system undergoing deformation. This study attempts to fill a void in the literature, addressing fluid flow and pressure in the process of fracturing. The results of this study are important for researchers who are concerned with the

distribution, orientation, and physical properties of opening mode fractures in addition to understanding the fundamental feedbacks between solid mechanics and fluid flow.

1.1 Coupled Processes in Hydrogeology

Coupled processes in geology commonly involve strongly nonlinear relationships among state variables (e.g., fluid pressure and temperature) and their associated dependencies on rock properties. For example, fluid permeability (k) in a porous medium relates fluid flux (q) and fluid pressure (p) through

$$q = -\frac{k(\sigma)}{\mu} \left(\nabla p + \rho g \nabla z \right), \tag{1.1}$$

where μ is fluid viscosity, ρ is fluid density, and g is gravity, z is elevation with respect to a datum, and ∇ is the gradient operator. Here k can be a function of stress (σ). In addition

$$\sigma' = \sigma - p, \tag{1.2}$$

where σ' is effective stress, suggests that the stress acting on a plane is offset and hence coupled to the fluid pressure (see Section 1.3 for more). This is a very simple example of a coupling between fluid flux and the stress state in the rock where $k(\sigma)$ can be linear or extremely non-linear. Equation (1.1) does not, however, express the degree of coupling.

Relations between the various state variables in a geologic system can be quite complex (Figure 1.1). However, information about the coupling between the thermal and hydrologic aspects of a system may be used to infer properties about its mechanical state. A prime example of this is given by *Saffer*

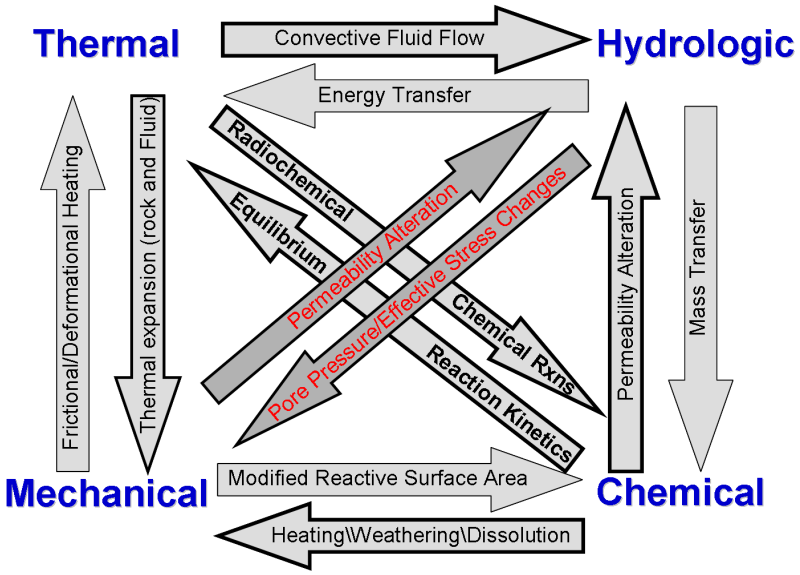

Figure 1.1: Coupled processes in hydrogeology, adapted from *Yow and Hunt* [2002].

et al. [2003], who evaluated the mechanical properties of the San Andreas fault by studying its thermal response to and perturbation by fluid flow. This type of analysis is only possible if a detailed understanding of the coupling or feedback loop between the two state variables is known. This dissertation focuses on the feedback loop between hydrologic and mechanical properties, in an attempt to elucidate a more detailed understanding of the coupling in systems with elevated fluid pressure.

The coupling between the hydrologic and the mechanical processes may be examined in two arbitrary ways: 1) the lone effect of fluid pressure on the mechanical response (effective stress) and 2) the effects of mechanics (strain and stress) on the hydrologic response, especially via permeability modification. Both of these coupling pathways can be equally important. However, one or

both are often ignored; many conditions or situations call for simplification in the form of neglecting one 'direction' of this coupling. For example, one of the assumptions in the development of the transient groundwater flow equation is that deformations are small and reversible (i.e., elastic deformation), and permeability remains unaltered. Numerical models and analytical solutions can aid in the analysis of the importance of the competing hydromechanical effects. One framework used for this analysis is the theory of linear poroelasticity.

1.1.1 Linear Poroelasticity

The theory of linear poroelasticity brings together concepts from solid mechanics and fluid flow through porous media [*Biot*, 1941]. Coupling between the equations of fluid diffusion (Equation (1.3)) and mechanical equilibrium (Equation (1.4)) is explicit because pore pressure (or more formally, increment of fluid content, ζ) appears in the force equilibrium equations, and because mean stress (or volumetric strain) appears in the fluid-flow equation [*Wang*, 2000]. The following equations describe the fully coupled stress and fluid flow behavior of a porous medium.

$$S_\sigma \left[\frac{B}{3} \frac{\partial \sigma_{kk}}{\partial t} + \frac{\partial p_{ex}}{\partial t} \right] = \frac{1}{\mu} \nabla \cdot \underline{\underline{k}} \nabla p_{ex}, \tag{1.3}$$

and

$$\nabla^2 \left(\sigma_{kk} - 4\eta p_{ex} \right) = -\frac{1+\nu}{1-\nu} \nabla \cdot \vec{F}, \tag{1.4}$$

where :

S_σ = three dimensional specific storage

B = Skempton's coefficient

σ_{kk} = mean stress

p_{ex} = pore pressure in excess of hydrostatic

μ = fluid viscosity

$\underline{\underline{k}}$ = permeability tensor

η = poroelastic stress coefficient

ν = drained Poisson's Ratio

$\vec{F}$ = body force per unit bulk volume.

The diffusion equation (Equation (1.3)) for pore pressure is called inhomogeneous because it includes changes in mean stress with time. The time-dependent mean stress term is mathematically equivalent to a fluid source whereas the fluid pressure gradient term in Equation (1.4) is equivalent to a body force. The mechanical problem is elasto-static, which means that static equilibrium is achieved for each instant of time. In reality, a finite amount of time is required for a stress wave to transmit changes across the problem domain, but the wave propagation term is ignored. If a stress or fluid pressure change is applied suddenly to a poroelastic body, local displacements and pore pressure adjust instantaneously to accommodate the change and maintain a state of internal force equilibrium. Subsequent time-dependent fluid diffusion occurs as a result of the delaying effects of finite permeability and storage.

In the absence of coupling to fluid flow, the stress or mechanical equilibrium equations will be time independent. This fact is extremely important when treating the fluids in the Earths crust as dynamic [*Bredehoeft et al.*, 1994]. If fluid is considered to be static [*Bradley*, 1975], then flow is instantaneous and the pressure in these "static compartments" reaches a constant value. This assumption is inherent in rock mechanics analyses in which no information about the spatial distribution of fluid pressure is available. The following two sections give examples of geologically relevant hydromechanical interactions.

1.2 Effects of Crustal Deformation on Fluid Flow

The most fundamental effect of deformation on fluid flow is to change porosity or the space available for fluid, through volumetric strain of the rock. Two aspects of this porosity change determine the behavior of the system of interest. One is the rate at which the change takes place and the other is the resulting spatial distribution of the change. Where porosity changes are slow enough for fluid to equilibrate with the new conditions (drained response), no changes in fluid pressure should be observed. But, as a consequence of the porosity change, the permeability of the rock will be altered. The permeability alteration will impact subsequent fluid flow paths. If porosity change is fast enough (undrained response), fluid pressure will rise due to the fluid compressibility. *Neuzil* [1995] showed that significant fluid pressure anomalies are generated and maintained when

$$\dot{\varepsilon}_{kk} > \frac{K}{l}, \tag{1.5}$$

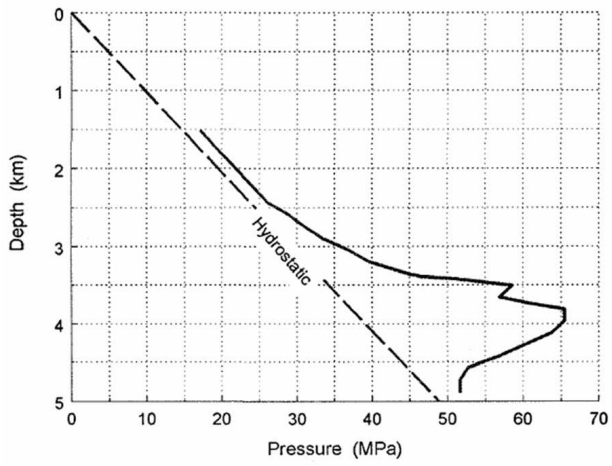

Figure 1.2: Observed fluid pressure-depth profile in Altamont field, Uinta Basin, Utah (adapted from *Bredehoeft et al.* [1994]). Shown for reference is a freshwater hydrostatic pressure profile (dashed line). This specific plot of fluid pressure vs. depth is probably not a direct result of sediment compaction, but may be more related to oil and gas generation, another source of hydrodynamic disequilibria that is not related to hydromechanical coupling. This illustrates the magnitude of fluid over-pressures observed in the field.

where $\dot{\varepsilon}_{kk}$ is the volumetric strain rate, K is the hydraulic conductivity, and l is the distance from the center of the domain to the boundaries.

Geologic processes induce strain (porosity change) at a variety of spatial and temporal scales. Many of these processes also induce hydrodynamic disequilibria, such as sediment compaction, erosional decompaction, tectonic deformation, barometric and earth tides, creep and seismic slip along faults, and magmatic intrusion. Fluid pressure changes can be dramatic relative to the hydrostatic (Figure 1.2). Compactive strain typically induces the largest and most widespread disequilibria, although local changes due to creep and seismic slip along faults can also be very large. In tectonically active regions, such

as accrectionary prisms, fluid flow is almost solely driven by tectonic strain. Simulations by *Saffer and Bekins* [2002] of accretionary prisms showed that thrusting directly causes high fluid pressure. This is in stark contrast to fluid flow in shallow basin sediments, which is usually driven by topography. Barometric and earth tide forcings can typically cause very minute changes in fluid pressure, but these changes are important in that they can be used to infer the hydrologic properties (such as storage) of the aquifer itself.

1.3 Effects of Fluid Pressure on Crustal Mechanics

Fluids exert a strong control on the mechanics of the crust. From a static perspective, fluids in the crust bear part of applied loads. Rock matrix is subjected to a smaller load than if the fluid were absent. Karl Terzaghi first discovered this phenomenon when researching consolidation of soils and termed the resulting stress an "effective" stress. An increase in applied tensional stress expands a rock by about the same amount as an equal increase in pore pressure. Similarly, equal changes in applied compressive stress and pore pressure tend to offset each other, indicating the strong effect of fluid pressure on both stress and strain of rocks.

Effective stress for a rock can be defined by tensor components σ'_{ij},

$$\sigma'_{ij} = \sigma_{ij} - \alpha p \delta_{ij}, \tag{1.6}$$

where σ_{ij} are stress components (a positive stress is compressive, using the geologists convention), α is the Biot-Willis coefficient, p is pore fluid pressure (positive is an increase in pressure), and δ_{ij} is the Kronecker delta. Pore pressure

only affects the normal stress terms, and not the shear stress, because shear stresses do not produce volumetric strains (hence the use of the Kronecker delta). The Biot-Willis coefficient is a measure of the efficiency with which pore pressure counteracts confining pressure to produce volumetric strain. The coefficient is commonly assumed to be equal to 1, as Terzaghi first assumed, but *Berryman* [1992], in work involving the Gassman equations, suggested a range for the Biot-Willis coefficient that is less than or equal to 1 depending on the rock type. Experiments on granites, sandstones, and other rocks [*Detournay and Cheng*, 1993] show that the Biot-Willis coefficient varies from 0.23 (Hanford basalt) to 0.83 (Pecos sandstone). These results suggest that this coefficient may also vary with the deformation state (fractured or unfractured) of the material. There is much debate over the validity and applicability of this concept [*Warpinski and Tuefel*, 1992].

Fluid pressure that is elevated relative to hydrostatic, regardless of cause, will offset some of the rock framework stress. For example, high pressure commonly occurs where sediments are buried in a basin with a high deposition rate. If the rate of burial-induced strain is faster than the rate of fluid flow out of the system, the fluid pressure will increase, eventually resulting in a rock framework that is under-consolidated with respect to ambient lithostatic load. This phenomenon typically leads to higher than predicted porosity with depth, commonly called compaction disequilibrium. High fluid pressure can also play a role in the shear failure of rocks. Since fluid pressure can offset normal stress, elevated fluid pressure can induce failure and/or slippage on pre-existing discontinuities. This concept forms the motivation and focus of this dissertation. *Hubbert and Rubey* [1959], in their classic paper on the mechanics

of thrust faulting, employed Terzaghi's effective stress principal to show that elevated fluid pressures facilitate movement of large thrust blocks. Finally, *Hsieh and Bredehoeft* [1981] demonstrated that fluid pressure increases and subsequent diffusion are responsible for seismicity near injection wells. These examples suggest a strong correlation between fluid pressure and the mechanical stability of rocks in the subsurface.

Fluid pressure is known to locally reach magnitudes equal to that of the far-feld minimum stress [*Breckels and Eekelen*, 1982; *Engelder*, 1993; *Engelder and Fischer*, 1994]. Injection of fluid at elevated pressure into boreholes are used to stimulate oil and gas reservoirs by locally creating fractures, which may increase permeability. Does a geologically equivalent process exist by which fractures are created naturally in the shallow crust, thereby increasing fluid permeability? In recent years a wealth of literature, using limited empirical failure criterion, has suggested that fluid pressure initiates and propagates fracture networks [*Tuncay et al.*, 2000; *LHeureux and Fowler*, 2000; *Payne et al.*, 2000; *McPherson and Bredehoeft*, 2001]. This draws on the work of *Secor* [1965] who explicitly linked rock jointing (mode-I fractures) to net tensile stresses created by high fluid pressure. *Secor* [1965] showed that if fluid pressure is greater than the least minimum stress (σ_3), the effective minimum stress (σ_3^*) becomes tensile, as shown through the following relation

$$\sigma_3^* = \sigma_3 - p. \tag{1.7}$$

Depending on the stress regime, depth, and tensile strength of the rock, it appears that overpressures are required for natural hydraulic fracturing to occur, due to the compressive state of the subsurface. Despite what is presented here,

little is known about the physics governing the intimate coupling between fluid flow and fracture growth under these conditions. This dissertation will examine the feasibility of this process and evaluate the conditions (fluid pressure, stress, and permeability) under which hydraulic fractures, or fluid-assisted fractures, can form.

1.4 Literature Review

Previous work on fracture initiation, propagation, and generation mechanisms has come from several fields including geology, mechanical and petroleum engineering, and hydrology. I lump these approaches into two broad but distinct categories: approaches that use empirical failure criteria and those that use classical Griffith crack theory [*Griffith*, 1921; *Irwin*, 1957], or what I will call crack-tip modeling (Figure 1.3).

Studies that use empirical failure criteria to determine whether rock will fracture, employ Mohr diagrams to analyze and interpret joints and fractures [e.g., *Muehlberger*, 1961; *Hancock*, 1985]. Although a Mohr diagram is a useful tool for exploring homogeneous stress fields, it does not account for the heterogeneous stress fields associated with a fracture [*Pollard and Aydin*, 1988]. A common assumption of empirical criterion studies is that fracture behavior depends only on rock mechanical properties and far-field driving forces [*Ramsay and Huber*, 1987]. Researchers typically incorporate pore pressure influences using the concept of effective stress, but rarely describe the movement of pore fluid itself. In most of these studies, pore pressures are homogeneously distributed, or uniform, throughout the domain of interest [*Fischer*, 1994; *Fischer et al.*, 1995; *McConaughy and Engelder*, 2001]. However, natural permeability

Research Focus	
Pre-Initiation (Conditions leading up to fracture initation)	Post-Initiation (Assuming Griffith cracks of some size)
References:	
Kinji, 1981	Secor, 1965
Narr and Currie, 1982	Secor, 1969
Rudnicki, 1985	Secor and Pollard, 1975
Miller, 1995	Segall and Pollard, 1983
Osborne, 1997	Segall, 1984
L'Heureux and Fowler, 2000	Engelder and Lacazette, 1990
Payne et al., 2000	Hegelson and Aydin, 1991
Tuncay et al., 2000	Lacazette and Engelder, 1992
Mcpherson and Bredehoft, 2001	Renshaw and Harvery, 1994
Merlani, 2001	Fischer et al., 1995
Simpson, 2001	McConaughy and Engelder, 2001

Figure 1.3: Selected research dealing with fracture formation and propagation in the presence of elevated fluid pressure

heterogeneity may cause large pore pressure gradients on the same spatial scale that effective stress concepts are thought to apply, e.g., at the scale of fracture tips. Pore pressure gradients may be used as a proxy for effective stress gradients, if a constant remote stress is assumed. Effective stress gradients serve to change the rock response, as indicated by classical poroelasticity theory [*Rice and Cleary*, 1976; *Rudnicki*, 1985], and hence may initiate or even arrest the propagation of a fracture. *Rock hydraulic parameters must also be considered because they control effective stress distributions.*

The other broad category of fracture studies is based on mechanics theories describing stress fields at crack tips, as discussed in Section 1.4.1, below. These methods involve crack-tip modeling with either the application of linear elasticity or poroelasticity. Overall, only a limited amount of work has investigated fracture in poroelastic materials [*Boone and Ingraffea*, 1990].

Techniques such as those used by *Bai and Pollard* [2000a,b] incorporate crack tip stresses in a linear elastic medium within a finite element model. These models are useful for analyzing fracture propagation where fluid flow and time-dependent processes are assumed to have negligible effects on the system. Some hydraulic fracture models simulate fracture fluid flow in an elastic medium using lubrication theory and do not directly account for flow into the formation [*Mendelsohn*, 1984a,b; *Advani et al.*, 1997]. For those processes in which fluids are considered important, poroelastic crack-tip models are analyzed using sophisticated coupled finite element and finite difference methods [*Boone and Ingraffea*, 1990; *Renshaw and Harvey*, 1994].

A few researchers [*Rice*, 1979, 1980, 1981; *Rudnicki*, 1980, 1981, 1985] studied the role of pore fluid diffusion in elastic and inelastic processes with specific emphasis on earthquakes. A major component of these works is that the pore fluid diffusion introduces a time scale into an otherwise time-independent process. An elastic, fluid-filled solid responds more stiffly to deformations that are rapid compared to the time scale of diffusion [*Rudnicki*, 1985]. Thus, time constants associated with fluid diffusion may be important considerations in fracture development. For example, a time constant can characterize how quickly a pulse or change in fluid pressure will travel some distance. Since the change in pressure will alter effective stress distributions, time constants will constrain the timing, and possibly the orientation, of fractures. These aspects are lumped together in a parameter termed the hydraulic diffusivity, defined as the ratio of the ability to transfer fluids (permeability) to the storage capacity (storativity).

1.4.1 Genesis and Propagation of Fractures

In general, fractures initiate and propagate when the stresses equal or exceed the rock strength. Sources of stress in the Earth's crust include overburden (where addition or removal of material is caused by deposition or erosion), fluid pressure, tectonic forces, and geological processes such as intrusion. Through the development of Linear Elastic Fracture Mechanics (LEFM) [*Lawn and Wilshaw*, 1975] and subsequent experimental verification, a tremendous amount has been learned about the initiation and propagation of cracks and fractures.

Joints are inferred to initate at flaws, based on field evidence [*Pollard and Aydin*, 1988]. Flaws may be anything from a simple grain contact to more complicated features such as fossils, cavities (pores), or microcracks. Joints are initiated where flaws perturb the local stress field such that the magnitude of local tensile stresses next to the flaw exceeds the tensile strength of the rock. This may occur under remote tension or remote compression. For example, remote tensional stresses may be amplified by factors of 1.5 to 3.0 inside circular inclusions [*Jaeger and Cook*, 1969] and, transfer of macroscopic compressive stresses through a heterogeneous material, like rock, can induce micro-tensile forces.

The initiation and propagation of tensile cracks in dry rocks under remote compressive stresses has been verified through many laboratory experiments [*Peng and Johson*, 1972; *Tapponnier and Brace*, 1976; *Kranz*, 1983]. The most common approach used is point loading of a circular shaped crack or flaw. With the addition of fluids point-loading mechanisms are only exac-

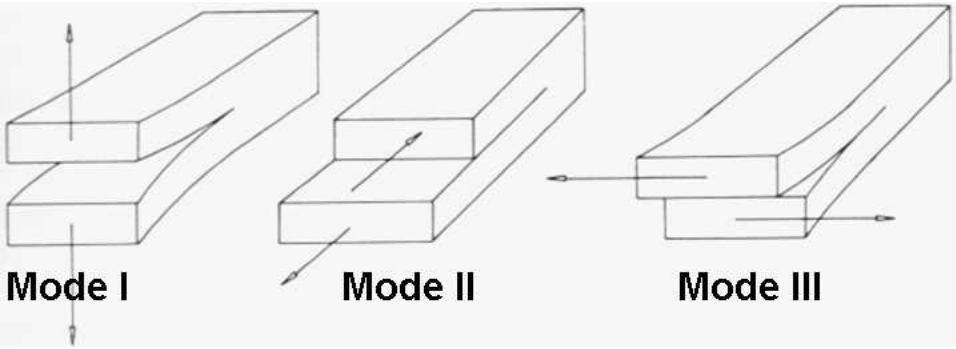

Figure 1.4: Three fundamental modes of fractures. Mode I - tensile, Mode II - in-plane shear, Mode III - anti-plane shear

erbated. *Pollard and Aydin* [1988] identify cavities and microcracks subjected to internal fluid pressure as most susceptible to joint initiation under remote compression.

The stress field around the fracture tip controls fracture propagation, and can be characterized by a stress intensity factor, which is a function of the applied stress and the fracture geometry. Each fracture mode, shown in Figure 1.4, has a stress intensity factor (K_I, K_{II}, K_{III}) and each is associated with a unique stress distribution near the fracture tip. Consider the stress intensity (K_I) for an opening mode (tensile) fracture subject to uniform remote stress (σ_3; Figure 1.5). K_I is defined as

$$K_I = (p - \sigma_3)[\pi a]^{1/2}. \tag{1.8}$$

The stress intensity factor is proportional to the driving stress ($p - \sigma_3$), and the square root of the fracture length. When stress intensity reaches a critical value $K_I = K_{IC}$ the fracture will propagate. The fracture toughness, K_{IC}, is a material property. This property is determined experimentally many different

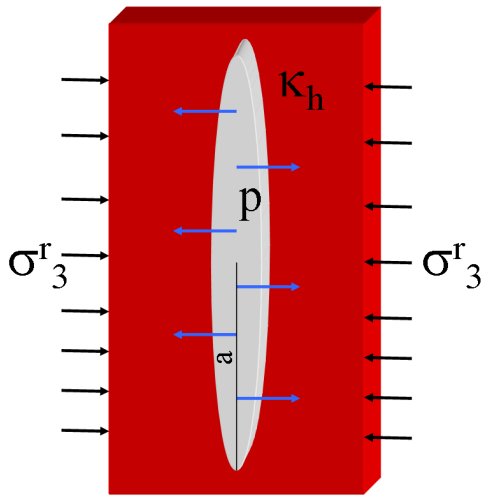

Figure 1.5: A mode I fracture of length $2a$ loaded by a remote compressive stress (σ_3) and fluid pressure (p).

ways, usually under biaxial compression and unsaturated, or under a vacuum [*Atkinson and Meredith*, 1987]. As evident from the above analysis, an internal pore pressure greater than the remote stress must be present for a Mode I crack or fracture to propagate under a remote compressive stress.

Irwin [1957] determined that a propagation criterion based on the above stress intensities is equivalent to the *Griffith* [1921] energy-balance criterion, $G_I = G_c$, for crack growth in a brittle elastic material. In this equation, G_I is the energy release rate, or the change in energy per unit crack extension, and G_c is the critical energy release rate for propagation to occur. For the crack pictured in Figure 1.5, the energy release rate is

$$G_I = (p - \sigma_3)^2 \pi a \frac{1-\nu}{2\mu}, \tag{1.9}$$

where ν is the Possion's ratio and μ is the shear modulus.

Joint propagation is related to the amount of joint opening. The opening, U_I, at the center of the crack in Figure 1.5 is [*Pollard and Segall*, 1987];

$$U_I = (p - \sigma_3)2a\frac{1-\nu}{\mu} \tag{1.10}$$

Equation (1.8) and Equation (1.10) imply that unless the pore pressure is greater than the remote compressive stress, then no stress concentration will develop and thus no fracture propagation will take place. The above analyses are applicable if it is assumed that the inelastic deformation is restricted to a relatively small region near the crack tip [*Irwin*, 1957].

For Mode I loading, the circumferential tensile stress at a small distance from the fracture tip is largest in the plane of the fracture. Therefore, joints propagate in their own plane perpendicular to the direction of greatest tension near the joint front. This occurs when the long axis of the crack is oriented perpendicular to the remote least compressive stress as in Figure 1.5. The complexity of single joint surfaces suggests that local principal stress directions can vary considerably [*Pollard and Aydin*, 1988]. In isotropic rocks, the joint path is primarily dependent on fluid pressure and the stress field. Therefore, local pore pressure gradients may cause stress variations.

The preceding analysis assumes that crack growth is achieved under quasi-static conditions. Inertial effects have been neglected. For propagation velocities approaching elastic wave speeds (i.e. fast), inertial forces must be considered and the traditional linear-elastic and elastic-plastic fracture mechanics, which assume quasi-static deformation, are inadequate.

Whether a fracture or crack will arrest (propagation velocity = 0)

depends on the amount of energy available for crack growth. As the energy release rate (Equation (1.9)) decreases to zero, fracture propagation depends on the value of the remote stress and the fluid pressure. If G_c is held constant, arrest can occur through either an increase in the remote compressive stress or by a decrease in the fluid pressure. A drop in fluid pressure may occur as a consequence of the increasing cross-sectional area of a growing fracture [*Secor*, 1969]. *Pollard and Aydin* [1988] state that the effectiveness of this arrest mechanism depends on how readily the pore fluid can recharge the fluid pressure in the joint. Arrest may also occur as the crack or fracture moves into a stiffer or more incompressible rock, as determined by the $\frac{1-\nu}{2\mu}$ term in Equation (1.9). The joint-propagation criterion, G_c, has also been shown to vary with a number of other factors such as confining pressure, temperature, chemical reaction rates, and microcracking [*Atkinson and Meredith*, 1987].

Lab experiments demonstrate that cracks also grow subcritically, under conditions of $G_I < G_c$. Several mechanisms for subcritical growth have been suggested [*Atkinson*, 1984]. These include stress corrosion, dissolution, diffusion, ion-exchange, and microplasticity. The chemical effects of pore water in the crustal environment influence all of these mechanisms. It is also interesting to note that subcritical cracking has been identified in glass under a vacuum [*Wiederhorn*, 1974]. *Atkinson and Meredith* [1987] list 6 variables that are important in subcritical crack growth:

- stress intensity factor
- temperature

- chemical equilibrium
- pressure
- rock microstructure
- residual strain

These factors vary significantly in the Earth's crust and hence the ability to relate subcritical crack growth in the field to a single mechanism is difficult. Overall, it has been suggested that some form of stress corrosion may be the most significant form of subcritical crack growth under appropriate conditions in the crust [*Atkinson and Meredith*, 1987].

In sum, all of these mechanisms rely heavily on (1) the presence of fluids and (2) pore fluid pressure at or above hydrostatic levels. *Pollard and Aydin* [1988] highlight the need for research on this subject. It is commonly assumed that the hydrologic regime is in a steady state when the structural regime is clearly transient. This suggests that processes, from a rock mechanist's point of view, have been traditionally un- or semi-coupled. As stated above, we know that fluids play important roles in the mechanics of rock, but our understanding has not progressed much in the last 30 years.

1.4.2 Natural Hydraulic Fractures

Recent work by *Renshaw and Harvey* [1994] addressed the quasi-static growth rates of natural hydraulic fractures (NHF). They simulated NHF in poroelastic media using a displacement discontinuity boundary element method. They noted that poroelastic effects may limit the rate of fracture growth, but

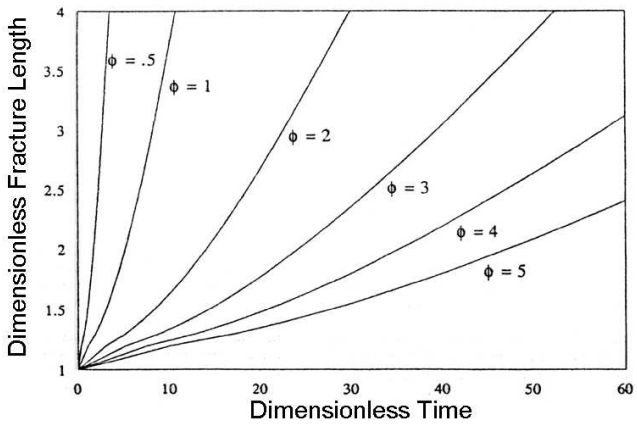

Figure 1.6: Plots of normalized fracture half-length (with respect to initial flaw length) versus dimensionless time show that rocks with higher ratios (ϕ) of amount of fluid required to sustain propagation (i.e., the change in area of the fracture per unit extension) to amount of fluid readily available (i.e., matrix storage) have fractures that grow slower. From *Renshaw and Harvey* [1994].

growth may still accelerate. In their model, the growth rate of isolated NHF (of initial flaw length of a_o) within many rock types is a function of the dimensionless time

$$\frac{Kt}{S^* a_o^2}. \tag{1.11}$$

Where characteristic ($\frac{S^* a_o^2}{K}$) time is dictated by the hydraulic conductivity as it determines how quickly fluid is transmitted to the fracture. The growth rate may be examined by considering the ratio of the amount of water required to sustain propagation (i.e. the change in area of the fracture per unit extension) to the amount of fluid readily available (i.e. matrix storage (S^*)),

$$\phi = \frac{(1-\nu)\rho g}{\mu S^*}. \tag{1.12}$$

The ratio $\frac{(1-\nu)}{\mu}$ controls the change in area. As S^* increases and ϕ decreases, more fluid is available to flow into the fracture. Shown in (Figure 1.6) are plots

of the dimensionless growth rate (fracture length vs. time) of an isolated NHF for various values of the dimensionless parameter ϕ. Note that unlike induced hydraulic fractures, the fluid pressure within natural hydraulic fractures is always less than the ambient fluid pressure once propagation begins [*Renshaw and Harvey*, 1994].

Much recent literature has focused on the subject of induced hydraulic fracturing for enhanced geothermal and oil extraction. As discussed above, the propagation of fractures explicitly depends on the stress distribution around the fracture tip. Thus, many papers (e.g. *Rice and Cleary* [1976]; *Advani et al.* [1987]) address pore fluid pressure at the crack tip. In general, theories under-predict the amount of pressure it takes to propagate an induced hydraulic fracture [*Advani et al.*, 1997]. A small region of reduced pressure at the tip of a propagating fracture can significantly reduce the stress intensity and thus require renewed abnormally high fluid pressure to propagate. This lower-pressure region is termed the fluid lag region and is usually attributed to excessive fluid flow into the formation. This suggests that fluid flow into the fracture may be a limiting process in geologic fracture generation.

Petroleum engineering studies also suggest that inducing local regions of high pore pressure via fluid injection may control hydraulic fracturing. *Bruno and Nakagawa* [1991] showed that induced hydraulic fractures will propagate toward regions of higher local pore pressure, or lower effective stress. Figure 1.7 is an adaptation of the experimental results of *Bruno and Nakagawa* [1991]. Higher injection pressures introduced greater deviation in fracture propagation direction. *Bruno and Nakagawa* [1991] also showed that stress concentra-

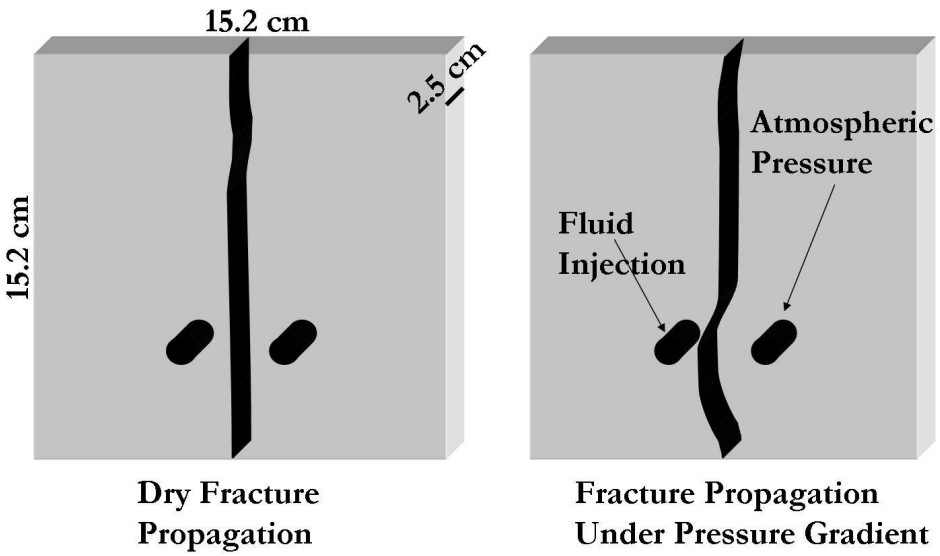

Figure 1.7: Deviation of fracture induced by pore pressure gradient. Adapted from *Bruno and Nakagawa* [1991].

tions at crack tips are influenced by pore pressure magnitude on a local scale. *Berchenko and Detournay* [1997] used a numerical model to demonstrate that pore pressures can alter the propagation path of an induced hydraulic fracture.

1.4.3 Pore Pressure Gradients

Many different factors cause pore pressure gradients in rocks. These include transients caused by heterogeneous expulsion of connate water during compaction, in-situ sources of fluid pressure (e.g. hydrocarbon generation), and local pressure gradients driving fluid diffusion. In the special case where a local, in-situ source of fluid pressure exists, fluid pressure gradients can significantly exceed hydrostatic. Such localized pressure gradients may cause effective stress to be low enough to influence fracture propagation near the fluid source

and no fracturing some distance away. The rate at which these pore pressure perturbations are diffused depends on the hydraulic diffusivity of the rock.

Hydraulic diffusivity describes the ability to transfer and store fluid mass. In groundwater hydrogeology, where uniaxial strain and constant vertical stress are commonly assumed conditions, the hydraulic diffusivity (κ) is

$$\kappa = \frac{k\rho g}{\mu S_s}, \tag{1.13}$$

where k is fluid permeability, S_s is one-dimensional specific storage. In coupled systems this relationship is more complex. The typical assumptions of uniaxial strain or constant vertical stress in every representative elementary volume (REV) are not met near a pumping well. Different definitions of storage arise because of its dependence on mechanical constraints. Since permeability can change with both direction and space, we need to consider hydraulic diffusivity to be a tensor property of the same order as that of the permeability. For a three-dimensional anisotropic heterogeneous system, each REV will have 3 diffusivities (with off diagonal terms equal to zero) and the tensor is second order symmetric.

If pressure changes occur within some time τ, then these pressure pulses will propagate a distance on the order of $\sqrt{\kappa\tau}$. If permeability is heterogeneous and distance is greater than the defined REV, then a harmonic average must be used to estimate κ. Also, a time of $\frac{L^2}{\kappa}$ is required for a pressure change to propagate a distance L, and is subject to the same averaging procedure.

1.5 Modeling of Coupled Fluid-Solid Mechanics

Problems involving coupled processes are typically addressed with continuum models that rely on constitutive relations developed through experimental work [*Neuzil*, 2003]. One concern with continuum-based models is that they yield very little information concerning material behavior. Alternative discrete-based methods, such as the discrete element method (DEM) for solid mechanics, use an approach that control and track many parameters, including pore structure and contact forces. An advantage of using a method like DEM is that the underlying physics are clearly resolved and the models are inherently discontinuous and heterogeneous, reflecting those properties of real geologic materials. A model such as DEM coupled with a discrete fluid-flow solver would enable investigation, at pore-scale, into coupled fluid-solid behavior in porous media. In this dissertation I take an approach that applies direct simulation (developed by *Cook et al.* [2000], *Cook* [2001],and *Cook et al.* [in press]) that couples the DEM with lattice-Boltzman (LB)[1]for application to the problem of natural hydraulic fracturing. I now briefly review the model used in this dissertation and then briefly compare the technique with other methods in the literature.

1.5.1 Discrete Element Method

The DEM technique has been successfully used to approximate the behavior of non-cohesive, granular systems under low stress conditions [*Cundall et al.*, 1982] and lithified sedimentary rocks [*Bruno and Nelson*, 1991; *Potyondy and Cundall*, In Press; *Hazzard et al.*, 2000; *Boutt and McPherson*, 2002]. In this paper we are employing an existing two-dimensional DEM application

[*Rege*, 1996]. DEM simulates the mechanical behavior of porous media by idealizing the system as a collection of separate particles that interact at their contact points. The method itself consists of (1) identifying elements in contact and (2) resolving the contact physics. The calculations performed in the DEM alternate between the application of Newton's Second Law and a force-displacement law (simple contact models) at the contacts between particles. The force-displacement law relates components of force to the corresponding components of the relative displacements through a generalized contact constitutive model. The contact constitutive model applied here is one with two parts, including a stiffness model and a slip model. The motion equations are then integrated explicitly with respect to time to obtain particle positions, are then used in the force-displacement calculations, and the calculation cycle starts over again. A benefit of this approach is that the DEM constitutive behaviors (stress and strain relations) are results rather than assumptions.

1.5.2 Lattice-Boltzmann and Coupled Model Theory

Fluid coupling with DEM was developed by *Cook* [2001] and *Cook et al.* [in press] through the integration of LB with the DEM (LBDEM) framework described above. A detailed development and validation of the coupled method can be found in *Cook et al.* [2000], *Cook* [2001], and *Cook et al.* [in press]. The two-dimensional simulations reported by *Cook* [2001] include such complex phenomena as drafting-kissing-tumbling in multi-particle sedimentation simulations and the saltation phase of bed erosion. An extended description of the method can be found in Chapter 5.

In the LBDEM formulation it is assumed that a fluid force is only

applied to the discrete elements if the fluid has a non-zero velocity. This implies that static pressure, on the whole, is not captured. Conceptually, issues with this assumption are avoided by treating changes in pressure within the model to be dynamic pressure or changes from a static pressure condition. This is accomplished by setting initial and boundary conditions to effective stress conditions, which is simply done by taking the total stress and subtracting off the static pressure. This limitation results in the poroelastic condition of setting the Biot-Willis coefficient (discussed above) equal to 1.

1.5.3 Previously Used Techniques

Many different frameworks are used to model the coupled physics of fluid-solid systems (See table 1.1) discussed above. These range from complete continuum approximations [*Wang*, 2000] to complete discontinuous approximations [*Bruno and Nelson*, 1991; *Boutt et al.*, 2003]. Most frameworks employ empirical constitutive relations governing fluid flow (e.g. Darcy's law) and fluid coupling (e.g. effective stress). The most common example is the assumption of Darcian flow. Below the REV scale (such as the case with discrete elements that are assumed to be grains), Darcy's law lacks physical meaning. A simple example of where Darcy' law won't apply is the accelerating and decelerating of flow through a pore throat. Regardless of this limitation, micromechanical

[1]The coupled LBDEM, originally called Modeling Interacting Multibody Engineering Systems (MIMES, [*Rege*, 1996]) was developed jointly by MIT (John Williams, PI) and Sandia National Laboratories (Dale Preece, PI; Ben Cook, PI) through a multiyear collaboration funded in part by the U.S. Department of Energy. The work of *Cook* [2001] highlights the addition of the lattice-Boltzmann method to and extension of the MIMES framework through funding provided by the National Oil and Gas Technology Partnership (NGOTP). The lattice-Boltzman coupled model is now called SandFlow2D.

Table 1.1: Summary of previously used coupling techniques

	Modeling Technique		**Coupling Technique**	
References	**Solid**	**Fluid**	**Solid → Fluid**	**Fluid →Solid**
Numerous Papers [See *Wang*, 2000; *Stephansson*, 2003, for reviews]	Poroelasticity	Darcy's	Pore Volume Changes	Effective Stress
Klosek [1997]; *Sakaguchi and Muhlhaus* [2000]; *Bruno et al.* [2001]; *Flekkoy and Malthe-Sorenssen* [2002]	DEM	Darcy's	Porosity-Permeability changes	Effective Stress
Bruno [1994]; *Li and Holt* [2001]	DEM	Poiseuille	Porosity-Permeability	Effective Stress
This dissertation	DEM	LB	No-Flow	Fluid Stresses

models using discrete elements coupled with a continuum fluid flow scheme based on Darcy's law seem to provide meaningful results [*Klosek*, 1997; *Sakaguchi and Muhlhaus*, 2000; *Bruno et al.*, 2001; *Flekkoy and Malthe-Sorenssen*, 2002]. Justifications for this approach suggest that discrete elements themselves are not grains but a collection of grains larger than a REV for fluid flow. As a result, these models must use empirical relations, such as the Kozeny-Carmen equation, to relate porosity to permeability.

Fluid to solid coupling in Darcian (in 2-D) based discrete models is achieved through integration of fluid force onto the solid, either at the solid centroid or around the solid perimeter. By the addition of static fluid pres-

sure to the solid grains, this applies the effective stress condition discussed in Section 1.3. Movements of the solid grains inhibit or induce fluid flow via porosity and permeability changes. In the case of a Darcy formulation, coupling is achieved through modification of hydraulic conductivity in Darcy's law. In the case of a flow network model [*Bruno*, 1994; *Li and Holt*, 2001], fluid flow is routed through cylindrical pipes governed by Poiseuille flow with the pipe diameter acting as a proxy for pore throats. Pipes are given a nominal diameter and as solids move away from one another this diameter is proportionally increased. Thus, in both of these formulations, the coupling is somewhat indirect because the conductance terms (pipe diameter or permeability) are tunable parameters with little more than an empirical basis. The LB technique used in this dissertation approximates the Navier-Stokes equations of fluid flow, no empirical relations are necessary to relate fluid flux to pressure drop at the pore scale. Also, the DEM approach does not require strict assumptions about the relationship between fluid permeability and porosity. Within the LBDEM framework the hydrodynamics simply evolve with the solid matrix.

1.6 Relationships between Micromechanical Properties and Macroscopic Concepts

In many instances throughout, the dissertation attempts to provide traditional hydrogeologic contexts and interpretations yet the numerical models utilized in the dissertation are founded on micromechanical theory. Interpretation with traditional contexts is necessary since very little work has been done using discretely coupled models. In addition, comparison of the models in the framework of established contexts provides support for their applicabil-

ity to the problems of interest. Below are a few commonly used continuum based parameters in hydrogeology and their relationships to microscopic and micromechanical properties.

1.6.1 Porosity

The porosity of a porous media is the defined as the total volume of pore space divided by the total volume of the porous media. At a microscopic level porosity is reflected as the individual pore space between, within, and surrounding the granular material. Porosity is a quantity that results from averaging a statistically significant volume of porous media (the REV), and thus these conditions are not met at the microscale. Important parameters that are quantifiable at the microscale and are related to the macroscopic porosity include the mean pore diameter and the surface area to volume ratio.

1.6.2 Permeability

Macroscopic permeability, as used in the context of Darcy's law, arises out of the interaction of some fluid with a solid porous matrix. The most important micro-properties of the porous media that influence macroscopic permeability are the connectivity and size of pore throats. Typically as the volume of pore space in a rock increases the permeability will also increase, reflecting this relationship. One important aspect in determining the porous media's macroscopic permeability is the degree of connection between the porosity. For example high porosity clay, with substantial pore volume in between clay layers, will have very low permeability. But, connectivity alone is not a prerequisite for a high permeability porous media, the length of connections (or tortuosity)

will play a large role in the observed macroscopic permeability. Anisotropies in macroscopic permeability arise from directional characteristics of the above parameters.

1.6.3 Storage Capacity and Hydraulic Diffusivity

The storage capacity of a porous media is a measure of the amount of the fluid that must be added to or removed from an REV to effect a given fluid pressure change. Two fundamental micromechanical processes (and ultimately properties) give rise to this macroscopic phenomenon: fluid compressibility and the porous media compressibility. The compressibility of fluid occupying a pore space can be a source or sink of fluid depending on the pressure conditions. At the microscopic level the amount of fluid produced per change in fluid pressure is a function of the pore space size and the fluid compressibility. The compressibility of a porous media is defined here as a change in volume of porous media per change in applied stress. As a result, the porous media compressibility is a strong function of the boundary conditions under which a change in stress takes place. For example, under drained hydrostatic compression the compressibility is simply referred to as the bulk modulus. The bulk can be further broken down into compressibility components related to the granular material compressibility (i.e. the compressibility of quartz in a sandstone) and the matrix compressibility. The matrix compressibility arises out of in-elastic deformation of the porous media that results in pore volume change with no change in grain volume. In a micromechanical context, the parameters that control the matrix compressibility are those that limit grain rearrangement, slippage, and grain breakage. In a micromechanical model these parameters

are friction, pore space distribution, and grain strength.

As defined above the hydraulic diffusivity is the ratio of permeability and storage capacity, and thus the micromechanical parameters that control the macroscopic hydraulic diffusivity are intimately linked to those that determine permeability and storage capacity. It is assumed that these parameters, such as porosity, will scale similarly between the permeability and the storage capacity, although very little work has been done on this subject. For completeness the important micromechanical parameters in determining the hydraulic diffusivity are the amount, shape, and distribution of pore space, the fluid compressibility, the grain compressibility, and the porous matrix compressibility.

1.7 Purpose, Goals, and Scope

It is the goal of this research to explore what control fluids exert on the initiation and propagation of opening mode fractures. This is accomplished through utilizing a suite of micromechanical tools to capture macroscopic material behavior. The DEM of *Potyondy and Cundall* [In Press] and the coupled DEM and lattice Boltzmann method of *Cook* [2001] and *Cook et al.* [in press] are used extensively in this research. A more detailed understanding of the feedback loop between strong deformations and fluid flow will allow a broader understanding of coupled processes in sedimentary basins, fault zones, and geothermal fields.

The coupling between fluid flow and the mechanics of rocks is shown, in the previous sections, to play a strong role in the behavior of hydrogeological systems. In many cases, these examples are limited to systems with purely

elastic deformations. This dissertation focuses on systems undergoing inelastic deformation, such as fracturing, which have not been previously examined in a hydrogeological context. The results of this dissertation will enable hydrogeologists to understand the importance of fluid pressure and flow on the distribution of fractures within sedimentary basins. Fractures commonly control the distribution of permeability in these types of systems, and thus are important factors in the mitigation of fluid pressure.

Understanding the conditions under which fractures form as the result of fluid overpressures is of critical importance for structural geologists. Numerous examples of studies were presented above that call on fluid-induced fractures, yet much debate still exists as to their prevalence in the geologic record. Most of the controversy arises from an incomplete conceptual model of fluid-induced fracture formation. This dissertation provides a physically based mechanism that meets the requirements of previously described qualitative models.

An additional and farther-reaching goal of this work is to understand the relationships between the microscale physics and the resulting macroscopic behaviors of coupled systems. With the further development of coupled micromechanical models of fluid-solid physics we can advance our understanding of the linkage between microscopic and macroscopic behaviors. These types of models can provide a context to interpret microscopic observations made in the laboratory and in the field. This includes a better understanding of the competing roles of mechanical and fluid heterogeneities in rock. With appropriate tools, underlying micro-mechanical processes that control observed

macroscopic fractures could be understood.

The specific tasks of this research included:

- Using a micromechanical approach (DEM) to capture observed macroscopic laboratory observations.
- Linking microscopic (DEM parameters) to macroscopic phenomena and exploring alternative model representations.
- Demonstrating the application of a calibrated micromechanical model to large scale fracturing in the Midland Basin, Texas.
- Demonstrating the validity of a coupled micromechanical model (LB-DEM) to porous media applications.
- Devising numerical and laboratory tests to generate fluid-induced fractures under realistic boundary conditions.
- Exploring the role of fluid pressure gradients in fracture genesis using physically based micromechanical formulations.
- Demonstrating proof of concept of experimental approach to generating hydraulic fractures using a laboratory test.

The results of a significant portion of this research apply to both dry and saturated rock. Most of the work focuses on relatively small scales and thus may be limited in application to larger spatial scales. Also, the assumptions associated with the 2-D models used in this study may not allow for the generalization of some of the specifics in this work to 3-D situations with complicated stress fields.

1.8 Organization of this Dissertation

Each chapter in this dissertation is a stand-alone document, suitable for publication in a refereed journal. Additional supporting material is included in the appendices, where appropriate.

The next 2 chapters (2-3) focus on micromechanical modeling of dry rock at multiple scales. These chapters set the stage for chapters 4-6, which investigate a coupled system of fluid and rock. Chapter 2 presents a discrete element method application and calibration procedure for sedimentary rocks. Chapter 2 has been published by *Boutt and McPherson* [2001]. Chapter 3 represents an application of the calibrated models from Chapter 2 to a large-scale fracturing problem in the Midland Basin. Portions of Chapter 3 have been accepted for publication in Geofluids journal.

Chapter 4 presents an alternative modeling approach to coupled fluid-solid problems developed by *Cook* [2001] and *Cook et al.* [in press]. Since the model has been only used previously for very specific applications, Chapter 4 explores the model's capabilities in solving problems in porous media. Chapter 5 examines some very detailed model comparisons to canonical fluid dynamics problems and 1-D poroelastic analytical solutions. Chapter 5 has been submitted for publication to the Journal of Geophysical Research. Application of the model presented in Chapter 4 and Chapter 5 to natural hydraulic fracturing is addressed in Chapter 6. Detailed examinations of the physics governing the process and associated implications for field relations are explored. The last section of this chapter includes results of laboratory experiments replicating the conditions used in the numerical study. Finally, conclusions and discussion of

future work are included in Chapter 7.

References

Advani, S., J. Torok, J. Lee, and S. Choudhry, Explicit time-dependent solutions and numerical evaluations for penny-shaped hydraulic fracture models, *Journal of Geophysical Research*, *92*, 8049–8055, 1987.

Advani, S., T. Lee, R. Dean, C. Pak, and J. Avasthi, Consequences of fluid lag in three-dimensional hydraulic fractures, *International Journal of Numerical and Analytical Methods in Geomechanics*, *21*, 229–240, 1997.

Atkinson, B., Subcritical crack growth in geological materials, *Journal of Geophysical Research*, *89*, 4077–4114, 1984.

Atkinson, B., and P. Meredith, The theory of subcritical crack growth with applications to minerals and rocks, in *Fault Mechanics and Transport Properties of Rock*, edited by B. Atkinson, pp. 111–166, Academic Press, San Diego, 1987.

Bai, T., and D. Pollard, Closely spaced fractures in layered rocks: initiation mechanism and propogation kinematics, *Journal of Structural Geology*, *22*, 1409–1425, 2000a.

Bai, T., and D. Pollard, Fracture spacing in layered rocks: A new explanation based on the stress transition, *Journal of Structural Geology*, *22*, 43–57, 2000b.

Berchenko, I., and E. Detournay, Deviation of hydraulic fractures through poroelastic stress changes induced by fluid injection and pumping, *Inter-*

national Journal of Rock Mechanics and Mining Sciences and Geomechanics Abstracts, *34*, 1009–1019, 1997.

Berryman, J. G., Effective stress for transport properties of inhomogeneous porous rock, *Journal of Geophysical Research*, *97*, 17,409–17,424, 1992.

Biot, M., General theory of three-dimensional consolidation, *J. Appl. Phs.*, *12*, 155–164, 1941.

Boone, T. J., and A. R. Ingraffea, A numerical procedure for simulation of hydraulically-driven fracture propagation in poroelastic media, *I. J. for Num. Anal. Meth. Geomech.*, *14*, 27–47, 1990.

Boutt, D., and B. McPherson, Discrete element models of the micromechanics of sedimentary rock: The role of organization vs. friction, *EOS Trans. AGU*, *82*, Abstract T32E–0913, 2001.

Boutt, D. F., and B. J. McPherson, Simulation of sedimentary rock deformation: Lab-scale model calibration and parameterization, *Geophysical Research Letters*, *29*, 10.1029/2001GL013,987, 2002.

Boutt, D. F., B. K. Cook, B. J. McPherson, and J. Williams, Application of a directly coupled numerical model of fluid-solid mechanics, in *Soil and Rock America 2003*, edited by T. Culligan, A. Whittle, and H. Einstein, MIT, Cambridge, MA, 2003.

Bradley, J., Abnormal formation pressure, *AAPG Bulletin*, *59*, 957–973, 1975.

Breckels, I., and H. v. Eekelen, Relationship between horizontal stress and depth in sedimentary basins, *J. Pet. Technol.*, *34*, 2191–2199, 1982.

Bredehoeft, J., J. Wesley, and T. Fouch, Simulations of the origin of fluid pressure, fracture generation, and the movement of fluids in the Uinta basin, Utah, *AAPG Bulletin*, *78*, 1729–1747, 1994.

Bruno, M., Micromechanics of stress-induced permeability anisotropy and damage in sedimentary rock, *Mechanics of Materials*, *18*, 31–48, 1994.

Bruno, M., and F. Nakagawa, Pore pressure influence on tensile fracture propagation in sedimentary rock, *International Journal of Rock Mechanics and Mining Sciences and Geomechanics Abstracts*, *28*, 261–273, 1991.

Bruno, M., and R. Nelson, Microstructural analysis of the inelastic behavior of sedimentary rock, *Mechanics of Materials*, *12*, 95–118, 1991.

Bruno, M., A. Dorfmann, K. Lao, and C. Honeger, Coupled particle and fluid flow modeling of fracture and slurry injection in weakly consolidated granular media, in *Rock Mechanics in the National Interest*, edited by Elsworth, Tinucci, and Heasley, Swets and Zeitlinger Lisse, Washington, D.C., 2001.

Cook, B., D. Noble, D. Preece, and J. Williams, Direct simulation of particle laden fluids, in *Fourth North American Rock Mechanics Symposium.*, A.A. Balkema, Rotterdam, 2000.

Cook, B., D. Noble, D. Preece, and J. Williams, Direct simulation of particle laden fluids, *Journal of Engineering Computations*, in press.

Cook, B. K., A numerical framework for the direct simulation of solid-fluid systems, Doctoral dissertation, Massachusetts Institute of Technology, 2001.

Cundall, P., A. Drescher, and O. Strack, Numercal experiments on granular assemblies: Measurements and observations, in *Deformation and Failure of Granular Materials*, edited by J. Jenkins and H. Luger, A.A. Balkema, Brookfield, VT, 1982.

Detournay, E., and A. H.-D. Cheng, Fundamentals of poroelasticity, in *Comprehensive Rock Engineering: Principles, Practice and Projects*, edited by J. Hudson, Pergammon Press, Oxford, UK, 1993.

Engelder, T., *Stress regimes in the lithosphere*, Princeton University Press, Princeton, New Jersey, 1993.

Engelder, T., and M. Fischer, Influence of poroelastic behavior on the magnitude of minimum horizontal stress, sh, in overpressured parts of sedimentary basins, *Geology*, *22*, 949–952, 1994.

Engelder, T., and A. Lacazette, Natural hydraulic fracturing, in *Rock Joints*, edited by N. Barton and O. Stephansson, A.A. Balkema, Brookfield, 1990.

Fischer, M., Application of linear elastic mechanics to some problems of fracture propagation in rock and ice, Doctoral dissertation, The Pennsylvania State Univ., 1994.

Fischer, M. P., M. R. Gross, T. Engelder, and R. J. Greenfield, Finite-element analysis of the stress distribution around a pressurized crack in a layered elastic medium: Implications for the spacing of fluid driven joints in bedded sedimentary rock, *Tectonphysics*, *247*, 49–64, 1995.

Flekkoy, E. G., and A. Malthe-Sorenssen, Modeling hydrofracture, *Journal of Geophysical Research*, *107*, 2151–2151, 2002.

Galloway, D., D. Jones, and S. Ingebritsen, Land subsidence in the United States, *Fact Sheet 165-00*, U.S. Geological Survey, 2000.

Griffith, A., The phenomena of rupture and flow in solids, *Royal Society of London Transactions*, *221*, 163–198, 1921.

Hancock, P., Brittle microtectonics: Principles and practice, *Journal of Structural Geology*, *7*, 437–457, 1985.

Hazzard, J., P. F. Young, and S. Maxwell, Micromechanical modeling of cracking and failure in brittle rocks, *Journal of Geophysics Research*, *105*, 16,683–16,697, 2000.

Hsieh, P., and J. Bredehoeft, A reservoir analysis of the denver earthquakes: a case of induced seismicity, *Journal of Geophysical Research*, *86*, 903–920, 1981.

Hubbert, M., and W. Rubey, Role of fluid pressure in mechanics of overthrust faulting, *GSA Bulletin*, *70*, 115–166, 1959.

Irwin, G., Analysis of stress and strain near the end of a crack traversing a plate, *Journal of Applied Mechanics*, *24*, 361–364, 1957.

Jaeger, J., and N. Cook, *Fundamentals of Rock Mechanics*, 2nd ed., Chapman and Hall, London, 1969.

Kinji, M., Mechanisms of natural hydraulic fracturing in a sedimentary basin, *AAPG Bulletin*, pp. 123–132, 1981.

Klosek, J., The integration of fluid dynamics with a discrete-element modelling system : Algorithms, implementation, and applications, Masters thesis, Massachusetts Institute of Technology IT, 1997.

Kranz, R. L., Microcracks in rocks: A review, *Tectonophysics*, *100*, 449–480, 1983.

Kumpel, H.-J., Special issue "thermo-hydro-mechanical coupling in fractured rock", *Pure and Applied Geophysics*, *160*, 809–812, 2003.

Lacazette, A., and T. Engelder, Fluid-driven cyclic propagation of a joint in the Ithaca siltstone, in *Fault Mechanics and Transport Properties of Rock*, edited by B. Evans and T.-F. Wong, pp. 297–323, Academic Press, San Diego, 1992.

Lawn, B., and T. Wilshaw, *Fracture of Brittle Solids*, Cambridge University Press, Cambridge, England, 1975.

LHeureux, I., and A. D. Fowler, A simple model of flow patterns in overpressured sedimentary basins with heat transport and fracturing, *Journal of Geophysical Research*, *105*, 23,741–23,752, 2000.

Li, L., and R. Holt, Simulation of flow in sandstone with fluid coupled particle model, in *Proceedings of the 38th U.S. Rock Mechanics Symposium: Rock Mechanics in the National Interest*, edited by D. Elsworth, J. P. Tinucci, and A. Heasley, pp. 511–516, A.A. Balkema, Rotterdam, 2001.

McConaughy, D. T., and T. Engelder, Joint initiation in bedded clastic rocks, *Journal of Structural Geology*, *23*, 203–221, 2001.

McPherson, B., and J. Bredehoeft, Overpressures in the Uinta basin, Utah: Analysis using a three-dimensional basin evolution model, *Water Resources Research*, *37*, 857–872, 2001.

Mendelsohn, D., A review of hydraulic fracture modeling - i: General concepts, 2d models, motivation for 3d modeling, *J. Energy Resources Tech*, *106*, 369–376, 1984a.

Mendelsohn, D., A review of hydraulic fracture modeling - ii: 3d modeling and vertical growth in layered rock, *J. Energy Resources Tech*, *106*, 543–553, 1984b.

Merlani, A. L., G. Natale, and E. Salusti, Fracturing processes due to temperature and pressure non-linear waves propagating in fluid-saturated porous rocks, *Journal of Geophysical Research*, *106*, 11,067–11,081, 2001.

Miller, T. W., New insights on natural hydraulic fractures induced by abnormally high pore pressures, *AAPG Bulletin*, *79*, 1005–1018, 1995.

Muehlberger, W., Conjugate joint sets of small dihedral angle, *Journal of Geology*, *69*, 211–218, 1961.

Narr, W., and J. Currie, Origin of fracture porosity - example from Altamont field, Utah, *AAPG Bulletin*, *66*, 1231–1247, 1982.

Neuzil, C., Abnormal pressures as hydrodynamic phenomena, *American Journal of Science*, *295*, 742–786, 1995.

Neuzil, C. E., Hydromechanical coupling in geologic processes, *Hydrogeology Journal*, *11*, 41–83, 2003.

Osborne, M. J., and R. E. Swarbrick, Mechanisms for generating overpressure in sedimentary basins: A reevaluation, *AAPG Bulletin*, *81*, 1023–1041, 1997.

Payne, D. F., K. Tuncay, A. Park, J. B. Comer, and P. Ortoleva, A reaction-transport-mechanical approach to modeling the interrelationships among gas generation, overpressuring, and fracturing - implications for the Upper Cretaceous natural gas reservoirs of the Piceance basin, Colorado, *AAPG Bulletin*, *84*, 545–565, 2000.

Peng, S., and A. Johson, Crack growth and faulting in cylindrical specimens of Chelmsford granite, *International Journal of Rock Mechanics and Mining Sciences and Geomechanics Abstracts*, *10*, 37–86, 1972.

Pollard, D., and P. Segall, Theoretical displacements and stresses near fractures in rock: With application to faults, joints, veins, dikes, and solution surfaces, in *Fault Mechanics and Transport Properties of Rock*, edited by B. Atkinson, pp. 277–350, Academic Press, San Diego, 1987.

Pollard, D. D., and A. Aydin, Progress in understanding jointing over the past century, *GSA Bulletin*, *100*, 1181–1204, 1988.

Potyondy, D. O., and P. A. Cundall, A bonded-particle model for rock, *International journal of rock mechanics and mining sciences*, In Press.

Ramsay, J. G., and M. I. Huber, *The Techniques of Modern Structural Geology Volume 2: Folds and Fractures*, Academic Press, San Diego, 1987.

Rege, N., Computational modeling of granular materials, Doctoral dissertation, Massachusetts Institute of Technology, 1996.

Renshaw, C. E., and C. F. Harvey, Propagation velocity of a natural hydraulic fracture in a poroelastic medium, *Journal of Geophysical Research*, *99*, 21,667–21,677, 1994.

Rice, J., Theory of precursors in the inception of earthquake rupture, *Gerlands Beitr. Geophysics*, pp. 91–127, 1979.

Rice, J., The mechanics of earthquake rupture, in *Physics of the Earth's Interior, Proceedings of the International School of Physics 'Enrico Fermi'*, edited by A. Dziewonski and E. Boschi, pp. 555–649, Italian Physical Society, North-Holland, Amsterdam, 1980.

Rice, J., Pore fluid processes in the mechanics of earthquake rupture, *Solid Earth Geophysics and Geotechnology*, *42*, 81–89, 1981.

Rice, J., and M. Cleary, Some basic stress diffusion solutions for fluid-saturated elastic porous media with compressible constituents, *Rev. Geophys. Space Physics*, *14*, 227–241, 1976.

Rudnicki, J., Fracture mechanics applied to the Earth's crust, in *Ann. Reviews of Earth Planetary Science*, edited by F. Donath, vol. 8, pp. 489–525, Annual Reviews Inc, Palo Alto, CA, 1980.

Rudnicki, J., On "Fundamental solutions for a fluid-saturated porous solid" by M.P. Cleary, *Int. J. Solids Structures*, *17*, 855–857, 1981.

Rudnicki, J., Effect of pore fluid diffusion on deformation and failure of rock, in *Mechanics of Geomaterials*, edited by Z. Bazant, pp. 315–347, John Wiley and Sons, 1985.

Saffer, D., and B. A. Bekins, Hydrologic controls on the morphology and mechanics of accretionary wedges, *Geology*, *30*, 271–274, 2002.

Saffer, D. M., B. A. Bekins, and S. Hickman, Topographically driven groundwater flow and the San Andreas heat flow paradox revisited, *Journal of Geophysical Research*, *108*, doi:10.1029/2002JB001,849, 2003.

Sakaguchi, H., and H.-B. Muhlhaus, Hydrid modeling of coupled pore fluid-solid deformation problems, *Pure and Applied Geophysics*, *157*, 1889–1904, 2000.

Secor, D., Mechanics of natural extension fracturing at depth in the Earth's crust, *Geological Survey of Canada*, *Paper No. 68-52*, 3–48, 1969.

Secor, D. T., Role of fluid pressure in jointing, *American Journal of Science*, *263*, 633–646, 1965.

Secor, D. T., and D. D. Pollard, On the stability of open hydraulic fractures in the Earth's crust, *Geophsical Research Letters*, *2*, 510–513, 1975.

Segall, P., and D. Pollard, Joint formation in granitic rock of the Sierra Nevada, *GSA Bulletin*, *94*, 563–575, 1983.

Stephansson, O., Theme issue on hydromechanics in geology and geotechnics, *Hydrogeology Journal*, *11*, DOI 10.1007/s10,040–002–0247–z, 2003.

Tapponnier, P., and W. Brace, Development of stress-induced microcracks in Westerly granite, *Int. J. Rock Mech. Sci.*, *13*, 103–112, 1976.

Terzaghi, K., *Erdbaumechanik auf Bodenphysikalischer Grundlage*, Deuticke, Leipzig, 1925.

Tuncay, K., A. Park, and P. Ortoleva, Sedimentary basin deformation: an incremental stress approach, *Tectonophysics*, *323*, 77–104, 2000.

Wang, H., *Theory of Linear Poroelasticity: with Applications to Geomechanics and Hydrogeology*, Princeton University Press, Princeton, New Jersey, 2000.

Warpinski, N., and L. Tuefel, Determination of the effective stress law for permeability and deformation in low permeability rocks, *INTERNATIONAL JOURNAL OF ROCK MECHANICS AND MINING SCIENCES*, *SPE Formation Evaluation*, 121–131, 1992.

Wiederhorn, S., in *Fracture mechanics of Ceramics*, edited by R. Bradt, D. Hasselman, and F. Lange, pp. 549–580, Plenum Press, New York, 1974.

Yow, J., and J. Hunt, Coupled processes in rock mass performance with emphasis on nuclear waste isolation, *International Journal of Rock Mechanics and Mining Sciences*, *39*, 143–1150, 2002.

CHAPTER 2

SIMULATION OF SEDIMENTARY ROCK DEFORMATION: LAB-SCALE MODEL CALIBRATION AND PARAMETERIZATION[1]

Abstract

Understanding the mechanical behavior of rock is critical for researchers and decision-makers in fields from petroleum recovery to hazardous waste disposal. Traditional continuum-based numerical models are hampered by inadequate constitutive relationships governing fracture initiation and growth. To overcome limits associated with continuum models we employed a discrete model based on the fundamental laws of contact physics to calibrate triaxial tests. Results from simulations of triaxial compression tests on a suite of sedimentary rocks indicate that the basic physics of rock behavior are captured. Evidence for this conclusion lies in the fact that one set of model parameters describes rock behavior at many confining pressures. The use of both inelastic and elastic parameters for comparison yields insight concerning the uniqueness of these models. These tests will facilitate development and calibration of larger scale

[1]Portions of this chapter appeared in *Geophysical Research Letters*: Boutt, D.F. and B.J.O.L. McPherson, Simulation of Sedimentary Rock Deformation: Lab-Scale Model Calibration and Parameterization, *Geophys Res. Letters*, 29(4), 10.1029/2001GL013987, 2002.

discrete element models, which may be applied to a wide range of geological problems.

2.1 Introduction

The mechanical behavior of sedimentary rocks is an important aspect of many investigations in the earth sciences. Previous workers analyzed these behaviors in the laboratory and made fundamental advancements (See *Lockner* [1995] for review). This paper highlights an investigation of the micromechanical behavior of sedimentary rocks using the discrete element method (DEM) pioneered by *Cundall* [1971] and *Cundall and Strack* [1979]. This type of DEM simulates the mechanical behavior of rock by idealizing the system as a collection of separate particles bonded together at their contact points, and utilizes the breakage of individual structural units or bonds to represent damage. The DEM used successfully models the behavior of rocks, particularly damage and non-linear behaviors, by employing simple contact models [*Potyondy et al.*, 1996; *Hazzard et al.*, 2000; *Potyondy and Cundall*, In Press]. Models that explicitly include damage are unique and far more robust than models that indirectly represent damage through empirical relations, such as continuum models. In the DEM constitutive behaviors are results rather than assumptions.

This study builds on previous DEM studies by exploring model behavior at a variety of stress states through attempting to explicitly reproduce select rock behavioral properties and to identify correlations between model results and observed rock behavior. In examining a variety of stress states we found that particle clustering (groups of bonded particles) allow a more

expanded range of micromechanical behaviors. In addition, by examining multiple stress states we determined important micro-parameter relationships that are not otherwise apparent.

2.2 Modeling Approach

2.2.1 Limitations of Previous DEM Studies

Previous DEM studies [*Hazzard et al.*, 2000; *Bruno and Nelson*, 1991; *Wang et al.*, 2000; *Potyondy*, 2002; *Potyondy and Cundall*, In Press] of laboratory scale mechanical behavior examined very limited sets of tests under similar stress states. Results of these tests and simulations may be too specific to the chosen tested stress states and not adequately represent general rock behavior. In many cases the microparameters (i.e., DEM model parameters) that govern macroscopic rock behavior reproduce the specific stress state, but do not provide a complete failure envelope. A more robust approach is to use many stress states to define the relevant microparameters (i.e., macroscopic rock properties). This would result in a more complete comparison and also reduce the number of degrees of freedom. Other research (e.g., *Li and Holt* [2001]) examined compaction and dilation of highly porous rock at different confining pressures, but did not compare model results to laboratory test data.

2.2.2 Selection of Parameters to Calibrate

For our purposes, the most important material properties to calibrate are the elastic and inelastic rock properties, including Young's modulus, Poisson's ratio, failure strength (at many confining pressures), and style of failure (uniaxial splitting or shear faulting, cataclastic flow, ductile). The style of fail-

ure is very important in a rock deformation model since it is an explicit control on the distribution of brittle deformation taking place. We have observed that strain localization in our models of rock can be somewhat distributed and ductile in nature and still match the observed elastic and inelastic parameters. Thus it is important to replicate both elastic and inelastic strain accumulation. An exact match to the shape of the stress-strain curve is not sufficient since most rocks undergo some inelastic deformation during laboratory tests due to flaws in addition to the inherent randomness of both samples and models.

2.2.3 Methods

We are using a commercially available DEM code called Particle Flow Code in 2 Dimensions (PFC2D), developed by Itasca Consulting Group, Inc [*Itasca Consulting Group*, 1999]. A detailed description of the two- and three-dimensional PFC model and the theory is provided by *Potyondy and Cundall* [In Press] and *Hazzard et al.* [2000]. Mechanical measurements of a suite of sedimentary rocks from the Midland Basin, Texas were selected for analysis. The Midland Basin rocks vary in lithology from fine-grained sandstones to laminated mudstones with little matrix porosity and exhibit a wide range of unconfined failure strengths (between 137 MPa and 220 MPa). For more details concerning the rocks, associated properties and data collection see *Lorenz et al.* [2002] and *Sterling* [2000].

The bonded-particle model (BPM) detailed in *Potyondy and Cundall* [In Press] is an implementation based on DEM that constructs a bonded DEM system. The BPM consists of methods to generate elements, pack them into a region, and prescribe particle and bond parameters. Use of the BPM allows a

consistent means of generating and assigning parameters to a bonded-particle model. In addition to particle density, particle shape, and particle size distribution, a set of 8 parameters, 10 if using both contact bonds in addition to parallel bonds, completely defines a BPM. These parameters are (equation (17) of *Potyondy and Cundall* [In Press]):

$$\begin{aligned} \{E_c, (k_n/k_s), \mu\} \qquad & \text{particle microproperties} \\ \{\bar{\lambda}, \bar{E}_c, (\bar{k}^n/\bar{k}^s), \sigma_c, \tau_c, \bar{\sigma}_c, \bar{\tau}_c\} \qquad & \text{bond microproperties} \end{aligned} \tag{2.1}$$

where E_c and $\bar{E}_c$ are the Young's moduli of the particles and parallel bonds, respectively; (k_n/k_s) and $(\bar{k}^n/\bar{k}^s)$ are the ratios of normal to shear stiffness of the particles and parallel bonds, respectively; σ_c and τ_c are the tensile and shear strengths, respectively, of the contact bonds; $\bar{\lambda}$ is the radius multiplier of the parallel bonds; μ is the particle friction coefficient; and $\bar{\sigma}_c$ and $\bar{\tau}_c$ are the tensile and shear strengths, respectively, of the parallel bonds. Equation (18) of *Potyondy and Cundall* [In Press] is used to relate the particle and parallel-bond moduli to the corresponding normal stiffnesses such that the particle and parallel-bond stiffnesses are assinged as

$$\begin{aligned} k_n &:= 2tE_c, t = 1, \\ k_s &:= \tfrac{k_n}{(k_n/k_s)} \\ \bar{k}^n &:= \tfrac{\bar{E}_c}{R^{(A)}+R^{(B)}} \\ \bar{k}^s &:= \tfrac{\bar{k}^n}{(\bar{k}^n/\bar{k}^s)} \end{aligned} \tag{2.2}$$

where R is the particle radius of particle A and B.

In this chapter we explore the effect of an additional parameter, namely the maximum number of elements within clusters (S_c). Particle clustering (*Potyondy and Cundall* [In Press]) refers to the process of bonding 2 or

more particles with a normal and shear strength greater than the strengths of the bonds between the clusters themselves (inter-cluster bonds). In practical terms, clustering is intended to make the DEM particles or particle clusters more closely mimic the mechanical behavior of rock grains or groups of grains.

Laboratory conditions are explicitly reproduced in the model, including servo controlled confining pressure, platen velocity, and sample size. The particle size distribution was uniformly distributed with the smallest particle being 1.0 mm ($D_{\min}$) and the largest being 1.66 mm ($D_{\max}$) in diameter in an area 0.0254 m wide by 0.0508 m long. Models specimens were built using the material-genesis procedure described in *Potyondy and Cundall* [In Press]. This process consists of placing a pre-calculated number of particles in a box and iteratively increasing their size until the assembly is well packed. Care is taken such that the minimum number of contacts on each particle was close to three. Isotropic stress (the initial stress state) in the assembly is then adjusted to 1 MPa by changing particle size iteratively until the desired value is reached. At this point the elements in contact are then bonded together.

We do not stipulate that a single particle will represent a single rock grain, but rather the assembly represents a collection of spatially averaged grains [*Hazzard et al.*, 2000]. Each model therefore consisted of roughly 1000 particles giving an average of 22 particles along the shortest dimension of the model. This number of particles ensures the model is not sensitive to our choice in particle size, using the criteria of *Huang et al.* [1999].

Table 2.1 gives the values of input microparameters for each of the 4 models. Particle densities were set at 2600 kgm^{-3} for all models. For all the

models described in this chapter, a local non-viscous damping was used with a coefficient of 0.7 to approximate quasi-static behavior. Both contact and parallel bonds were used in all of the models. The addition of contact bonds with different strengths than the parallel bonds allows for a two-step failure of the material. The presence of contact bonds at different strengths than that of parallel bonds appears to improve the ability of the model to capture the trend of increasing material strength with confining pressure. All bonds (contact and parallel) within clusters had 650 MPa strength magnitudes, whereas all bonds between clusters had the strengths shown in Table 2.1. Cluster size (S_c) varied between 2 and 3 for the models presented.

Clusters in these models were generated from a densely packed particle assembly by traversing the bonded-particle contacts (See section 3.4 of *Potyondy and Cundall* [In Press]). Each cluster is grown by selecting an individual particle and then adding adjacent particles to the cluster until the value of S_c is reached. This results in a distribution of cluster sizes throughout the packed assembly (Figure 2.1). Preliminary work on effects of cluster geometry indicates that it has a strong influence on the slope of the compressional strength envelope.

2.3 Results and Discussion

2.3.1 General Relationships Among Microparameters and Macroparameters

Our procedure for attempting to reproduce the rock behavior began with an extensive sensitivity study attempting to elucidate which microparameters exerted the strongest control on the macroparameters of interest. We

Table 2.1: Input Microparameters for DEM Models. Parameters notation is consistent with the notation of *Potyondy and Cundall* [In Press] to allow for comparison.

	1U-1	**5U-3**	**5U-4**	**5U-6**
k^n/k^s, $\bar{k}^n/\bar{k}^s$ (-)	0.5	0.5	0.5	0.5
E_c, $\bar{E}_c$ (GPa)	23.5	13.5	23.5	22.0
μ (-)	0.7	0.6	0.7	0.5
$\bar{\sigma}_c$ (MPa)	18.0	10.45	10.5	12.5
$\bar{\tau}_c$ (MPa)	144.0	83.6	84.0	100
σ_c (MPa)	24.0	20.9	15.75	25.0
τ_c (MPa)	192	167.2	126.0	200.0
$\bar{\lambda}$ (-)	1.0	1.0	1.0	1.0
S_c (-)	3	2	3	2

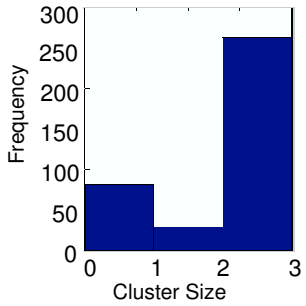

Figure 2.1: A histogram of the distribution of cluster sizes in a 3 cluster model indicates that not all of the clusters are 3 large. A small number of 2 clusters and single elements are present.

attempt to describe what microparameters were found to control which macroscopic model behaviors (macroparameters). The particle friction coefficient (μ) and particle clustering (S_c) attributes were found to increase the slope of the compressive failure envelope. This results in an increase in failure strength of the higher confining pressure samples, possibly due to interlocking of the clusters [*Boutt and McPherson*, 2001]. We suggest that the particle friction coefficient has a similar effect on failure strength.

The normal and shear contact and parallel bond moduli ($E_c, \bar{E}_c$) influence the elastic parameters, with the ratio of the normal to shear stiffnesses (k^n/k^s, $\bar{k}^n/\bar{k}^s$) having a larger effect on the exhibited Poisson's ratio of the assembly. The contact and parallel bond strength (σ_c, τ_c, $\bar{\sigma}_c$, $\bar{\tau}_c$) of the inter-cluster bonds of a clustered material is set such that it controls the uniaxial compressional strength with the particle clustering controlling the slope of the failure envelope.

2.3.2 Calibration of Failure Mode

Our initial modeling efforts suggested that even though quantitative and consistent calibrations between the simulated and observed material properties were possible, the type and mode of failure was quite different in the model than those measured or observed in the actual rock deformation tests. In some cases a somewhat non-localized ductile type of failure was observed. We believe that the model assembly was failing in a non-localized manner because shear and normal bond strengths were similar. The model was failing preferentially through shear bond breakages, whereas failure and localization depend on differential stress and interparticle shear strength. Models with

high ratios of shear to normal bond strength (> 4) produce a well defined shear plane, as illustrated in Figure 2.2. A similar conclusion was documented by *Huang et al.* [1999]. In summary, the ratio of shear to normal bond strength in the DEM plays an important role in strain localization. Greater than 90% of the bonds in each model failed in tension, indicating that the interparticle tensile strength is the key micro-process controlling both localization and failure in the specimens. By using quantitative (and qualitative) measures of inelastic processes in addition to elastic properties for comparison we derive microparameter relationships that are otherwise undeterminable.

The evolution of strain localization in a modeled sample via a through-cutting shear fault is depicted for a sample under uniaxial stress in Figure 2.2. In this plot, gradients of displacement are contoured to emphasize areas undergoing differential movement [*Morgan and Boettcher*, 1999]. A stark contrast in displacement gradient magnitudes indicates that regions on either side are moving coherently. The gradients are then plotted at different times throughout the test and are related to the axial stress-strain plot by the numbers above the individual plot. Before peak stress, stage 1 through 2, the sample exhibits very low magnitudes of displacement gradients. A slight amount of localization is developed in stage 3 where a linear feature first appears. At peak stress, stage 4, the sample begins to show displacement gradients that resemble a failure plane. Stages 5 through 7 show the post peak behavior where the through going shear fault is realized and destruction of the sample begins by development of splays off the main fault. This is consistent with our laboratory observations and with the results of *Menendez et al.* [1996]. Progression of strain localization in the modeled samples is captured with the calculated displacement gradients,

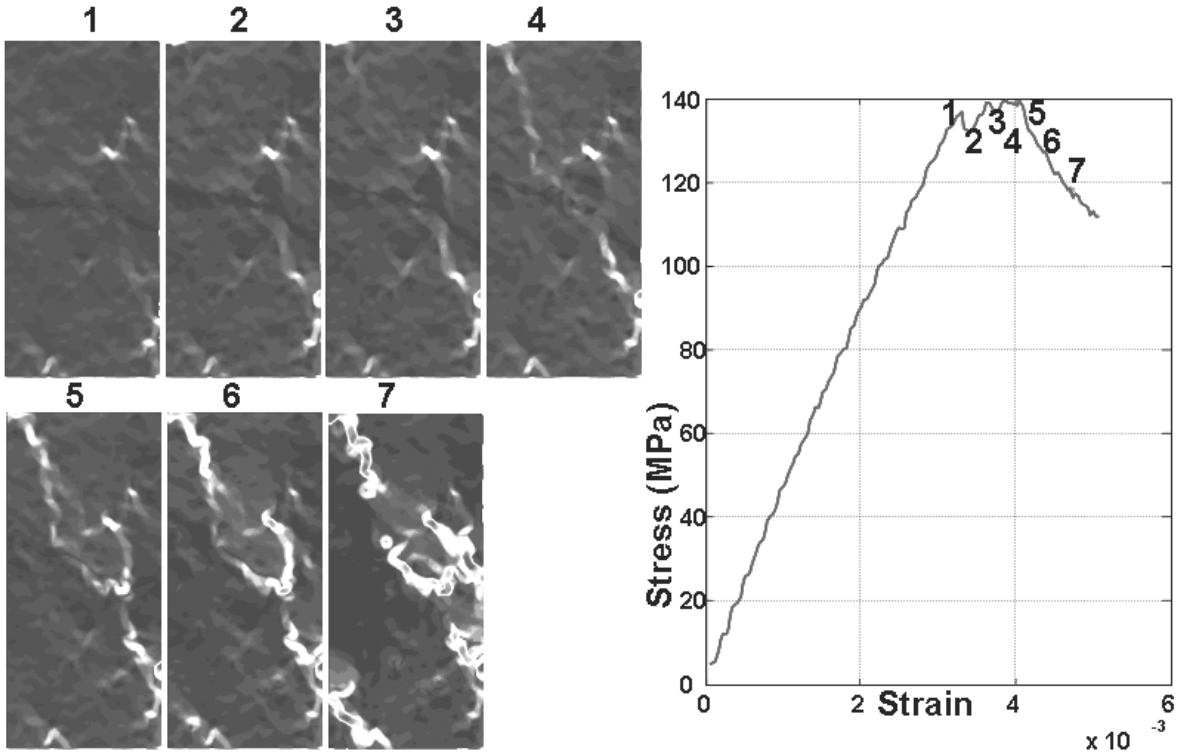

Figure 2.2: Time series of displacement gradients (see text) for sample 5U-4 at 0 MPa confining pressure. The localization in the modeled sample evolves from a distributed mode (darker colors) with very little deformation to a highly localized deformation (lighter colors) just after peak stress. This zone is approximately 4 particles wide.

which indicate a good match between the model and laboratory observations.

2.3.3 Strength Envelopes

Using the above results as a guide, we used an iterative process in an attempt to mimic the full compressive strength envelope of the rock as well as appropriate failure modes, using a single and unique set of micro-parameters. This entailed generating multiple DEM assemblies with the same microparameters and running simulations at the same confining pressures as the laboratory tests. Figure 2.3 shows the comparison between simulated and observed compressive failure envelopes for four different rock samples, at various confining pressures. The match is qualitatively consistent – the differences in the model results compared to the laboratory tests are well within the reproducibility of the laboratory test results. The clustered material appears to increase the overall slope of the compressive failure envelope, which is not attainable using unclustered material and realistic microparameters.

2.3.4 Stress-Strain Curves

In the DEM model, we calibrated the slope of the stress-strain curves to the intrinsic elastic properties of the rock. Both the observed and simulated differential stress versus axial strain and volumetric strain versus axial strain including load-unload loops are plotted in Figure 2.4 (See *Jaeger and Cook* [1969] for discussion of load-unload loops). The dashed lines indicate the curves for the simulated rock and the solid line the observed rock. Since the model is calibrated to the intrinsic elastic properties and not the damaged rock the stress-strain curves take on different forms, as illustrated in Figure 2.4a.

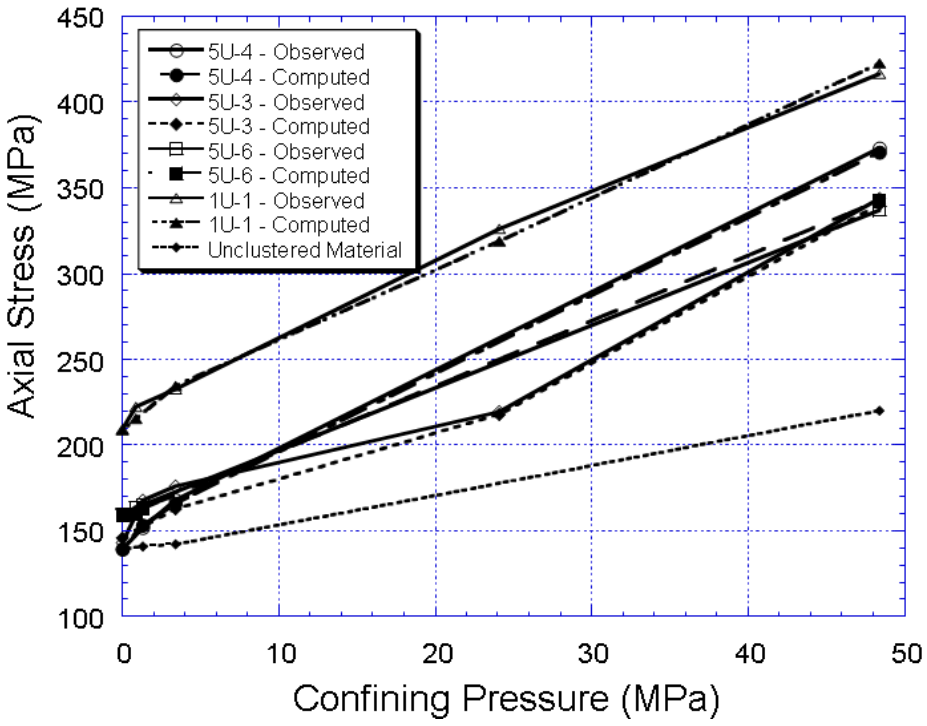

Figure 2.3: Simulated and observed compressive failure envelopes for 4 different groups of sedimentary rocks from the Midland Basin. Failure envelopes were determined by plotting peak stress at the given confining pressure. A good match is achieved through adjusting the main parameters controlling the slope of the compressive failure envelope, particle friction (0.5 in all models) and cluster size. Note the difference in slope between the unclustered material and the models in this study.

Much more strain is observed in the real rock due to processes not captured in the simulated rock, such as grain boundary sliding and preexisting cracks. The plots of volumetric strain versus axial strain (Figure 2.4b) highlight volume changes in the samples over the course of the triaxial tests. As sample loading begins, initial compaction takes place (positive volumetric strain) until approximately 0.9% axial strain, then a sharp increase in volume occurs. This is documented in both the laboratory and the model and is termed shear-enhanced dilation, common in low porosity, fined-grained sedimentary rocks [*Brace*, 1978; *Wong et al.*, 1992]. The simulated and observed stress-strain curves are quite similar in terms of their general trends in volume changes as well as timing of these events.

The post-peak behaviors in the simulated samples are quite different than in the laboratory as shown in Figure 2.4. This may be best explained by considering the stiffness of the testing machine vs. the model stiffness. In a very compliant system, as typically most triaxial compression devices are [*Shimamoto et al.*, 1980], a significant amount of energy is absorbed by the machine and consequently released upon failure of the sample. This energy causes inertial effects in the sample, rapid propagation of the shear fracture, and a steep drop in stress. Post peak comparison of stress-strain curves using this data is not possible.

2.4 Conclusions

The numerical approximation of the mechanical behavior of rock is difficult using traditional continuum-based models that typically are hampered by inadequate constitutive relationships governing crack initiation and growth.

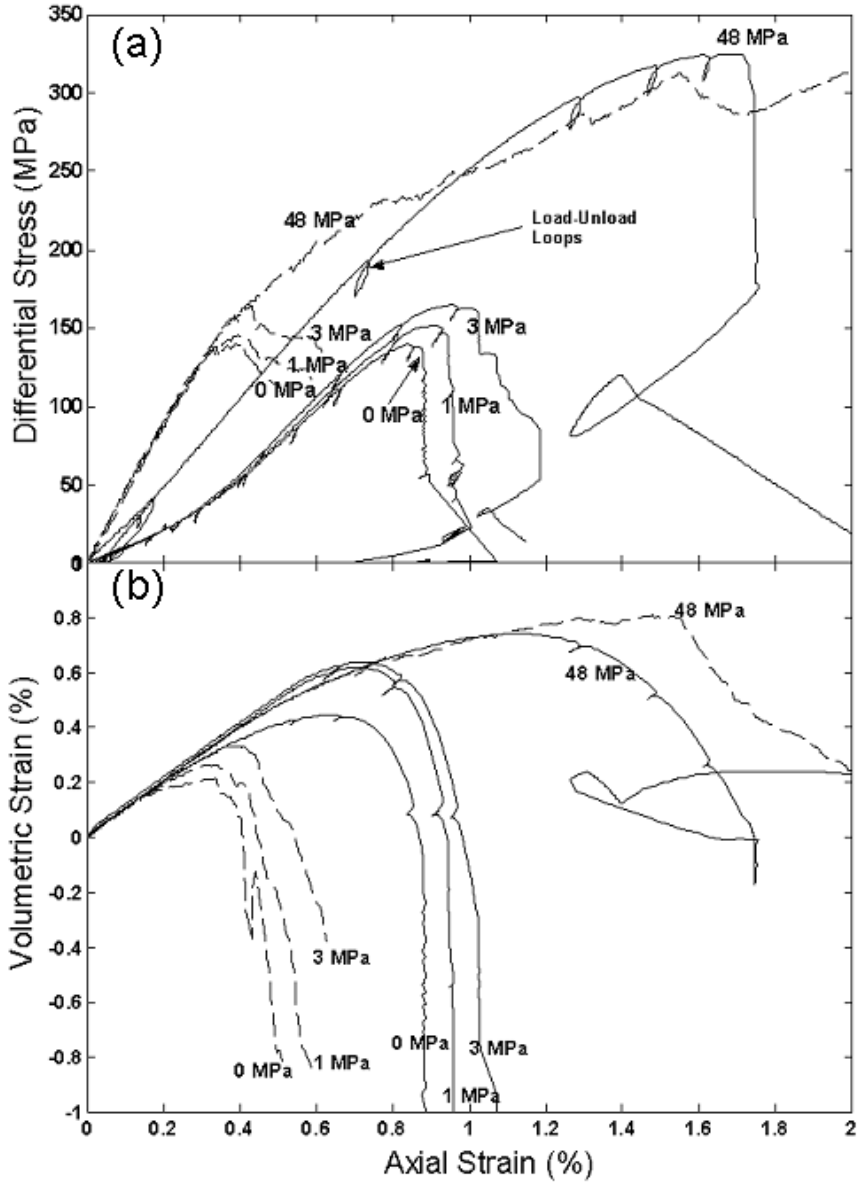

Figure 2.4: Simulated and observed differential stress and volumetric strain versus axial strain curves for sample 5U-4. Solid lines represent observed laboratory data at the confining pressure marked on the plot and dashed lines represent simulations. Differences in the position of the curves along the x axis are due to a choice in elastic parameter calibration (intrinsic versus damaged rock properties). The general trends in the curves are captured.

The discrete model applied in this study has been shown to match the observed laboratory data very well with model microparameters chosen by comparing elastic and inelastic material behavior. Calibrated models of rock behavior could be used to explore scaling relationships as well as provide insight into the micromechanics of rock fracture.

The modeled progression of strain localization in the samples is clearly captured with the calculated displacement gradients that indicate a good match between the model and laboratory observations. Post-peak comparison of stress-strain curves using data from a non-stiff triaxial machine is not possible. The ratio of shear to normal bond strength in the DEM plays an important role in strain localization. Clustered material appears to increase the overall slope of the compressive failure envelope, which is unattainable using un-clustered material and realistic microparameters. The simulated and observed stress-strain curves are quite similar in terms of their general trends in volume changes as well as timing of these events. Finally, by utilizing more than one calibration parameter, looking at failure envelopes and failure modes, we have identified microparameter relationships that would not be apparent otherwise.

References

Boutt, D., and B. McPherson, Discrete element models of the micromechanics of sedimentary rock: The role of organization vs. friction, *EOS Trans. AGU*, *82*, Abstract T32E–0913, 2001.

Brace, W., Volume changes during fracture and frictional sliding: A review, *Pure and Applied Geophysics*, *116*, 603–614, 1978.

Bruno, M., and R. Nelson, Microstructural analysis of the inelastic behavior of sedimentary rock, *Mechanics of Materials*, *12*, 95–118, 1991.

Cundall, P., A computer model for simulating progressive, large-scale movement in block rock systems, in *Rock fracture*, edited by Anonymous, vol. 1, Int. Soc. Rock Mech., France, 1971.

Cundall, P., and O. Strack, A discrete element model for granular assemblies, *Geotechnique*, *29*, 47–65, 1979.

Hazzard, J., P. F. Young, and S. Maxwell, Micromechanical modeling of cracking and failure in brittle rocks, *Journal of Geophysics Research*, *105*, 16,683–16,697, 2000.

Huang, H., E. Detournay, and B. Bellier, Discrete element modeling of rock cutting, in *Rock Mechanics for Industry*, edited by Amadei, Kranz, Scott, and Smealie, pp. 123–130, A.A. Balkema, Rotterdam, 1999.

Itasca Consulting Group, I., PFC2D/3D (Particle Flow Code in 2/3 Dimensions) Version 2.0, ICG, Minneapolis, Minnesota, 1999.

Jaeger, J., and N. Cook, *Fundamentals of Rock Mechanics*, 2nd ed., Chapman and Hall, London, 1969.

Li, L., and R. Holt, Simulation of flow in sandstone with fluid coupled particle model, in *Proceedings of the 38th U.S. Rock Mechanics Symposium: Rock Mechanics in the National Interest*, edited by D. Elsworth, J. P. Tinucci, and A. Heasley, pp. 511–516, A.A. Balkema, Rotterdam, 2001.

Lockner, D. A., Rock failure, in *Rock physcis and phase relations: A handbook of physcial constants*, edited by T. J. Ahrens, vol. 3, p. 295, AGU, Washington, 1995.

Lorenz, J., J. Sterling, D. Schecter, C. Whigham, and J. Jensen, Natural fractures in the Spraberry Formation, Midland basin, TX: The effects of mechanical stratigraphy on fracture variability and reservoir behavior, *AAPG Bulletin*, *86*, 504–524, 2002.

Menendez, B., W. Zhu, and T.-f. Wong, Micromechanics of brittle faulting and cataclastic flow in Berea sandstone, *Journal of Structural Geology*, *18*, 1–16, 1996.

Morgan, J., and M. Boettcher, Numerical simulations of granular shear zones using the distinct element method 1. Shear zone kinematics and the micromechanics of localization, *Journal of Geophysical Research*, *104*, 2703–2719, 1999.

Potyondy, D., P. Cundall, and C. Lee, Modeling rock using bonded assemblies of circular particles, in *Rock Mechanics: Tools and Techniques*, edited by Aubertin, Hassani, and Mitri, pp. 1937–1944, A.A. Balkema, Rotterdam, 1996.

Potyondy, D. O., A bonded-disk model for rock: Relating microproperties and macroproperties, in *Discrete Element Methods: Numerical Modeling of Discontinua*, edited by B. K. Cook and R. P. Jensen, vol. 1, pp. 340–345, ASCE, Santa Fe, NM, 2002.

Potyondy, D. O., and P. A. Cundall, A bonded-particle model for rock, *International journal of rock mechanics and mining sciences*, In Press.

Shimamoto, T., J. Handin, and J. M. Logan, Specimen-apparatus interaction during stick-slip in a triaxial compression machine: A decoupled two-degree-of-freedom model, *Tectonophysics*, *67*, 175–205, 1980.

Sterling, J. L., Fracture generation and fluids in the Spraberry Formation, Midland basin, Texas, Masters - independent study, New Mexico Institute of Mining and Technology, 2000.

Wang, Y.-C., X.-C. Yin, F.-J. Ke, M.-F. Xia, and K.-Y. Peng, Numerical simulation of rock failure and earthquake process on mesoscopic scale, *Pure and Apllied Geophysics*, *157*, 1905–1928, 2000.

Wong, T.-f., H. Szeto, and J. Zhang, Effect of loading path and porosity on the failure mode of porous rocks, *Appl. Mech. Rev.*, *45*, 281–293, 1992.

CHAPTER 3

APPLICATION OF DISCRETE ELEMENT MODELING TO UNDERSTANDING THE FORMATION OF SHEAR FRACTURES IN THE SPRABERRY TREND, MIDLAND BASIN[1]

Abstract

The Spraberry Formation in the Permian Basin, Texas, is a textbook example of a highly fractured formation, including extension and shear fractures. Within local areas of the Midland Basin, at least two sets of natural fractures exist in two reservoir intervals, but exhibit different characteristics. One hypothesis regarding the genesis of Spraberry Formation fractures is that high fluid pressures reduced effective stresses during the basin's geologic history, allowing ambient but unremarkable (i.e. very low) tectonic stresses to induce failure. Another hypothesis is that weak Laramide-age compressional stresses alone caused the fracture sets. Initial modeling of basin evolution suggests that high pore fluid pressures were not attained, at least at regional scale. Therefore we explore the possibility of inelastic deformation in the absence of high fluid pressures. We focus on this point, using a calibrated DEM model of Spraberry Formation strata to investigate whether weak compressional forces of the Laramide

[1]Portions of this chapter have been submitted to *GEOFLUIDS*: McPherson, B.J.O.L. Boutt, D.F. The role of fluids in causing fracturing in the Spraberry Trend, Midland Basin.

orogeny could have caused the shear fractures to form. Despite model limitations, 2-D plane parallel model (modeling shear mode only) and current-day rock properties, simulation results suggest that a mild compressional episode of geologically short duration may induce deformation, in the form of shear fractures. The interactions between mechanically distinct units are observed to deflect and transfer stresses resulting in more deformation in some beds and restricting deformation in others compared to a homogeneous model. Characterization of the mechanical properties, such as the Young's modulus and Failure strength, of significant lithologic units could enable a better understanding of the role of mechanical stratigraphy in tectonically quiescent basin settings.

3.1 Introduction

The hydrodynamic regimes of deep sedimentary basins are usually affected, and often controlled, by fractures. Much research has been devoted to understanding the effects of faults and fractures on fluid flow patterns (e.g., *McCaig* [1989]; *Forster and Evans* [1991]; *Nordqvist et al.* [1992]; *Bai et al.* [1993]; *Caine et al.* [1996]). Many studies specifically acknowledge that fractures form in the presence of fluids with fluid pressures at or above hydrostatic, some examples being *Hubbert and Rubey* [1959], *Secor* [1965], *Atkinson* [1984], *Pollard and Aydin* [1988], *Boone and Ingraffea* [1990], *Lorenz et al.* [1991], *Cheng et al.* [1993], and *Renshaw and Harvey* [1994]. For example, *Secor* [1965] used the concept of effective stress outlined by *Hubbert and Rubey* [1959] to show that tensile fractures form under compressive stress if pore fluid pressures are great enough. More recent studies, for example *Boone and Ingraffea* [1990] and *Ren-*

shaw and Harvey [1994], focus on poroelasticity and crack-tip modeling using sophisticated coupled finite element and finite difference models.

This study builds on these earlier works, with a primary hypothesis that is fairly specific: fractures commonly form preferentially in overpressured areas of sedimentary basins, inasmuch as high fluid pressures facilitate the formation of fractures and regional-scale fracture networks. In other words, fluid pressures may reduce effective stresses enough to permit otherwise insufficient tectonic stresses to induce fracturing.

The Spraberry Formation in the Midland Basin, Texas, is a highly fractured formation that has been deemed the "largest uneconomic oil field in the world" [*Guevara*, 1988]. Fracture genesis in the Spraberry Formation has been attributed to range of possible forces. Changes in sediment volume due to compaction, regional tension and local uplift were all possible mechanisms cited by *Warn and Sidwell* [1953] and *Guevara* [1988]. Another hypothesis has been that the fractures are due to a weak force sustained over a long period of time [*Schmitt*, 1954]. *Winfree* [1995] and *Lorenz et al.* [2002] suggest that compressional forces exerted on the region during the Laramide orogeny are the primary cause of fracturing, whereas *Sterling* [2000] suggests that high fluid pressures during the basin's history likely played an important role in fracture genesis.

Modeling of basin evolution suggests that high pore fluid pressures were not attained, at least at regional scale. Therefore it is useful to explore the possibility of inelastic deformation in the absence of high fluid pressures. Rather than provide a systematic test of different options, will focus on this

point, using a regional-scale approach and geologically reasonable loading parameters. Our regional-scale approach is particularly suitable for the Midland Basin because of its very simple structure and stratigraphy, and its simple geologic history. Additionally, fractures in this basin appear to be regional-scale in origin as suggested by the fact that fractures produced by local flexure would not have regional parallel orientations [*Winfree*, 1995]. The parallel orientation of fractures across the entire region suggests that the fractures formed by a large-scale mechanism probably associated with regional tectonic compression [*Lorenz et al.*, 1991; *Winfree*, 1995], perhaps in tandem with the regional-scale overpressuring that is common to many sedimentary basins [*Law and Spencer*, 2000]. We are restricted to use the current rock properties, which may or may not be similar to those of the rocks during the laramide, and investigate model response to end load using a 2D plane parallel model. Thus, are effectively investigating out-of-plane deformation (which precludes consideration of extension fractures) of system similar to present-day system. Although not a comprehensive approach, this is nevertheless a good beginning point for considering mechanics of an evolving basin.

3.2 Geologic Setting and Background

The Midland basin consists of shallow-marine shelf to shelf-margin carbonate and deep-basin deposits of Pennsylvanian and Permian age [*Galley*, 1958; *Handford*, 1981; *Guevara*, 1988]. Figure 3.1 includes a structure-contour map of the upper Spraberry Formation (adapted from *Bai* [1989]) for a 64 km by 31 km area within the basin, illustrating that the Spraberry Formation is generally homoclinal with a gentle dip of less than 1^o to the west and into

the deepest part of the basin. The Spraberry Formation lies between units of contrasting mechanical and hydrologic properties. The Spraberry Formation consists of a series of interbedded sands and shales, ranging in thickness from 200 m at the margins to 400 m at the basin's depositional center [*Stanley et al.*, 1951; *Guevara*, 1988]. These sediments are interpreted as submarine fan complex deposits [*Tyler and Gholston*, 1988; *Guevara*, 1988]. In recent literature, the Spraberry Formation has been divided into sub-units, primarily to distinguish between areas of high and low oil production [*Guevara*, 1988; *Lorenz et al.*, 2002]. In particular, the 10 to 15 feet thick 1U and 5U sands of the Spraberry Formation are designated as the most productive reservoir units in the Midland County area, but production is rare to nonexistent in shale layers [D. Schechter, personal communication, 1998].

3.2.1 Observed Fractures

Extensive natural fractures are observed in the Spraberry Formation, despite its stable geologic setting with minimal folding and faulting [*Lorenz et al.*, 2002]. Analysis of horizontal core from the E. T. O'Daniel #28 well indicated that a minimum of three sets of fractures are observed in the upper Spraberry Formation. The three sets are different in orientation, location, spacing, type and mineralization (Figure 3.2). The first set consists of extension fractures that have a northeast strike (average 43^o; Figure 3.2). These northeast (NE) striking fractures are limited to the 1U sand and silt reservoir facies, and have a low variability in strike [*Lorenz et al.*, 2002]. The second set consists of right-lateral shear fractures that strike north-northeast (average 32^o; Figure 3.2). This set is only observed in sand and silt layers in the 5U.

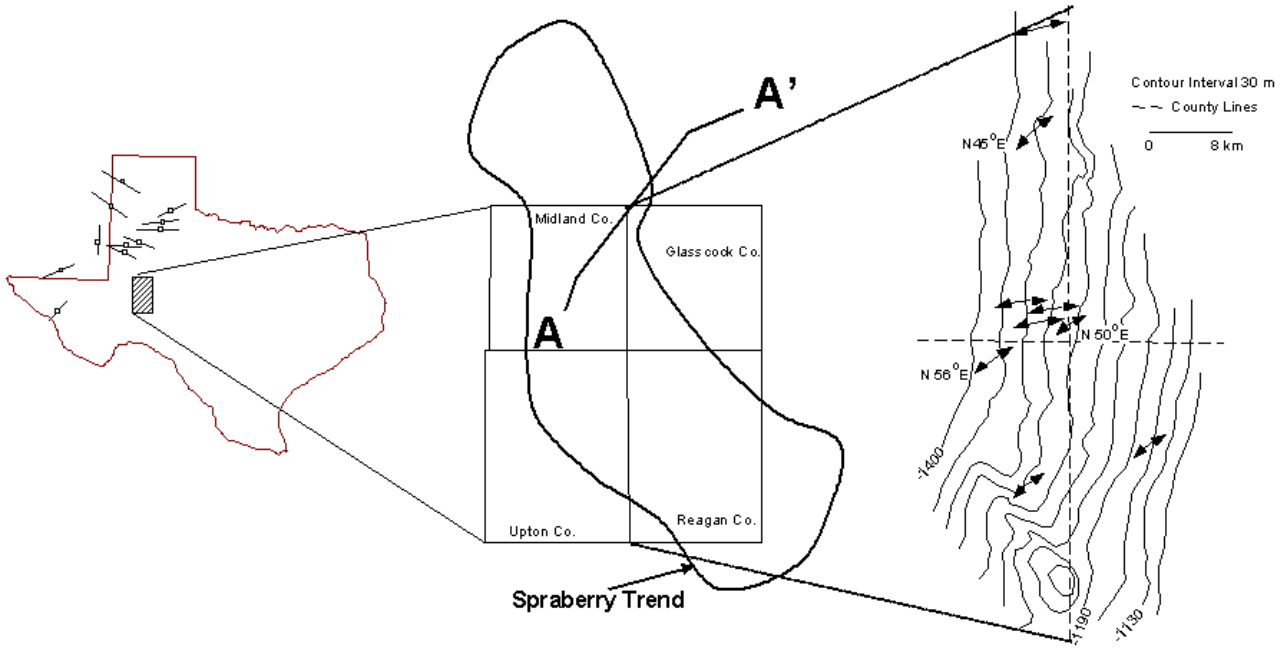

Figure 3.1: Structure contour map of upper Spraberry Formation, (right; from *Bai* [1989]) illustrating the relatively simple structure of the area. Location of contour map area shown on map of Texas (left). Shown on the contour map are fracture orientations (determined by *Bai* [1989]); shown on the map of Texas are major horizontal compressive stress orientations (from *Zoback and Zoback* [1989]). Outline of Spraberry trend shown in center schematic. Also shown on center schematic is the location of the cross-section A-A'.

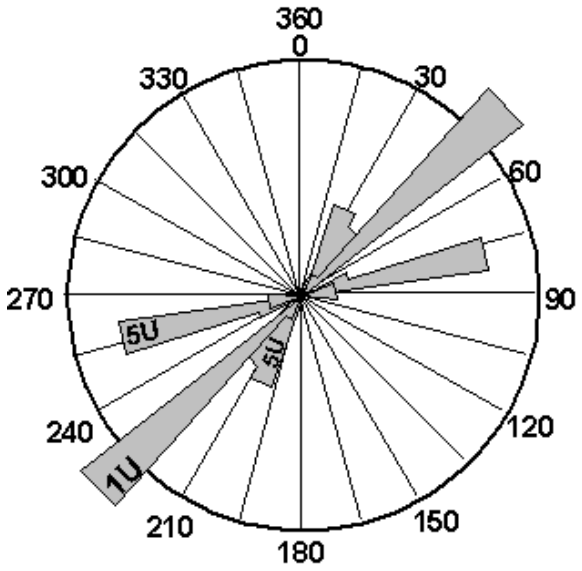

Figure 3.2: Rose diagram showing the trends of observed fracture sets in the Spraberry Formation.

The last fracture set strikes east-northeast (average 70^o), and also includes extension fractures. This set is observed within the 5U-reservoir sand and silt unit, as well as within the black shales that overlie both 1U and 5U reservoirs. *Lorenz et al.* [2002] provides a thorough description and analysis of observed fractures in the Spraberry Formation within the area of interest of this study.

3.2.2 Possible Fracture Mechanism

Observed fractures in the Spraberry Formation (Figure 3.2) provide a number of clues about the potential forces and orientations of stresses that caused them. The geometry of observed shear fracture sets in the Midland basin suggests that at the time of failure, σ_1 was horizontal and trended northeast or northwest. Two sets of surface lineaments and fractures, strik-

ing both northeast and northwest, were observed and described by *Stanley et al.* [1951] and *Guevara* [1988], and were linked genetically to Spraberry Formation shear fractures by *Stanley et al.* [1951]. If this analysis is correct, it suggests that Spraberry Formation fractures formed since the deposition of surface sediments in the early Cretaceous, coincident with timing of the Laramide orogeny, $\sim 80 - 40$ Ma. The inferred northeasterly orientation of σ_1 is also consistent with the direction of weak regional compressive forcing imparted by the Laramide orogeny. Recent sonic velocity anisotropy orientation measurements of Spraberry Formation core suggest that present-day stresses are oriented in the northeastern direction, too [D. Holcomb, written communication, 1998]. Additionally, *Winfree* [1995] suggests that subsequent extension has helped maintain or keep fractures open. In sum, this evidence suggests that fractures in the Spraberry Formation could possibly be related to Laramide forces, whether caused exclusively by compressional forces and maintained by extension, or by a combination of these forces with elevated fluid pressures, as discussed in *McPherson and Boutt* [Accepted].

3.3 Role of Laramide Compression in Fracture Formation

The basin evolution model analysis presented in *McPherson and Boutt* [Accepted] suggests that high fluid pressures were not likely to have formed in the Midland basin during its history. At the minimum, observed present-day rock properties do not favor overpressuring. Based on these results, it is concluded that elevated fluid pressures probably played a minor role, if any, in causing observed fractures in the Spraberry Formation. We turn our attention to whether or not inferred low strain rates (resulting from small stresses) asso-

ciated with the Laramide orogeny could induce significant fracturing, unaided by high fluid pressures. This issue is addressed using a 2-dimensional (2-D) discrete element method (DEM) modeling approach.

3.3.1 DEM Model of Laramide Compression

The DEM entails simulating the mechanical behavior of rock by idealizing the system as a collection of separate particles bonded together at their contact points and utilizing the breakage of individual structural units or bonds to represent damage [*Cundall and Strack*, 1979; *Cundall*, 1986; *Potyondy et al.*, 1996]. Each particle has unique properties and represents a collection of mechanical units. The particles do not represent grains, but are meant to discretize space much like cells or elements in continuum models. This method is unique because of its inherent ability to represent damage or fractures in a direct fashion as well producing realistic non-linear behavior using simple contact laws governed by Newtonian mechanics [*Saltzer and Pollard*, 1992; *Hazzard et al.*, 2000; *Potyondy and Cundall*, In Press]. Details of model input parameters and algorithms used in DEM code for the modeling is provided Chapter 2 and *Potyondy and Cundall* [In Press].

Our DEM model was calibrated to the measured mechanical properties of the Spraberry Formation calculated from laboratory triaxial tests that are detailed by *Sterling* [2000]. Details of the calibration process are described by *Boutt and McPherson* [2001] and *Potyondy and Cundall* [In Press]. Rocks from each individual sub-unit of the Spraberry Formation were calibrated separately and the parameters recorded.

DEM assemblies were built by generating particles through the fill and expand technique with a uniform normal distribution to completely fill the domain of interest, and then compacted until a low isotropic stress was achieved. The final step was assignment of the parameters to the Spraberry Formation model units. Boundary conditions assigned to the top and bottom of the model were constant stress (representing the minimum stress direction). This implies that the assembly can strain from the top and the bottom, but the overall stress will remain constant. This is justified because the assembly was loaded to emulate the burial conditions imposed on the unit during the Laramide orogeny. As predicted by the burial history [*McPherson and Boutt*, Accepted], the amount of overburden on the unit during the Laramide orogeny was essentially constant, therefore no change in the minimum stress was imposed. The boundary conditions on the sides of the model were assigned as constant strain rate. No measured strain or shortening rates for the Midland basin exist, and therefore we used a strain rate typical of mildly compressive regions [*Twiss and Moores*, 1992]: a strain rate of $3 * 10^{-}17\frac{1}{s}$ wasapplied for 5.4 Ma, inducing a cumulative strain of 0.0051 or 0.51 % in the direction of compression. This strain is significantly higher than those reported by *Lorenz et al.* [2002]. They reported a strain of 0.1 % for extension fractures parallel to the assumed maximum stress direction during the Laramide. Given that this strain is normal to our direction of compression and the small Poisson's Ratio reported for these rocks (0.03-0.11), our value of strain rate used is very appropriate. This amount of strain is also consistent with the lack of structures found within the Midland Basin [*Winfree*, 1995].

Our modeling results are limited by the two-dimensionality of the

model. It is well established that the fractures present in the Spraberry Formation are three-dimensional structures. In this initial idealization, we chose to model 2-D sections oriented parallel to the assumed shortening direction. This is justified because (1) boundary conditions are established for this section and (2) a wealth of information exists for stratigraphy in this orientation. As a consequence of modeling this particular section we are not able to resolve the exact orientation of fractures observed in the Spraberry Formation. Instead, we are simply attempting to show whether, for a given set of material properties, the assumed strain rates were or were not large enough to cause deformation in the Spraberry Formation.

Plots of results are generated by first gridding the cumulative displacements for all particles in the DEM model for a timestep and then taking the spatial gradients of the resultant vectors (See Chapter 2 for an example). This technique highlights differential movements in the assembly by highlighting areas where strong contrasts in displacements occur. A fracture or fault marks a discontinuity in an otherwise coherent medium and thus will show a strong gradient of overall movement (cumulative displacement) with respect to some coordinate system. Figure 3.3 depicts results of a homogeneous one layer model of the Spraberry Formation. The boundary conditions are depicted in Figure 3.3. The estimated Laramide strain rate described above was applied as the side boundary conditions. This model is composed of 5U rocks and the elastic properties of the rock type is summarized in Table 3.1.

Displacement gradients are also shown in Figure 3.3. The deformation field is very heterogeneous, highlighted by distinct regions of high magnitude

Table 3.1: Elastic and in-elastic data for units used in the 1-layer and 3-layer models.

Property	1U-3	5U-6	3 Layer Model
Young's Modulus (GPa)	40.2	20.8	20
Poisson's Ratio	0.088	0.112	0.03
Failure Strength (MPa)	250.3	159.2	N/A
Bulk Modulus (GPa)	N/A	N/A	12.2

displacement gradients (brighter regions of Figure 3.3). Large displacement gradients exist throughout the model and are coincident with the occurrence of bond breakages between the individual discrete elements.

These deformation patterns (Figure 3.3) are not apparent from simply examining the cumulative displacement field; the gradients must be calculated. We interpret these patterns to represent areas of strain localization where adjacent regions are undergoing differential movement. That is to say that the regions represent discontinuities, or in this case, shear fractures, consistent with the interpretations of *Lorenz et al.* [2002]. In sum, even for the relatively small strain rates applied, distinct deformation zones form in the model. We suggest that the relatively weak compression rates associated with the Laramide orogeny are sufficient to induce deformation, without the need for excessive fluid pressures to reduce effective stress.

3.3.2 Fracture Variability: DEM Model Simulations

We believe that mechanical interactions (both inelastic and elastic) or stress amplifications (see *Lorenz et al.* [1991] and *Eshelby* [1957]) among the units of the Spraberry Formation may cause variability in induced fractures. This hypothesis suggests that elastic and inelastic behavior of any given rock

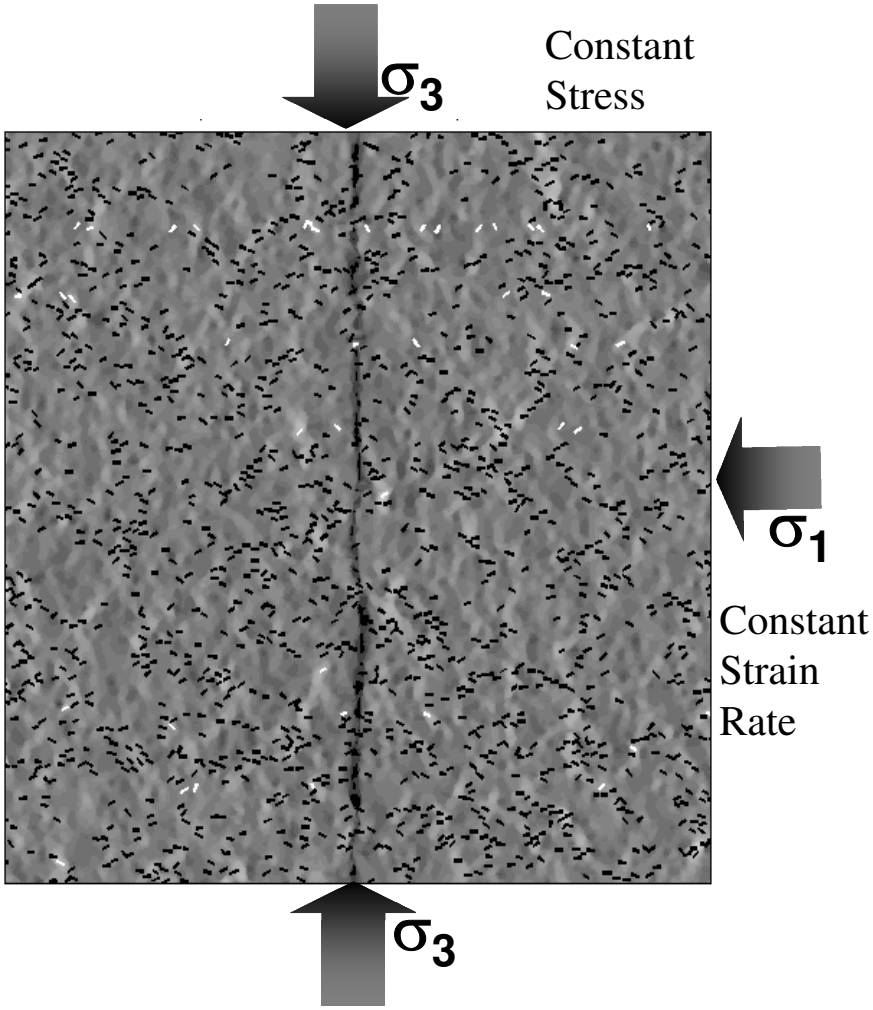

Figure 3.3: Results of the 5U simulation plus boundary conditions. Spraberry Formation strata consist of thin reservoir sands surrounded by thicker fine grained silts and shales. Resultant displacement gradient contours of the 5U model show significant deformation. It is possible that the properties of the surrounding units may influence how individual units behave mechanically.

unit is influenced by the surrounding rock units. In other words, the effective elastic and inelastic properties of a suite of units may be different from the properties of the individual units. We used 2-dimensional DEM models to evaluate this problem.

Scaled DEM models of the Spraberry Formation stratigraphy were assembled using the calibrated parameters. We assembled 3-layer models in the vertical direction, rather than a homogeneous model in the horizontal direction (Figure 3.3), attempting to capture the physics of mechanical interactions between layers. The top and bottom boundary condition was set to the overburden load as determined via the basin evolution model. We examined several different scenarios using a combination of the different material properties of the Spraberry Formation. The model discussed here is a 5U reservoir sandstone sandwiched between 2 equally thick 1U shales. The significance of reconstructing a heterogeneous set of units (i.e. mechanical stratigraphy) is that they may influence each other in terms of their abilities to transfer and deflect stresses.

Simulation results are depicted in Figure 3.4. This model has two equally thick outer layers (50 % of total thickness) of the properties of the Spraberry Formation 1U-3 unit and one middle layer of the 5U-6 unit which also makes up 50 % of the thickness. The elastic and inelastic properties for these units are summarized in Table 3.1. The geometry is illustrated in Figure 3.4b by the dashed lines. The 1U-3 unit is much stronger and stiffer, both in terms of its unconfined failure strength and its modulus of elasticity, compared to the 5U-6 unit. The strength of the bonds between layers was assigned as the average of the of the 1U-3 and 5U-6 layers. Results suggest this

heterogeneity has a strong influence on the behavior of the systems. Figure 3.4a depicts a gridded, filled contour plot of cumulative spatial displacement. The overall direction of the displacement vectors is horizontal and towards center, indicative of compression. We observed small changes in the direction of the displacement vectors at a local scale. Spatial displacement gradients of this field (Figure 3.4b) show a heterogeneous deformation field.

We suggest that the units are responding differently to the applied stress solely because of contrasts in their properties. To isolate or highlight contrasts in behavior among the two units, we subtracted the 5U-6 displacement gradient results shown in Figure 3.4b from those for a 1-layer (i.e., homogeneous) model with the properties of the 5U-6 unit (Figure 3.3). This is depicted in Figure 3.4c, illustrating a distinct difference from the homogeneous case by having non-zero displacements in the middle layer. The organization of the displacement gradients of the 5U-6 layer suggests that this layer is undergoing strain localization differently than that observed for the homogeneous case.

Lastly we examined the effect of relative proportions of the 1U and the 5U on the overall failure behavior of an ensemble. Simulations with 0, 25, 50, 75, and 100 percent 1U units were generated with the same dimensions as described above. In all cases where the 5U unit was present, it was placed between two 1U layers with thicknesses of that given by the above percentages. For example, the model described above is the 50 % case where the 5U unit is sandwiched between two smaller 1U units. In these cases we loaded the layered system until failure, as determined by a loss in strength of the assembly, and the time of failure was noted.

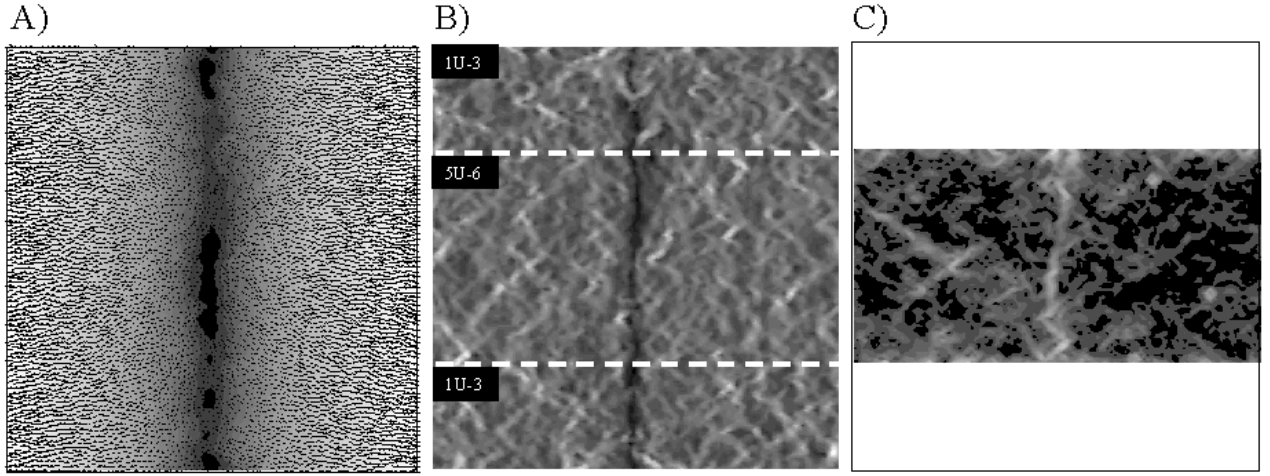

Figure 3.4: DEM simulation results. (A) Cumulative particle displacements and associated displacement vectors, (B) spatial displacement gradients, (C) residual displacement gradients of middle layer.

Figure 3.5 depicts curves showing the stress parallel to loading versus time to failure for the assemblies composed of the different percentages of 1U and 5U units. The two end-members, 0% and 100 % 1U, show very different magnitudes and the timing of peak stress. The 100 % 1U simulation reaches peak stress first and attains the highest stress whereas the 0 % 1U simulation is the exact opposite, showing the lowest peak stress reached after the longest amount of time. The two simulations also differ in terms of the shape of their stress versus time curves. The more brittle 100 % 1U simulation shows a more pronounced failure peak which is quite different than the 0 % 1U simulation with a more rounded and smoothed peak.

It might be expected that the intermediate percentage simulations would follow a linear transition from 0% to 100% 1U behavior. This is clearly not the case (Figure 3.5). The smallest percentage of 1U, 25%, is much stronger than the 0% 1U and also fails much sooner. Its strain curve is more similar to the 100% 1U simulation than to the 0% 1U simulation. The rest of the intermediate percentages follow a similar pattern. These results indicate that even small percentage of the stronger and more brittle 1U units influences the mechanical behavior of the package as a whole. In fact, they can even alter the timing and location of failure as shown in this and the previous section. Of course, these simulations assume a constant strain rate, but if the period of loading is short these results imply that some layers will fail whereas other will not.

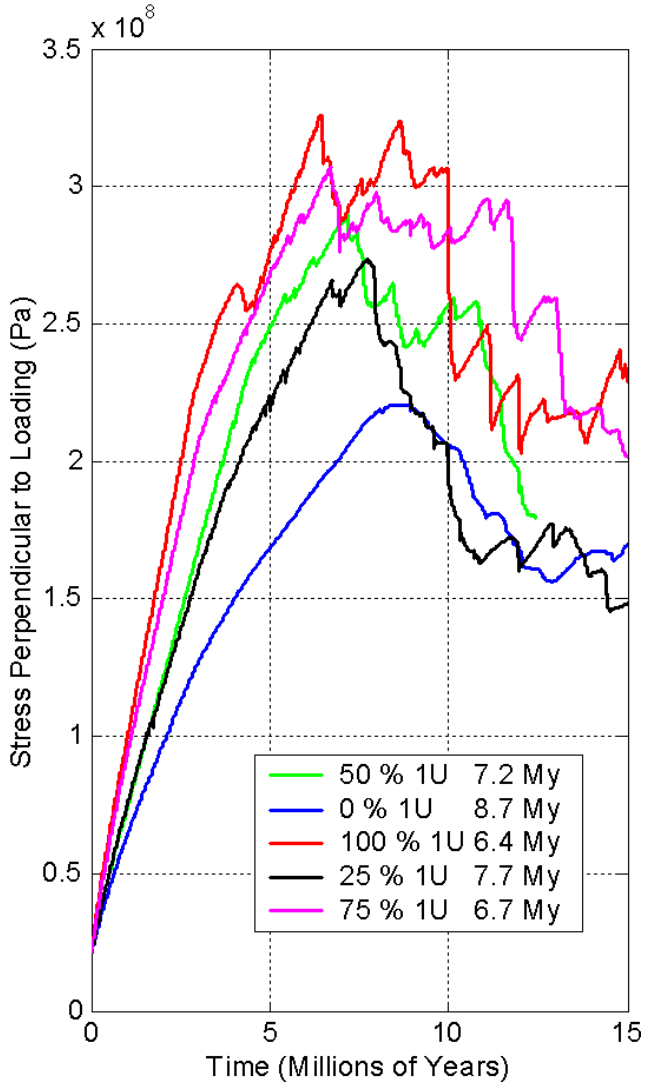

Figure 3.5: Stress perpendicular to loading v.s. simulation time for assemblies composed of the stated percentages of 1U and 5U units. The different percentages of the units tend to lower the affect both the strength of the unit and the timing of failure.

3.4 Conclusions

A discrete element model was used to simulate geomechanical aspects, including elastic and inelastic rock behavior. Our primary goal was to determine whether fluid pressures were required for shear fracture genesis, or if regional tectonic forces alone could produce them.

Our basin evolution model simulation results [*McPherson and Boutt*, Accepted] suggest that high fluid pressures did not occur during the basin's history. Furthermore, the DEM simulations suggest that such fluid pressures are not necessary to explain the origin of observed fractures, and that fractures may form during a mild compressional episode of geologically short duration, without excessive fluid pressures. Results of our study support the findings and interpretations of *Lorenz et al.* [2002].

In sum, important conclusions include:

- Simulations using estimated Laramide strain rates suggest that a mild compressional episode of geologically short duration can induce shear fractures without excessive fluid pressures.
- Simulation results of the 3-layer DEM models suggest that mechanical interactions between distinct units with different properties influence the overall mechanical behavior of the system as well as the local behavior.

Additionally, the layered heterogeneous models provide other insight regarding the general elastic and in-elastic mechanical interactions of layered systems under controlled conditions. More commonly applied analysis using single layer properties and assumptions of homogeneous stress fields (Mohr

circles) may not be adequate to capture the full range of physical processes occurring in a layered system.

Our results have important implications for fracture prediction. The initial plan was to simulate the mechanical evolution of the unit from deposition to burial, but we abandoned it when simulation results included complete failure (deformation) only 15 Ma into the burial history. This result was intuitive since the model was calibrated using experimental results associated with present-day, completely lithified rock core, and burial rates during initial compaction are relatively high during initial portions of the burial history. In other words, we were simulating the strata's full geologic history, albeit the rock properties pertained only to the present-day, final state. It is clear that we are limited to simulating mechanical behavior during a window of time in which the present day mechanical properties may more closely match those during which the fractures formed.

References

Atkinson, B., Subcritical crack growth in geological materials, *Journal of Geophysical Research*, *89*, 4077–4114, 1984.

Bai, M., D. Elsworth, and J. Rogiers, Multiporosity/multipermeability approach to the simulation of naturally fractured reservoirs, *Water Resources Research*, *29*, 1621–1633, 1993.

Bai, R., Optimizing hydraulic-fracture length in the Spraberry trend, *SPE Formation Evaluation*, *September*, 1989.

Boone, T. J., and A. R. Ingraffea, A numerical procedure for simulation of hydraulically-driven fracture propagation in poroelastic media, *I. J. for Num. Anal. Meth. Geomech.*, *14*, 27–47, 1990.

Boutt, D., and B. McPherson, Discrete element models of the micromechanics of sedimentary rock: The role of organization vs. friction, *EOS Trans. AGU*, *82*, Abstract T32E–0913, 2001.

Caine, J., J. Evans, and C. Forster, Fault zone architecture and permeability structure, *Geology*, *24*, 1025–1028, 1996.

Cheng, A.-D., Y. Abousleiman, and J.-C. Roegiers, Review of some poroelastic effects in rock mechanics, *International Journal of Rock Mechanics and Mining Sciences and Geomechanics Abstracts*, *30*, 1119–1126, 1993.

Cundall, P., Distinct element models of rock and soil structure, in *Analytical and Computational Methods in Engineering Rock Mechanics*, edited by E. Brown, pp. 129–163, Allen and Unwin, London, 1986.

Cundall, P., and O. Strack, A discrete element model for granular assemblies, *Geotechnique*, *29*, 47–65, 1979.

Eshelby, J., The determination of the elastic field of an elliptical inclusion, and related problems, *Proceedings of the Royal Society, A.*, *241*, 376–396, 1957.

Forster, C., and J. Evans, Hydrogeology of thrust faults and crystalline thrust sheets; results of combined field and modeling studies, *Geophysical Research Letters*, pp. 979–982, 1991.

Galley, J., Oil and geology in the Permian basin of Texas and New Mexico, in *Habitat of Oil*, edited by L. Weeks, pp. 395–446, AAPG, Houston, 1958.

Guevara, E., Geological characterization of Permian submarine fan reservoirs of the Driver waterflood unit, Spraberry Trend, Midland basin, Texas, *Report of Investigations 172*, Bureau of Economic Geology, Austin, Texas, 1988.

Handford, C., Sedimentology and genetic stratigraphy of Dean and Spraberry Formations (Permian), Midland basin, west Texas, *APPG Bulletin*, *65*, 1602–1616, 1981.

Hazzard, J., P. F. Young, and S. Maxwell, Micromechanical modeling of cracking and failure in brittle rocks, *Journal of Geophysics Research*, *105*, 16,683–16,697, 2000.

Hubbert, M., and W. Rubey, Role of fluid pressure in mechanics of overthrust faulting, *GSA Bulletin*, *70*, 115–166, 1959.

Law, B., and C. Spencer, Compressive failure of mudstone samples containing quartz veins using rapid ae monitoring: The role of asperities, *Tectonophysics*, *328*, 329–340, 2000.

Lorenz, J., J. Sterling, D. Schecter, C. Whigham, and J. Jensen, Natural fractures in the Spraberry Formation, Midland basin, TX: The effects of mechanical stratigraphy on fracture variability and reservoir behavior, *AAPG Bulletin*, *86*, 504–524, 2002.

Lorenz, J. C., L. W. Teufel, and N. R. Warpinski, Regional fractures i: A mechanism for the formation of regional fractures at depth in flat-lying reservoirs, *AAPG Bulletin*, *75*, 1714–1737, 1991.

McCaig, A., Geology; fluid flow through fault zones, *Nature*, *340*, 600, 1989.

McPherson, B., and D. Boutt, The role of fluids in causing fractures in the Spraberry Trend, Midland basin, *GEOFLUIDS*, Accepted.

Nordqvist, A., Y. Tsang, C. Tsang, B. Dverstop, and J. Andersson, A variable aperture fracture network model for flow and transport in fractured rocks, *Water Resources Research*, *28*, 1703–1713, 1992.

Pollard, D. D., and A. Aydin, Progress in understanding jointing over the past century, *GSA Bulletin*, *100*, 1181–1204, 1988.

Potyondy, D., P. Cundall, and C. Lee, Modeling rock using bonded assemblies of circular particles, in *Rock Mechanics: Tools and Techniques*, edited by Aubertin, Hassani, and Mitri, pp. 1937–1944, A.A. Balkema, Rotterdam, 1996.

Potyondy, D. O., and P. A. Cundall, A bonded-particle model for rock, *International journal of rock mechanics and mining sciences*, In Press.

Renshaw, C. E., and C. F. Harvey, Propagation velocity of a natural hydraulic fracture in a poroelastic medium, *Journal of Geophysical Research*, *99*, 21,667–21,677, 1994.

Saltzer, S. D., and D. D. Pollard, Distinct element modeling of structures formed in sedimentary overburden by extensional reactivation of basement normal faults, *Tectonics*, *11*, 165–174, 1992.

Schmitt, G., Genesis and depositional history of Spraberry Formation, Midland basin, Texas, *AAPG Bulletin*, *38*, 1957–1978, 1954.

Secor, D. T., Role of fluid pressure in jointing, *American Journal of Science*, *263*, 633–646, 1965.

Stanley, T., S. Levinson, P. Masson, W. Pratt, and A. Osanik, Geological investigation of the 'Spraberry', Midland basin, west Texas, *Unpublished report*, Humble Oil and Refining Company, 1951.

Sterling, J. L., Fracture generation and fluids in the Spraberry Formation, Midland basin, Texas, Masters - independent study, New Mexico Institute of Mining and Technology, 2000.

Twiss, R. J., and E. M. Moores, *Structural Geology*, W. H. Freeman and Company, New York, 1992.

Tyler, N., and J. Gholston, Heterogeneous deep-sea fan reservoirs, Shackelford and Preston waterflood units, Spraberry trend, west Texas, *Report of Investigation 117*, Bureau of Economic Geology, 1988.

Warn, G., and R. Sidwell, Petrology of the Spraberry sands of west Texas, *Journal of Sedimentology and Petrology*, *23*, 67–74, 1953.

Winfree, K., Post-Permian folding and fracturing of the Spraberry formation within the Midland basin region of west Texas, *West Texas Geological Society Bulletin*, *35*, 5–20, 1995.

Zoback, M. L., and M. Zoback, Tectonic stress field of the continental United States, *GSA Bulletin*, *Memoir 172*, 532–539, 1989.

CHAPTER 4

NUMERICAL MODELING OF COUPLED FLUID-SOLID MECHANICS: MODEL PROPERTIES AND LIMITATIONS[1]

4.1 Introduction

Continuum numerical methods for studying fluid-solid mechanics are well established and are the most common approach for investigating coupled poroelastic problems. Recently, however, discrete methods of fluid-solid mechanics have been applied to coupled problems in porous media. Since such discrete techniques are relatively new, model testing and comparison to continuum methods are desirable. This chapter presents basic testing of the coupled lattice-Boltzmann and Discrete Element Method (LBDEM) technique developed by *Cook* [2001] and *Cook et al.* [in press]. *Cook* [2001] previously used the LBDEM technique to model complex phenomena such as drafting-kissing-tumbling in multi-particle sedimentation simulations, but properties of the model had not been previously evaluated in porous media applications. For this effort, it was necessary to modify the formulation to include additional features (e.g., boundary conditions) important for porous media applications. An overview of the coupling technique and justification of its use is presented,

[1]Portions of this chapter have been published in the *Proceedings of 2003 Soil and Rock America*: Boutt, D.F. Cook, B.K. McPherson, B.J.O.L. and J.R. Williams, Application of a directly coupled numerical model of fluid-solid mechanics

in addition to the results testing of the model for porous media applications.

4.2 Modeling Approach

4.2.1 Discrete Element Method

This dissertation details an investigation of the hydromechanical behavior of porous media using aDEM [*Cundall*, 1971; *Cundall and Strack*, 1979]. DEM simulations have been shown to successfully approximate the behavior of non-cohesive, granular systems under low stress conditions [*Cundall et al.*, 1982], as well as lithified sedimentary rocks [*Bruno and Nelson*, 1991; *Potyondy et al.*, 1996; *Hazzard et al.*, 2000; *Boutt and McPherson*, 2002]. In the remaining three chapters of the dissertation an existing two-dimensional DEM application [*Rege*, 1996] is employed. DEM simulates mechanical behavior of porous media by idealizing the system as a collection of separate particles that interact at their contact points. The method itself consists of (1) identifying elements in contact and (2) resolving the contact physics. The calculations performed in the DEM alternate between the application of Newton's Second Law and a force-displacement law (simple contact models) at the contacts between particles. The force-displacement law relates components of force to corresponding components of relative displacements through a generalized contact constitutive model. The contact constitutive model applied here has two parts: a stiffness model and a slip model. The motion equations are then integrated explicitly with respect to time to obtain particle positions. Positions at each time step are then used in force-displacement calculations and the calculation cycle starts over again. It is important to note that constitutive behaviors modeled with a DEM, including stress and strain relations, are results rather

than assumptions.

4.2.2 Coupled Model Theory

Fluid coupling with DEM was developed by *Cook* [2001] and *Cook et al.* [in press] through explicit integration of an LB (lattice-Boltzmann) algorithm with the DEM framework described above. Cook's approach is reviewed here. The fluid-solid coupling scheme is depicted in Figure 4.1. The velocity of the fluid is set to maintain a no-slip boundary condition on the solid particle. As a result of this condition, a momentum imbalance between the fluid and solid particle arises. This imbalance is resolved through the addition of momentum from the fluid to the solid, resulting in a net force on the solid. These codes are weakly coupled [*Celia and Gray*, 1992] and all simulations in this paper use a 1:1 DEM to LB timestep unless otherwise noted. A detailed development and validation of the coupled method can be found in *Cook et al.* [2000], *Cook* [2001], and *Cook et al.* [in press].

In the LB approach, fluid is represented as packets of mass that move about a regular lattice, or grid, defined with appropriate boundary conditions. Collision and redistribution, or streaming, of fluid packets occur at lattice nodes according to relationships that conserve mass and momentum, and recover the Navier-Stokes equation to the second order in space and time. Most of the computational cost incurred at each timestep is associated with the collision phase, which is local in nature. The only data exchange between lattice nodes occurs during the streaming of the distributions. The model uses the linearized,

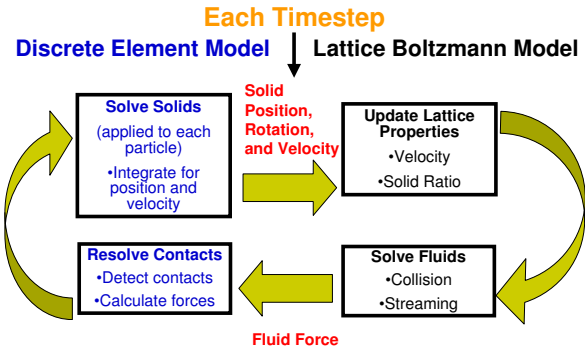

Figure 4.1: The coupling between lattice-Boltzmann and DEM is a function of both element location and velocity. Resulting forces from the fluid are applied to the solid and integrated for new position and velocity.

Bhatnagar-Gross-Krook (BGK) single-time relaxation form of the LB equation,

$$f_i(\mathbf{x} + \mathbf{e}_i \Delta t, t + \Delta t) = f_i(\mathbf{x}, t) - \frac{\Delta t}{\tau}(f_i(\mathbf{x}, t) - f_i^{eq}(\mathbf{x}, t)), \tag{4.1}$$

where $f_i(\mathbf{x}, t)$ is the fluid particle density distribution with velocity $\mathbf{e}_i$ at a node located at position x for a given time t; τ is the relaxation time; and $f_i^{eq}(\mathbf{x}, t)$ is the equilibrium density distribution for the fluid. Cook's (2001) two-dimensional model uses a square, nine-velocity lattice typically referred to as the D2Q9 model [*Qian et al.*, 1992]. Each node has eight density distributions, f_i, with non-zero velocities in addition to a zero-velocity or rest distribution at each node, f_0. The macroscopic fluid variables at a node, density ρ and velocity v, are associated with the moments of the fluid particle density distribution:

$$\mathbf{v} = \frac{\sum_i f_i \mathbf{e}_i}{\rho}, \rho = \sum_i f_i. \tag{4.2}$$

Lattice-Boltzmann simulates a slightly compressible fluid; consequently, fluid pressure, p, is given by the following equation of state

$$p = c_s^2 \rho, \tag{4.3}$$

where c_s is the fluid's speed of sound (defined as the ratio of the spatial discretization and the temporal discretization). This simple relationship for pressure gives LB a distinct advantage over traditional Navier-Stokes solvers, which must solve the Poisson equation for pressure. Coupling with discrete elements was accomplished through a moving solid boundary condition. At a minimum, a physically correct condition must impose identical velocities along fluid-solid interfaces. For computational expediency, Cook (2001) adopted an immersed moving boundary scheme proposed by *Noble and Torczynski* [1998]. The modified LB equation for solid-covered nodes becomes

$$f_i(\mathbf{x} + \mathbf{e}_i \Delta t, t + \Delta t) = f_i(\mathbf{x}, t) - \frac{\Delta t}{\tau}(1 - B)(f_i(\mathbf{x}, t) - f_i^{eq}(\mathbf{x}, t)) + B\Omega_i^S, \tag{4.4}$$

where B is a weighting function that depends on the local solid fraction or solid ratio, ε, defined here as the fraction of the nodal area covered by a solid(s), and the dimensionless relaxation time, τ^*, as

$$B(\varepsilon, \tau^*) = \frac{\varepsilon(\tau^* - 1/2)}{(1-\varepsilon) + (\tau^* - 1/2)}. \tag{4.5}$$

Ω^S is an additional collision term that bounces back the non-equilibrium part of the distribution and is given by

$$\Omega_i^S = f_{-i}(\mathbf{x}, t) - f_i(\mathbf{x}, t) + f_i^{eq}(\rho, \mathbf{v}_s) - f_{-i}^{eq}(\rho, \mathbf{v}), \tag{4.6}$$

where v_s is the solid's velocity at time t, and $-i$ is used to denote the distribution component having the opposite direction to i. The effect of LB Equation (4.4) is to modify the density distributions at those nodes covered by a

solid in such a way that the fluid velocity matches the solid's rigid body motion, enforcing a no-flow condition at the interface. An important advantage of this boundary condition is that it allows for sub-grid resolution of moving boundaries through the solid ratio term.

Fluid dynamics in a particle-fluid system are influenced by the presence of solids, and the displacements of solids (discrete elements) are, in turn, driven by fluid-induced forces. The moving boundary condition presented above accounts for the effect of moving solids on fluid flow; coupling is completed with the computation of the fluid-induced forces on solids. The force of the fluid, F_f, on a discrete element is calculated by summing up the momentum transfer that occurs over the n nodes covered by the element as

$$\mathbf{F}_f = \frac{h^2}{\Delta t} \sum_n B_n \sum_i \Omega_i^S \mathbf{e}_i, \tag{4.7}$$

where h is the nodal spacing. Fluid-induced torque, T_f, is found through a similar computation,

$$\mathbf{T}_f = \frac{h^2}{\Delta t} \sum_n [(\mathbf{x} - \mathbf{x}_s) \times (B_n \sum_i \Omega_i^S \mathbf{e}_i)], \tag{4.8}$$

where $\mathbf{x_s}$ is the centroid of the solid particle at time t. Fluid-particle coupling is realized at each timestep by first computing the fluid solution, and then updating solid particle positions by integration of the equations of motion.

It should be noted that in the LBDEM formulation it is assumed that a fluid force is only applied to the discrete elements if the fluid has a non-zero velocity. This implies that static pressure, on the whole, is not captured. Conceptually, issues with this assumption are avoided by treating changes in

pressure within the model to be dynamic pressure or changes from a static pressure condition. This is accomplished by setting initial and boundary conditions to effective stress conditions, which is simply done by taking the total stress and subtracting off the static pressure. This limitation results in the poroelastic condition of setting the Biot-Willis coefficient (discussed in Chapter 1) equal to 1.

4.3 Why Navier-Stokes and the LBDEM technique?

A brief review of previous numerical techniques used to model coupled fluid-solid mechanics in porous media was presented in Chapter 1. Justification for the fluid part of the LBDEM approach is developed here. In the LB method, the Navier-Stokes (N-S) equations of incompressible fluid flow are solved to a second order in space and time. From a computational standpoint, these calculations in porous media flow are much more expensive than a Darcy's law approach. The following question could then be asked: what is the advantage of the increase in computational expense? The answer depends on the nature of the problem and questions being answered by the simulation. For the problems of interest in this dissertation, solving the N-S equations is superior to a Darcy's implementation for the following reasons:

- It allows relaxation of continuum assumptions associated with Darcy's law [*Ferreol and Rothman*, 1995; *vanGenabeek and Rothman*, 1996; *O'Connor and Fredrich*, 1999].

- It accurately resolves pore-scale flow processes [*Ferreol and Rothman*, 1995; *vanGenabeek and Rothman*, 1996].

- It includes inertial physics of fluid [*Chen and Doolen*, 1998].
- It handles fluid properties (such as compressibility) without additional terms.

Relaxing inherent limiting assumptions in continuum formulations is one of the major advantages to modeling porous media with pore-scale solutions of fluid flow. The most basic assumption that can be discarded is that of the hydraulic conductivity parameter in Darcy's law. Since the N-S equations are explicitly solved in a known geometry of porous media, the hydraulic conductivity of the porous media is an outcome of the model, not a specified parameter. This is extremely important when permanent deformations in the material occur that cause porosity and corresponding permeability changes. No *a priori* assumptions about porosity and permeability relationships are needed with the LBDEM. By comparison implementations based on linear poroelasticity don't assume any change in permeability associated with changes in volumetric strain [*Wang*, 2000].

Not only does this formulation allow for flexibility in model parameterization, but representative elementary volume (REV) restrictions assumed in any application of Darcy's Law are also avoided. Previous research applications of coupled Darcy schemes with DEM [*Klosek*, 1997; *Sakaguchi and Muhlhaus*, 2000; *Bruno et al.*, 2001; *Flekkoy and Malthe-Sorenssen*, 2002] are vague with respect to whether REV conditions are met. It can be shown that Darcy's law does not capture grain-scale fluid-flow phenomena because of the assumed linear pressure drop. Typically, a finite element mesh is solved over a region comprising a few discrete elements. It is unclear in most of these studies

whether these elements were envisioned as grains or assemblages of grains. In general, modeling grain micromechanics with Darcy's Law often violates REV conditions and imposes over-restrictive constraints on permeability distributions.

4.4 Model Boundary Conditions

Boundary conditions implemented by *Cook* [2001] for the LBDEM model included periodic, no-flow, slip, and external forcing. The LBDEM was extended in this study to include a more realistic pressure boundary condition for the simulation of flow through porous media and representation of conditions typically applied in experimental tests.

4.4.1 Pressure Boundary Condition

Pressure conditions are imposed in many numerical and experimental setups to create fluid pressure drops through porous materials. For flow through porous media, these conditions are necessary to determine fluid permeabilities. To extend our model, we chose to incorporate the boundary condition of *Zou and He* [1997]. This was a good choice since it is general, local, and relatively efficient compared to the image-node pressure boundary conditions of *Chen et al.* [1996] and *Maier et al.* [1996]. When using pressure boundary conditions (constant density condition), special care must be taken to satisfy numerical constraints of the method while maintaining the desired numerical value of the pressure at the inlet and outlet. This complication occurs because of the equation of state for pressure, where pressure is a function of the density and also the ratio of node spacing to timestep. Results for density and velocity

errors for flow between parallel plates using the pressure boundary condition indicate that both the density (pressure) and velocity profiles slowly converge towards a steady-state distribution (Figure 4.2).

An additional test was designed to examine errors associated with fixing large density differences across the channel that cause large pressure gradients. Many problems of interest that involve fluids in geomechanics also involve large fluid pressure gradients. Understanding the upper limits of this method in terms of errors resulting from fluid pressure gradients is of utmost importance. A plot of relative velocity error vs. percent density change along the flow channel is depicted in Figure 4.3. The plot indicates that even with relatively large density drops, the maximum error is still relatively small. The error at small percent density drops is attributed to discretization error.

4.4.2 No Slip

The current version of the LBDEM code uses one of two boundary conditions to enforce a no-slip boundary condition. The immersed moving boundary, presented above, can be used for both moving and stationary solids. The more traditional no-slip boundary condition, also known as the bounce-back or natural condition, is a stationary boundary condition. Testing indicated that both conditions properly enforce a no-slip condition and provide numerically accurate results.

4.5 Model Properties

Solving the N-S equations accurately with LB requires that certain numerical parameters meet specified conditions. Numerous sources of error may

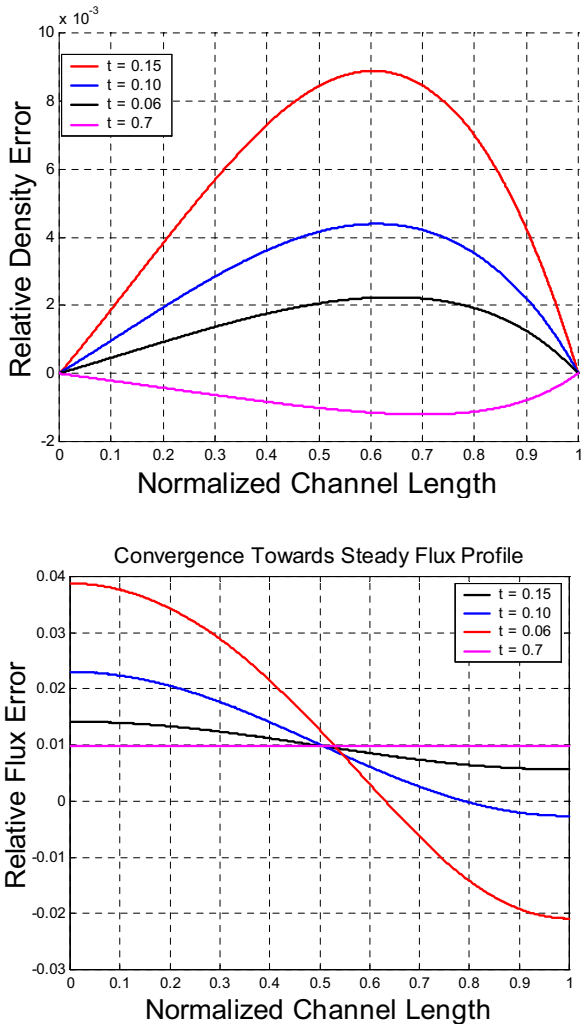

Figure 4.2: Convergence from an initial condition of rest towards steady state for velocity and pressure using pressure boundary condition of *Zou and He* [1997] compared to an analytical solution for steady-state Poiseuille flow. The top gives the density difference and the bottom plot shows the relative flux difference.

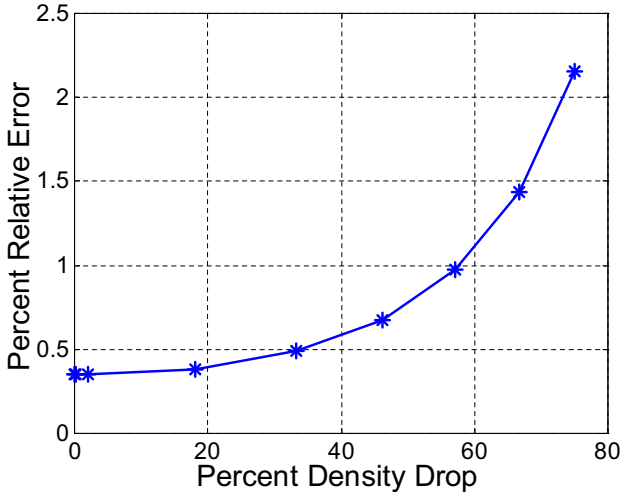

Figure 4.3: The mean velocity error associated with increasing density differences along channel is significantly higher. The points, connected by straight lines, represent the actual error between the simulation and the analytical solution for Poiseuille flow.

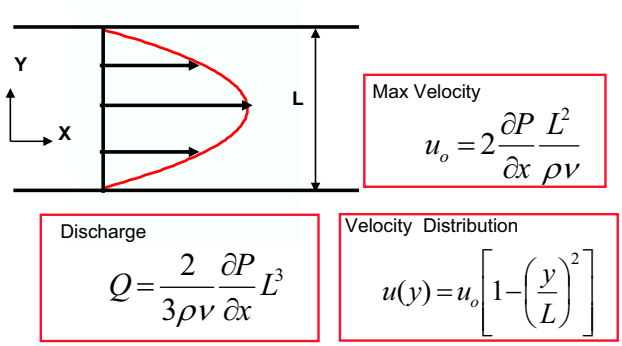

Figure 4.4: Problem space and analytical solution for Poiseuille flow. Comparisons of model results were made to this solution.

arise due to improper grid resolution, large fluid velocities relative to fluid speed of sound, and improper model parameterization leading to spurious solutions. Each one of these aspects is explored below in addition to an investigation of the LB formulation's compressibility properties.

4.5.1 Grid Resolution

One of the most important aspects of numerical modeling is the proper allocation of computer resources. The level of spatial and temporal resolution necessary to capture the essential physics of a problem dictates the computational requirements of a given simulation. The model's computational demand can be optimized through determination of the minimum level of discretization required to accurately simulate pore flow. To provide this guidance, an idealized study was devised to determine the amount of error, relative to the analytical solution for Poiseuille flow (Figure 4.4), associated with a particular discretization level. Poiseuille channel flow was simulated at varying discretiza-

tions with a set of models that had identical physical (domain) dimensions. A total of 11 models were created with the number of nodes across the channel ranging from 3 to 39 using the bounce-back condition for the no-slip boundary. Results from the study are shown in Figure 4.5 and Figure 4.6. In Figure 4.5, four different velocity profiles are shown and compared to Poiseuille flow. By increasing the number of nodes the simulation converges to the analytical solution. In theory, since LB is second order and the theoretical velocity profile parabolic, the model should reproduce exactly the analytical solution for Poiseuille flow (within round-off error) [*Chen and Doolen*, 1998]. However, first-order boundary conditions are used here, which degrade the accuracy of the solution across the fluid domain. A summary data plot is presented in Figure 4.6. This figure depicts percent error as a function of the number of nodes defining the channel. Error decreases as the number of nodes increases, revealing roughly first-order numerical convergence in the solution as a result of the lower-order boundary conditions. Overall, these results imply that four or five nodes between solid particles should be sufficient to achieve accurate simulations in large-scale applications.

4.5.2 Relaxation Time

The relaxation parameter in LB is typically constrained to have a numerical value between 0.5 and 1 to ensure numerical stability and accuracy. This parameter relates the simulated fluid viscosity to the spatial and temporal discretization. In nondimensional form, the relaxation parameter is given by

$$\frac{1}{2} + \frac{3\nu\Delta t}{h^2} = \tau. \tag{4.9}$$

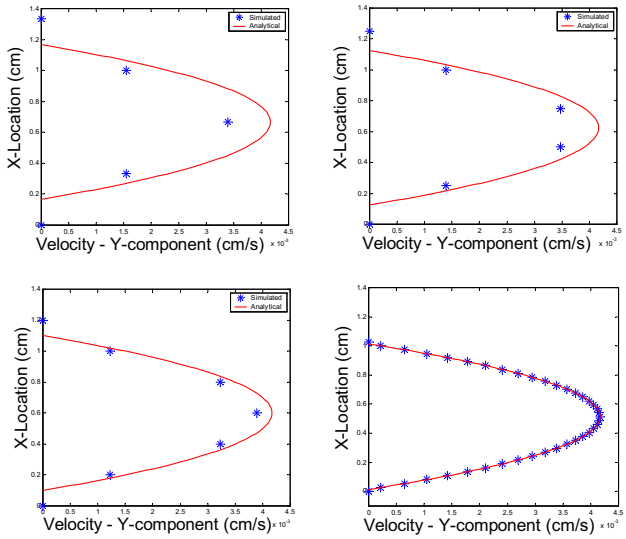

Figure 4.5: Comparisons of LB solutions (stars) to analytical solutions (lines) for 3, 4, 5, and 37 nodes in the channel. These errors allow the determination of the required number of nodes for numerically accurate resolution of flow.

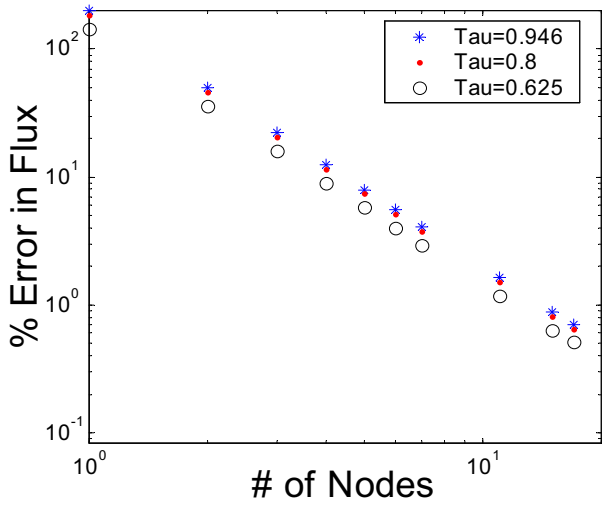

Figure 4.6: A log-log plot of error vs. number of nodes shows roughly first order numerical convergence. The influence of relaxation time, τ^*, on relative flux error is relatively small, but observable.

Figure 4.6 shows the influence of the dimensionless relaxation time on the numerical accuracy of LB for Poiseuille flow between parallel plates. As shown, a smaller relaxation time gives a more accurate result. However, this is not always the case, as other studies have shown that relaxation times smaller than 0.625 resulted in more error [*Cook*, 2001].

4.5.3 Computational Mach Number

In the LB scheme, error increases with computational Mach number squared [*Reider and Sterling*, 1995]. Thus, this parameter must be kept fairly small (Figure 4.7). For the special case of Poiseuille flow in a channel, we can exploit the analytical solution to explore the constraints that the small Mach number requirement places on LB simulations. In the LB scheme, the

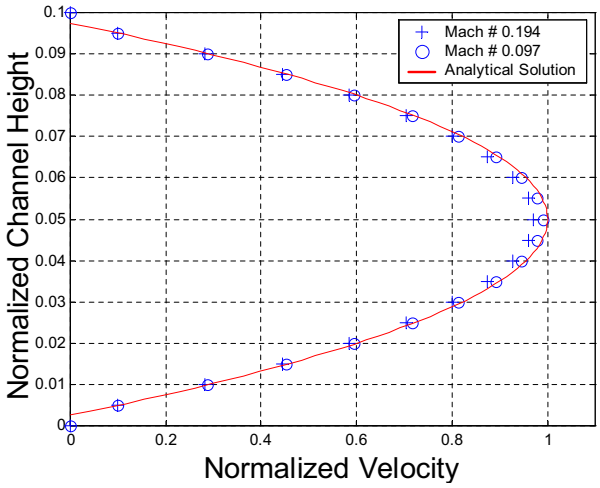

Figure 4.7: The relative flux error for Poiseuille flow increases as the Mach number squared. It is important that this number be small (i.e. much less than 1.0). A computational Mach number greater than one implies that fluid velocity is traveling faster than the method can transfer information causing instability.

computational Mach number is defined as

$$M = \frac{v_{\max}}{c}, \tag{4.10}$$

where $v_{\max}$ is the maximum fluid speed, c is the lattice speed given by

$$\frac{h}{\Delta t}, \tag{4.11}$$

and h is equal to the spacing between lattice nodes. For Poiseuille flow, $v_{\max}$ is equal to

$$v_{\max} = \frac{\Delta P}{\Delta L}\frac{H}{2\nu\rho}, \tag{4.12}$$

where ΔP is the change in fluid pressure across the distance ΔL, H is the channel height, and ν is the fluid viscosity. As stated above the fluid pressure in LB is related to the fluid density by the equation of state in Equation (4.3). Substituting this relation into Equation (4.12) we obtain

$$v_{\max} = \frac{3}{14}\frac{h^2}{\Delta t^2}\frac{\Delta\rho}{\Delta L}\frac{H}{\nu\rho}. \tag{4.13}$$

We can substitute Equation (4.13) into the definition of the computational Mach number (M) and make use of the lattice speed definition to yield

$$M = \frac{3}{14}\frac{h}{\Delta t}\frac{\Delta\rho}{\Delta L}\frac{H}{\nu\rho}. \tag{4.14}$$

Equation (4.9) demonstrates that the fluid viscosity is a function of timestep, node spacing, and relaxation time. This relationship, written in terms of the timestep, is equal to

$$\Delta t = \frac{(2\tau - 1)h^2}{6\nu}, \tag{4.15}$$

where τ is the relaxation time, a numerical stability parameter. Substituting the expression in Equation (4.13) we find

$$M = \frac{9}{7}\frac{\Delta\rho}{\Delta L}\frac{H}{h(2\tau - 1)\rho}. \tag{4.16}$$

Typically, the grid resolution, relaxation parameter, and density variations are constrained, which leaves ΔL, the total length of the domain (parallel to flow) as the only free parameter.

4.5.4 Fluid Compressibility

As shown earlier, error in the LB method increases with density gradients. Although the LB method solves the Navier-Stokes equations for incompressible fluid flow the numerical fluid density can vary. As long as density gradients are kept relatively small; the errors in LB are sufficiently small. Thus, the method can accommodate a weakly compressible fluid, such as water or brine, which are the fluids of interest in most hydrogeologic problems. Fluid compressibility is an important property of a hydrogeologic system, since some storage is from this property. Also, fluid compressibility plays a role in poroelastic response, since the fluid itself can support a certain amount of stress. The following test problem is designed to explore the compressibility properties of the LB fluid.

The important parameters in determining the compressibility of a fluid are (1) density change ($\Delta\rho$) and (2) an applied stress (σ_o). For a Newtonian fluid one can write the compressibility of a fluid β as

$$\beta = \frac{1}{\rho_o}\frac{\Delta\rho}{\sigma_o}, \tag{4.17}$$

where ρ_o is the initial fluid density. This implies that a positive change in density of the fluid with a positive applied stress is linear. The inverse of the fluid compressibility (β) is the fluid modulus of elasticity (E). These equations could also be written in terms of volume, where volume would replace density and a negative sign would be placed in front to signify a reduction in volume with an increase in σ_o.

In Figure 4.8, a very simple model is used to test the LBDEM fluid compressibility properties. The initial conditions are equilibrium pressure with the platens applying the stress at rest. All model properties are listed in Table 4.1. The test begins with an application of stress on all four sides of a unit volume of fluid. The boundary conditions for the solid elements are "servo" controlled such that they apply a constant stress. A plot of applied stress vs. time for the above conditions is shown in Figure 4.9. Since we are simulating a dynamic system, the stress applied at the boundary takes some finite time to reach its ultimate value. This takes roughly 0.03 seconds of model time to reach the specified stress. Plots of fluid density change and fluid velocity vs. time are given in Figure 4.10. As the applied stress increases, the resulting density change is roughly linear and reaches a mean value of $1.9 * 10^{-4}$. The movement of the boundary elements also forces fluid movement (flow) to occur until a quasi-steady state is reached. Given a density change of $1.9 * 10^{-4}$ and the initial properties of the system (Table 4.1), the compressibility of the fluid in this model is $1.9 * 10^{-6} Pa^{-1}$.

In LB information travels at a finite speed. The fluid speed of sound

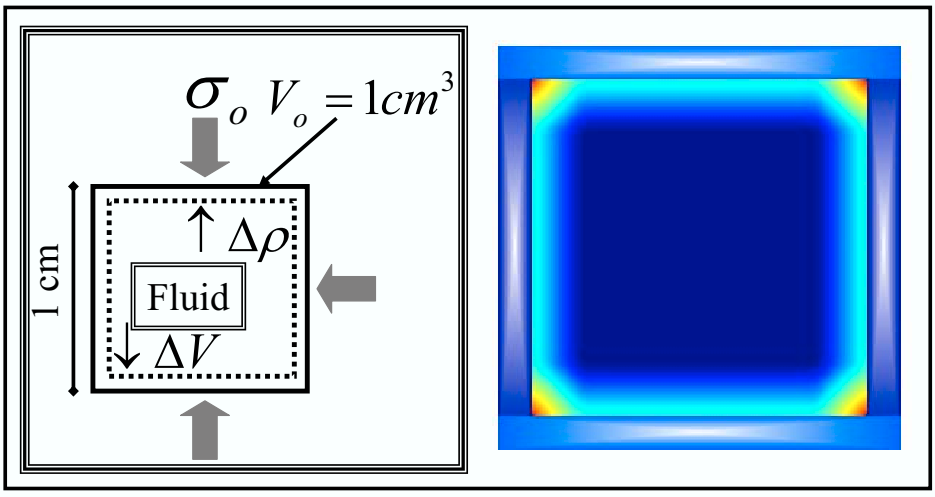

Figure 4.8: Conceptual model (left) and screenshot (right) of fluid compressibility problem. The screenshot depicts the platens and a filled contour plot of fluid pressure at early time.

Table 4.1: Parameters of fluid compressibility simulations

Parameter	Value
Viscosity ($\frac{cm^2}{s}$)	0.1
Relaxation Time (-)	0.875
Node Spacing (cm)	0.011
Timestep (s)	$1.5e-4$
Number of Nodes (-)	10201
Fluid Speed of Sound ($\frac{cm}{s}$)	142.8
Applied Stress (Pa)	100

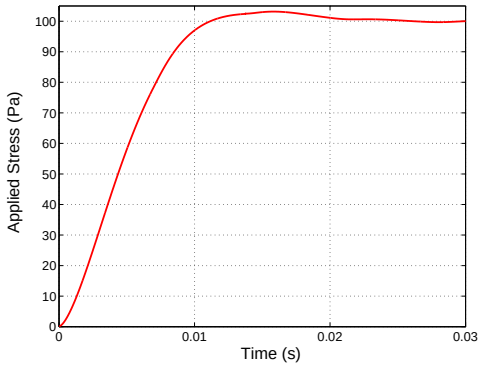

Figure 4.9: In LBDEM, a constant stress boundary condition is used to determine parameters defining the fluid compressibility. As a result of an applied stress, a volume of fluid will come to equilibrium as the fluid resists a change in volume. The corresponding density change yields information about how the fluid responds to changes in pressure.

of the lattice (c_s) is related to the fluid compressibility (β) by

$$c_s = \sqrt{\frac{1}{\beta\rho}}, \tag{4.18}$$

and solving for β provides

$$\beta = \frac{1}{c_s^2\rho}. \tag{4.19}$$

The compressibility of the fluid via the model parameters is $4.9 * 10^{-5} Pa^{-1}$. This value is slightly larger than the value calculated via the model test, but nevertheless is within an order of magnitude of each other. Given this relation between fluid compressibility and the fluid speed of sound, it enables us to evaluate potential problems, such as in applying the LBDEM. Further comparison of the LBDEM to a problem with significant fluid compressibility is presented in Chapter 5.

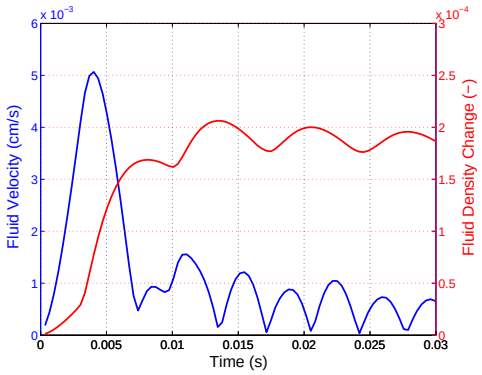

Figure 4.10: When a stress is applied to a volume of compressible fluid, a corresponding density change takes place. In the LBDEM, the velocity of the fluid accelerates until an equilibrium condition is reached. At late times the fluid density curve is the upper curve and the fluid velocity curve is the lower.

References

Boutt, D. F., and B. J. McPherson, Simulation of sedimentary rock deformation: Lab-scale model calibration and parameterization, *Geophysical Research Letters*, *29*, 10.1029/2001GL013,987, 2002.

Bruno, M., and R. Nelson, Microstructural analysis of the inelastic behavior of sedimentary rock, *Mechanics of Materials*, *12*, 95–118, 1991.

Bruno, M., A. Dorfmann, K. Lao, and C. Honeger, Coupled particle and fluid flow modeling of fracture and slurry injection in weakly consolidated granular media, in *Rock Mechanics in the National Interest*, edited by Elsworth, Tinucci, and Heasley, Swets and Zeitlinger Lisse, Washington, D.C., 2001.

Celia, M., and W. Gray, *Numerical Methods for Differential Equations*, Pentice Hall, New York, 1992.

Chen, S., and G. Doolen, Lattice boltzman method for fluid-flows, *Annual Review of Fluid Mechanics*, *20*, 329–364, 1998.

Chen, S., D. Martinez, and R. Mei, On boundary conditions in lattice Boltzmann methods, *Phys. Fluids A*, *8*, 2527–2536, 1996.

Cook, B., D. Noble, D. Preece, and J. Williams, Direct simulation of particle laden fluids, in *Fourth North American Rock Mechanics Symposium.*, A.A. Balkema, Rotterdam, 2000.

Cook, B., D. Noble, D. Preece, and J. Williams, Direct simulation of particle laden fluids, *Journal of Engineering Computations*, in press.

Cook, B. K., A numerical framework for the direct simulation of solid-fluid systems, Doctoral dissertation, Massachusetts Institute of Technology, 2001.

Cundall, P., A computer model for simulating progressive, large-scale movement in block rock systems, in *Rock fracture*, edited by Anonymous, vol. 1, Int. Soc. Rock Mech., France, 1971.

Cundall, P., and O. Strack, A discrete element model for granular assemblies, *Geotechnique*, *29*, 47–65, 1979.

Cundall, P., A. Drescher, and O. Strack, Numercal experiments on granular assemblies: Measurements and observations, in *Deformation and Failure of Granular Materials*, edited by J. Jenkins and H. Luger, A.A. Balkema, Brookfield, VT, 1982.

Ferreol, B., and D. Rothman, Lattice-Boltzmann simulations of flow through Fontainebleau sandstone, *TRANSPORT IN POROUS MEDIA*, *20*, 3–20, 1995.

Flekkoy, E. G., and A. Malthe-Sorenssen, Modeling hydrofracture, *Journal of Geophysical Research*, *107*, 2151–2151, 2002.

Hazzard, J., P. F. Young, and S. Maxwell, Micromechanical modeling of cracking and failure in brittle rocks, *Journal of Geophysics Research*, *105*, 16,683–16,697, 2000.

Klosek, J., The integration of fluid dynamics with a discrete-element modelling system : Algorithms, implementation, and applications, Masters thesis, Massachusetts Institute of Technology IT, 1997.

Maier, R., R. Bernard, and D. Grunau, Boundary conditions for the lattice Boltzmann method, *Phys. Fluids A*, *8*, 1788–1801, 1996.

Noble, D., and J. Torczynski, A lattice boltzman method for partially saturated computational cells, *International Journal of Modern Physics*, *C9*, 1189–201, 1998.

O'Connor, R., and J. Fredrich, Microscale flow modeling in geologic materials, *Physics and Chemistry of the Earth (A)*, *24*, 611–616, 1999.

Potyondy, D., P. Cundall, and C. Lee, Modeling rock using bonded assemblies of circular particles, in *Rock Mechanics: Tools and Techniques*, edited by Aubertin, Hassani, and Mitri, pp. 1937–1944, A.A. Balkema, Rotterdam, 1996.

Qian, Y., D. Dhumieres, and P. Lallemand, Lattice BGK models for Navier-Stokes equation., *Europhysics Letters*, *17*, 479–484, 1992.

Rege, N., Computational modeling of granular materials, Doctoral dissertation, Massachusetts Institute of Technology, 1996.

Reider, M., and J. Sterling, Accuracy of discrete-velocity BGK models for the simulation of the incompressible Navier-Stokes equations, *Computers and Fluids*, *24*, 459–467, 1995.

Sakaguchi, H., and H.-B. Muhlhaus, Hydrid modeling of coupled pore fluid-solid deformation problems, *Pure and Applied Geophysics*, *157*, 1889–1904, 2000.

vanGenabeek, O., and D. Rothman, Macroscopic manifestations of microscopic flows through porous media: Phenomenology from simulation, *ANNUAL REVIEW OF EARTH AND PLANETARY SCIENCES*, *24*, 63–87, 1996.

Wang, H., *Theory of Linear Poroelasticity: with Applications to Geomechanics and Hydrogeology*, Princeton University Press, Princeton, New Jersey, 2000.

Zou, Q., and X. He, On pressure and velocity boundary conditions for the lattice-Boltzmann method, *Physics of Fluids (A)*, *9*, 1591–1598, 1997.

CHAPTER 5

NUMERICAL INVESTIGATION OF THE MICROMECHANICS OF FLUID SATURATED ROCKS[1]

Abstract

A detailed understanding of the coupling between fluid and solid mechanics is important for understanding many processes in the Earth sciences. Numerical models are a popular means for exploring these processes, but most models do not adequately handle all aspects of this coupling. This paper presents an application of a robust fluid-solid coupling scheme, LBDEM, for porous media simulation. The LBDEM approach couples a discrete element method (DEM) for solid mechanics and a lattice-Boltzmann (LB) method for fluid mechanics. To illustrate its application to porous media, fluid flow through periodic arrays of cylinders at various Reynolds numbers are examined and compared to previously published experimental and numerical results. For a range of solid concentrations, fluid flow simulation results are very consistent with the results of previous studies, suggesting that fluid mechanics are being effectively resolved. We also compared model results to basic Darcy's law calculations for flow through stationary porous media, also to porosity-permeability rela-

[1]This chapter has been submitted to the *Journal of Geophysical Research*: Boutt, D.F. Cook, B.K. McPherson, B.J.O.L. and J.R. Williams, Direct simulation of fluid-solid mechanics in porous media using the lattice-Boltzmann and discrete element methods

tionships predicted by the Kozeny-Carmen equation. Quantitative comparison to a one-dimensional analytical solution for fluid flow in a slightly deformable medium suggests a reasonable fluid diffusion-like profile. Finally, full coupling of the numerical formulation is demonstrated through simulation of porous medium consolidation. Results of these simulations are consistent with those predicted by poro-elastic theory. In sum, the LBDEM model captures the full dynamics of fluid-solid micro-mechanics, and facilitates detailed and effective investigations not possible before.

5.1 Introduction

Fundamental problems in geology and geological engineering commonly involve analysis of coupled processes in heterogeneous systems, such as thermomechanical, hydromechanical, and chemomechanical processes. Analysis and interpretation of coupled problems typically rely on more sophisticated conceptual models and have more degrees of freedom than uncoupled problems [*Yow and Hunt*, 2002]. We are trying to understand the dynamics of coupled fluid-solid processes in hydrogeology and geomechanics. One example is the generation of deep subsurface rock fractures by anomalous fluid pressures. In sedimentary basins, fluid pressures may be elevated by many different processes [*Neuzil*, 1995] and attain large magnitudes relative to hydrostatic, sometimes exceeding the least principal stress [*McPherson and Bredehoeft*, 2001]. The rate of pressure dissipation is governed by rock hydraulic diffusivity and the rate of pressure generation. Macroscopic (i.e. continuum) descriptions of these processes typically yield first-order controls on system behavior but do not address smaller-scale processes responsible for observed inelastic rock deformation. Of

particular importance are the initiation and propagation of extension fractures and associated feedbacks between the fluid flow field and the mechanical state of the rock. A detailed understanding of the coupled pore-scale physics will facilitate better designs and fewer limitations of experimental tests, and more effective interpretation of field data.

Recent discussion in the literature has focused on evidence for a strong hydrologic control on the state of stress in the Earth's crust [*Simpson*, 2001; *Moore and Iverson*, 2002; *Saffer and Bekins*, 2002]. For example, deciphering the role of fluid pressure and fluid flow on crustal mechanics is of critical importance to understanding what causes earthquakes. It is difficult to isolate, from experiments and field data alone, the competing effects of fluids on the stress field and the stress field on the fluids.

Problems involving coupled processes are typically addressed with continuum models that rely on constitutive relations developed through experimental work [*Neuzil*, 2003]. Yet, continuum models typically yield little information concerning material mechanical behavior. Another approach is to use a discrete mechanical approach that controls and tracks many parameters, including pore structure, such as the discrete element method (DEM). An advantage of using DEM models for solid mechanics is that the underlying physics are clearly resolved and the models are inherently discontinuous and heterogeneous. In this paper we apply a coupled model [*Cook et al.*, 2000; *Cook*, 2001; *Cook et al.*, in press] that uses DEM for resolving solid mechanics and the lattice-Boltzmann method (LB) to simulate fluid mechanics. LB is an efficient method for solving the Navier-Stokes equations of incompressible fluid

flow. The solid and fluid mechanics are directly resolved by simulating flow at the pore-scale and computing fluid-grain coupling. Implicit assumptions about effective stress and heuristic porosity-permeability relationships are not necessary. Since the solid framework is made of discrete elements, their deformation and movement will directly change porosity and hence permeability of the system. Constitutive relations between porosity and permeability are therefore results rather than assumptions.

With this numerical model we simulated steady and unsteady fluid flow through stationary and non-stationary discrete media. Pore-scale fluid flow through simple square periodic arrays of cylinders at various Reynolds numbers was compared to previously published experimental and numerical results. Additional comparisons of model results to those predicted by Darcy's law for flow through stationary porous media were carried out. These include comparison of resulting model permeability to porosity-permeability relationships predicted by the Kozeny-Carmen equation. A quantitative comparison to a 1-D analytical solution fluid flow in a slightly deformable medium was also made. Finally, simulations of porous medium consolidation were compared to results predicted by poroelasticity theory. Thus, it is our goal to demonstrate the validity of the new LBDEM coupled model to applications for flow through both stationary and non-stationary porous media.

5.2 Fluid-solid Coupling in Porous Media

Coupling between fluids and solids in a porous medium results from direct interaction in pores. For instance, as the volume of a pore space collapses, fluid is forced to either compress or flow out of its pore. Conversely, a fluid

pressure change may impart a tangible force on the solid grain "walls" of the pore. This microscale interaction is the most fundamental feedback loop or coupling. On a macroscopic scale, coupling between fluids and solids result from changes in pore-space (mechanical to fluid) and/or changes in effective stress (fluid to mechanical) [Figure 1 of *Yow and Hunt*, 2002].

Many different frameworks are used to model the coupled physics of fluid-solid systems (Table 5.1). These range from complete continuum approximations [*Wang*, 2000] to purely discontinuous approximations [This paper; [*Bruno and Nelson*, 1991]]. Most frameworks employ some empirical constitutive relations governing fluid flow (e.g., Darcy's law) and fluid coupling (e.g., effective stress). The most common example is the assumption of Darcy flow. Several micro-mechanical models were recently developed using discrete elements coupled to a continuum fluid flow scheme based on Darcy's law with good results [*Klosek*, 1997; *Sakaguchi and Muhlhaus*, 2000; *Bruno et al.*, 2001; *Flekkoy and Malthe-Sorenssen*, 2002]. Several authors justify this type of approach by suggesting that individual discrete elements are not single grains but rather are groups of grains. As a consequence, these models must use empirical relations, such as the Kozeny-Carmen equation, to relate porosity to permeability.

Fluid-solid coupling in models coupled with Darcy's law is achieved through the summation of fluid forces imparted on the solid (i.e. effective stress), summed either at the solid centroid or around the solid perimeter. Movements of the solids inhibit or promote fluid flow (i.e. through porosity/permeability changes). In the case of the Darcy formulation mentioned

Table 5.1: Summary of previously used coupling techniques

	Modeling Technique		**Coupling Technique**	
References	**Solid**	**Fluid**	**Solid → Fluid**	**Fluid →Solid**
Numerous Papers [See *Wang*, 2000; *Stephansson*, 2003, for review]	Poro-elasticity	Darcy's	Pore Volume Changes	Effective Stress
Klosek [1997]; *Sakaguchi and Muhlhaus* [2000]; *Bruno et al.* [2001]; *Flekkoy and Malthe-Sorenssen* [2002]	DEM	Darcy's	Porosity-Permeability changes	Effective Stress
Bruno [1994]; *Li and Holt* [2001]	DEM	Poseuille	Porosity-Permeability	Effective Stress
This paper	DEM	LB	Impedes Flow	Momentum Transfer

above, coupling is achieved through modification of the hydraulic conductivity term in Darcy's law. For example, in the case of a flow network model [*Bruno*, 1994; *Li and Holt*, 2001], where fluid flow is routed through cylindrical pipes (Poiseuille flow), the pipe walls act as a proxy for pore throats. These pipes are assigned a nominal diameter, and as solids move away from one another, this diameter is proportionally increased. Thus, in both of these formulations, coupling is indirect because the conductance terms (pipe diameter or permeability) are adjustable parameters based on empirical or proxy processes.

We take a different approach to this problem by applying a direct simulation approach developed by *Cook* [2001] and *Cook et al.* [in press]. No empirical relations are necessary to relate fluid flux to pressure drop at the pore scale. Also, since the model directly simulates movement and deformation of the solid matrix, no *a priori* assumptions about the relationship between fluid permeability and porosity are necessary. The hydrodynamics simply evolve with the changing solid matrix.

5.3 Modeling Approach

5.3.1 Discrete Element Method

This paper details an investigation of the hydromechanical behavior of porous media using DEM [*Cundall*, 1971; *Cundall and Strack*, 1979]. The technique has successfully approximated the behavior of non-cohesive, granular systems under low stress conditions [*Cundall et al.*, 1982], including lithified sedimentary rocks [*Bruno and Nelson*, 1991; *Potyondy et al.*, 1996; *Hazzard et al.*, 2000; *Boutt and McPherson*, 2002]. In this paper, we employ an existing two-dimensional DEM application [*Rege*, 1996]. DEM simulates mechanical

behavior of porous media by idealizing the system as a collection of separate particles that interact at their contact points. The method itself consists of (1) identifying elements in contact and (2) resolving the contact physics. The calculations performed in the DEM alternate between the application of Newton's Second Law and a force-displacement law (simple contact models) at the contacts between particles. The force-displacement law relates components of force to corresponding components of relative displacements through a generalized contact constitutive model. The contact constitutive model applied here is one with two parts, including a stiffness model and a slip model. The motion equations are then integrated explicitly with respect to time to obtain particle positions. Positions at each time step are then used in force-displacement calculations and the calculation cycle starts over again. It is important to note that DEM constitutive behaviors, including stress and strain relations, are results rather than assumptions.

5.3.2 Coupled Model Theory

Fluid coupling with DEM was developed by *Cook* [2001] and *Cook et al.* [in press] through explicit integration of an LB algorithm with the DEM framework described above. Cook's approach is reviewed in the appendix of this chapter. The coupling scheme is depicted in Figure 5.1. The velocity of the fluid is set to maintain the no-slip boundary condition on the solid particle. As a result of this condition, a momentum imbalance between the fluid and solid particle arises. This imbalance is resolved through the addition of momentum from the fluid to the solid, resulting in a net force on the solid. These codes are currently weakly coupled and all simulations in this paper use a 1:1 DEM to LB

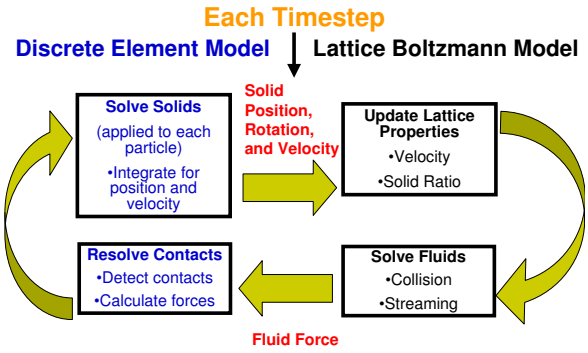

Figure 5.1: The coupling between lattice-Boltzmann and DEM is a function of both element location, velocity, and rotation. Resulting forces from the fluid are applied to the solid and integrated for new position and velocity.

timestep unless otherwise noted. A detailed development and validation of the coupled method can be found in *Cook* [2001]. The two-dimensional simulations reported by *Cook* [2001] include such complex phenomena as drafting-kissing-tumbling in multi-particle sedimentation simulations and the saltation phase of bed erosion.

5.3.3 LB Boundary Conditions

A variety of options are available for simulating boundaries in LB methods. The model by *Cook* [2001] described above includes no flow, slip, and periodic boundary conditions. In this paper we employ the periodic condition in the *Cook* [2001] model and implement *Zou and He* [1997]'s pressure boundary condition. A periodic boundary condition implies that fluid exiting a boundary is inserted in the opposite boundary yielding an infinite array of the domain that

is simulated. This condition was only used for simulations where comparisons were made with other periodic results. The pressure boundary condition was used for all the other simulations reported in this paper.

5.3.4 Model Two-Dimensionality

The most limiting aspect of this modeling scheme is the assumption of a two-dimensional system. However, many fundamental problems can still be addressed. In a compacted or very densely packed two-dimensional assembly of discrete elements, a physically unrealistic situation arises in the form of no connected paths for fluid to flow through. To facilitate the use of fluid coupling in this context, an assumption about the fluid flow paths must be made. This problem has been addressed before for the case of flow network models [*Bruno and Nelson*, 1991; *Bruno*, 1994; *Li and Holt*, 2001] and continuum Darcy's models [*O'Connor et al.*, 1997]. In both cases, fluid is assumed to flow out of plane and around solids. In our case we take a similar approach to *O'Connor et al.* [1997] and assume that fluid is flowing out the plane. The LB is assumed to only interact with a defined percentage of the discrete elements. For all simulations reported in this chapter the percentage was constant. This effectively results in a smaller radius used to resolve the fluid through the assembly. Changing the "effective" fluid radius results in changes in pore throat sizes and resulting macroscopic parameters, such as permeability.

5.4 Fluid Flow Through Periodic Arrays of Cylinders

The first series of fluid-flow simulations were conducted with solids fixed in space. One motivation for the study of fluid flow around stationary

objects is the design of heat and mass transfer equipment. A fundamental paper published on flow past spatially periodic arrays of cylinders was authored by *Sagani and Acrivos* [1982]. They approximated the creeping flow equations using multipole expansions and calculated the drag on square and hexagonal arrays of cylinders. Their solutions are shown to be in excellent agreement with the corresponding analytical expressions for flow around stationary cylinders. Subsequent to their work, *Edwards et al.* [1990] used finite elements to assess the influence of Reynolds number on the apparent permeability of periodic arrays of cylinders. *Edwards et al.* [1990] results were consistent with those of *Sagani and Acrivos* [1982] . *Koch and Ladd* [1997] also examined flow through spatially periodic and random arrays of cylinders, but used a lattice-Boltzmann scheme with solid boundaries modeled with a bounce-back scheme (see appendix). Following *Koch and Ladd* [1997] and *Hill et al.* [2001], we will employ a similar approach, but using the coupled LB-DEM model with an immersed boundary condition for solids (see appendix). In general experimental data for flows over stationary cylinders at low Reynolds number are very limited.

5.4.1 Low Reynolds Number Flows

Comparisons of previous numerical methods to the coupled LB-DEM model have been performed for the case of fluid flow around a stationary simple square array of cylinders at low Reynolds numbers, with Reynolds number defined by

$$Re = \frac{UD}{\mu}, \tag{5.1}$$

where U is the mean fluid velocity, D is the cylinder diameter, and μ is the dynamic fluid viscosity. Figure 5.2 illustrates the modeled domain and flow

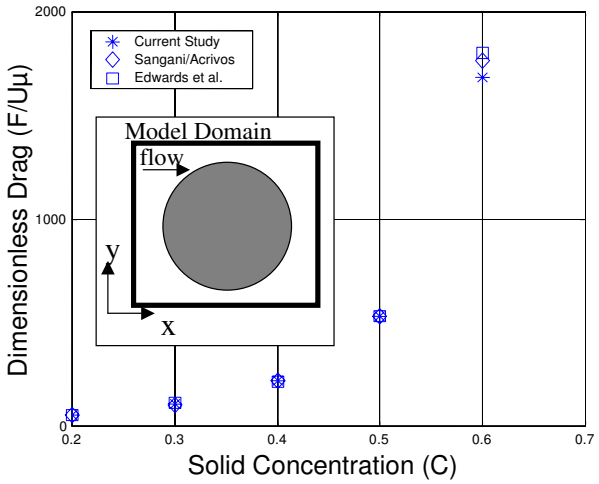

Figure 5.2: Dimensionless drag vs. solid concentration for low Reynolds flow around a periodic array of cylinders for solid concentrations ranging from 0.2 to 0.6. As solid concentration increases so does the drag on the cylinder.

direction. Boundary conditions on all sides of the model are periodic with an immersed boundary condition for the solid (see appendix). As *Koch and Ladd* [1997] point out, some error may be attributed to discretization of the solid onto the fluid lattice. The use of the immersed boundary condition helps reduce this error, but a small amount of irregularities still exist in the solid discretization. This may introduce a small amount of additional error compared to methods that can handle smoothed boundaries, such as the finite element method. The solid concentration C is defined as the area of the solid divided by the area of the unit cell of the periodic array and it was varied between runs.

Dimensionless drag force is defined as

$$\bar{F} = \frac{F}{U\mu}, \tag{5.2}$$

where F is the force per unit length of the cylinder. The force per unit length

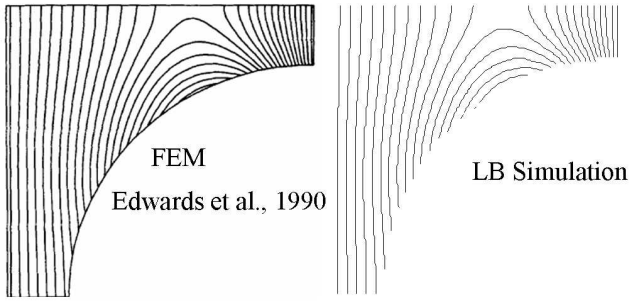

Figure 5.3: Qualitative comparison of pressure contours at a solid concentration of 0.5 for FEM results of *Edwards et al.* [1990] and our LBDEM results. A good match between the two solutions is achieved.

of the cylinder was calculated using a force balance at steady state through the relation

$$F = \frac{\Delta P}{\Delta l}\frac{\pi r^2}{C}, \tag{5.3}$$

where $\Delta P/\Delta l$ is the pressure gradient, r is the radius of the cylinder, and C is the solid concentration. A larger cylinder area should result in a larger overall fluid drag by the cylinder. In Figure 5.2 simulations with solid concentrations ranging from 0.2 to 0.6 are compared to the results of *Sagani and Acrivos* [1982],*Edwards et al.* [1990]. Pressure contours of flow around a cylinder at a solid concentration of 0.5 are plotted in Figure 5.3, where l is the length of the periodic domain. Note the good qualitative match between the finite element solution of *Edwards et al.* [1990] and the LBDEM simulation.

5.4.2 High Reynolds Number Flows

Higher Reynolds number flows are sometimes encountered in porous media, such as fluid flow near well bores. Some experimental data at higher Reynolds flows are available [*Bergelin et al.*, 1950], and serve as a good bench-

mark for the LBDEM coupled model. The modeled domain for this set of simulations is identical to that for the low Reynolds number flows. In this case, our results are compared with the experimental data of *Bergelin et al.* [1950] and the numerical results of *Edwards et al.* [1990]. *Bergelin et al.* [1950] measured pressure drop through a simple square arrangement of cylindrical tubes. We compare our results for dimensionless pressure drop, which is defined by

$$\nabla \bar{P} = \frac{\Delta P}{\Delta l} \frac{l}{\rho U^2}, \tag{5.4}$$

for Reynolds numbers ranging from 0.001 to 180, in Figure 5.4. As Reynolds increases, viscous energy dissipation becomes less important and thus the dimensionless pressure drop over the cylinders is reduced. All three results plotted on Figure 5.4 show this trend quite well, and the match between all three sets of data is reasonable. Deviations from the experimental data are probably a result of boundary conditions associated with the periodic condition used in the numerical solutions.

Sources of error in the LB solutions were evaluated by *Boutt et al.* [2003] and found to be small for the problems of interest. In these simulations errors arise from two sources. First, a smooth disc is represented with stair-stepped features due to the level of spatial discretization in the numerical method. These small irregularities can result in the propagation of errors not seen in analytical solutions and experimental data. Additionally error may arise from the simplification of using periodic boundary conditions to model a finite domain. As seen in Figure 5.4, this same source of error may be influencing the finite element solution of *Edwards et al.* [1990].

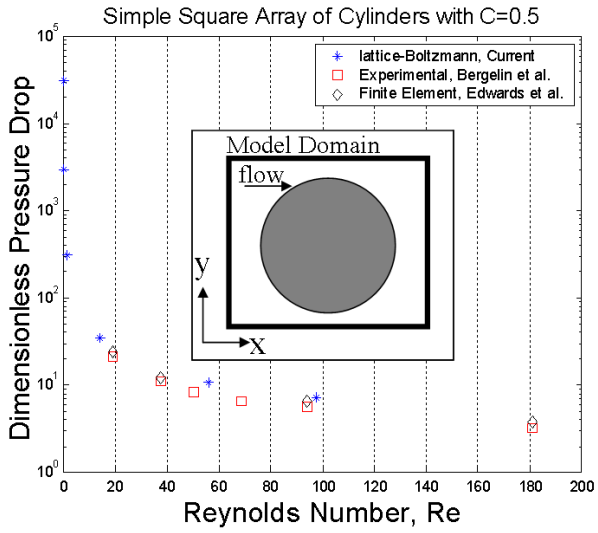

Figure 5.4: Dimensionless pressure drop vs. Reynolds number for flow around a periodic array of cylinders for a solid concentrations of 0.5. As the Reynolds number increases, the pressure drop decreases, as viscous dissipation is lessened.

5.5 Steady Flow Through Stationary Porous Media

Understanding steady flow through porous media is important for many scientists and engineers. Although Darcy's law is accepted as valid for low Reynolds number flow in porous media; the relatationship between permeability and some measurable property of the porous matrix is open to debate. One of the most widely accepted permeability relationships for porous media was developed by *Kozeny* [1927], who treated the medium as a bundle of capillary tubes. LB and other numerical schemes that solve the Navier-Stokes equations can be used to test theoretical and empirical permeability relationships [*O'Connor and Fredrich*, 1999]. In this work, a coupled model simulates steady flow through stationary porous media and resulting permeability-porosity relationships are compared to established theoretical derivations.

5.5.1 Darcy's Law

To examine the relationship between fluid flux and pressure gradient, an LBDEM model composed of 200 discrete elements was developed. All solid elements in the model are fixed in space on a regular lattice. The fluid lattice is discretized at a high level to minimize grid resolution errors [*Boutt et al.*, 2003], with a minimum of 5 lattice nodes per pore throat . Pressure is fixed at a constant value at the top and bottom of the system and the system is allowed to evolve from an initial condition of constant pressure throughout the domain, as depicted in Figure 5.5a. As a result of the pressure boundary conditions, flow is driven from top to bottom of the assembly. Upon reaching steady state, defined here as flux-in equal to flux-out, the model run was terminated and fluid flux recorded. Fluid flux vs. pressure gradient are plotted in Figure 5.5b, and demonstrate a linear relationship. This linearity is consistent with Darcy's law with the slope of the line proportional to the permeability.

5.5.2 Porosity-Permeability Relationships

The Kozeny permeability formulation is written in terms of porosity, n, specific surface area with respect to a unit volume of porous medium, M, and Kozeny's constant, c_o, according to

$$k = \frac{c_o n^3}{M^2}. \tag{5.5}$$

Carmen [1937] used the previous equation, but expressed the specific surface with respect to the unit volume of solid, M_s, and used $c_o = 0.2$ derive the Kozeny-Carmen equation,

$$k = \frac{0.2 n^3}{M_s^2 (1 - n^2)}. \tag{5.6}$$

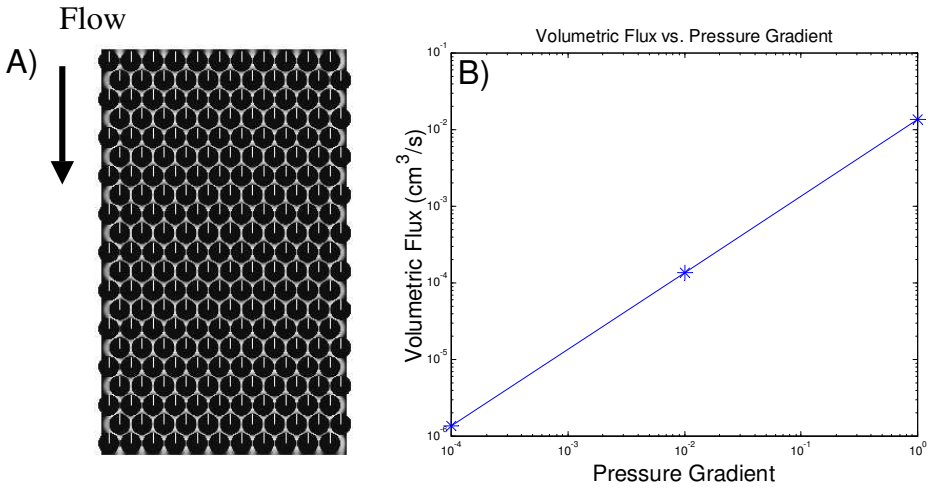

Figure 5.5: (a) Fluid flow through a finite number of stationary cylinders showing the acceleration and deceleration of fluid through pore throats. (b) A plot of volumetric flux vs. pressure gradient shows a linear relationship, as predicted by Darcy's law.

For cylinders of constant diameter D,

$$M_s = \frac{4\pi r^2}{2\pi r^3} = \frac{2}{D}, where r = 2D. \tag{5.7}$$

Substituting yields,

$$k = \frac{n^3}{20(1-n^2)} D^2. \tag{5.8}$$

For the coupled model studied here, the porosity and particle diameter are both known, thereby providing a relationship between these physical parameters and the permeability of the porous medium.

We examined this relationship with the LBDEM model for a range of model porosities and element (disc) diameters. Four models were developed, each with 200 circular discrete elements fixed in space. Model porosity was varied by changing the size of discrete elements. Boundary conditions and model geometry were identical to models used for the Darcy's law test, of Section 5.5.1. Relationships between porosity and permeability of the medium produced by the LBDEM are compared to the Kozeny-Carmen Equation, 5.8 in Figure 5.6. A reasonable match between theoretical and numerical results is demonstrated; however, these results are expected for such a simple geometry. When 5.8 is applied to more complicated models, with variable grain sizes and spatial distributions, the fit is not as consistent. The LBDEM is a tool that may be used to explore porosity-permeability relationships in systems too complex for theoretical analysis.

5.6 Unsteady Flow Through Non-Stationary Media

To test the full capability of the coupled LBDEM model, we examined unsteady fluid flows through non-stationary porous media. Most flows through

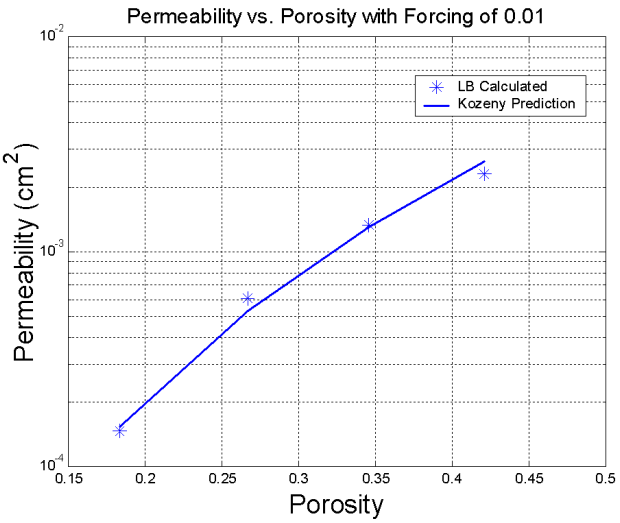

Figure 5.6: Permeability-Porosity relationships for simple models show a good match to what is predicted via Kozeny-Carmen theory.

porous media fall into this category. For example, flow to a shallow groundwater well in a confined aquifer includes elastic deformation of the aquifer material due to fluid pressure changes and converging flow around the well bore [*Helm*, 1994]. Sources of water for the well include deformation of the aquifer that releases water from storage and expansion of water volume following pressure reduction.

In the simpler problem of one-dimensional (1-D) consolidation of a layer of porous media, compaction of the aquifer material results in an increase in fluid pressure that forces fluid to flow out of the formation. Like the problem of flow to a well, elastic deformations of the solid framework and the fluid compressibility act together to influence changes in fluid pressure. In the following section we compare a simple 1-D analytical solution for fluid flow in a slightly

compressible elastic porous medium to LBDEM model simulations. We further compare the LBDEM model to poroelasticity theory using an extension of the analytical solution to a 1-D consolidation problem.

5.6.1 Fluid Flow in Slightly Compressible Porous Media

All of the previous results addressed steady-state porous media flows. We conducted several additional simulations to examine transient behavior in the LB-DEM models and to derive continuum parameters governing fluid flow, such as hydraulic diffusivity. We compared results of these simulations to those of an analytical solution.

In discrete models of porous media, averaged quantities such as permeability and diffusivity are not easily calculated, especially because of their scale dependence. In order to parameterize a porous media model, it is necessary to determine "micro" parameters, such as pore throat sizes and bond stiffnesses, as well as more intuitive "macro" or continuum parameters, such as permeability and Young's modulus. This has been previously accomplished for DEM models [*Boutt and McPherson*, 2002; *Potyondy and Cundall*, In Press] by comparing laboratory experimental results to numerical simulation results. In this paper, we are not specifically interested in comparing model results to actual observations in rocks, although we are currently performing this work. Thus, we will only compare the LBDEM to an analytical solution of fluid flow, and from those results infer continuum parameters governing the behavior of our current model setup.

The governing equation for 1-D slightly compressible fluid flow in an

isotropic homogeneous porous media in the absence of body forces is:

$$\frac{\partial P}{\partial t} = c\frac{\partial^2 P}{\partial x^2}, \tag{5.9}$$

where P is fluid pressure, t is time, x is a spatial coordinate, and c is the hydraulic diffusivity. The hydraulic diffusivity can be defined as

$$c = \frac{k}{\mu S}, \tag{5.10}$$

with the parameter (c) being a combination of the porous medium permeability (k) and storage capacity (S) or commonly referred to as the specific storage ($S = \frac{S_s}{\rho g}$). This is the only material parameter needed to fully define the transient flow field of an isotropic homogeneous porous medium. The specific storage is one of four properties in the general constitutive poroelastic equations and contains fluid and medium compressibility components [*Green and Wang*, 1990]. Through a structural homology with the mathematics of diffusion and heat conduction, Equation (5.9) is commonly referred to as the diffusion equation. Analytical solutions of this equation for various boundary conditions and initial conditions are widely available (e.g. *Carslaw and Jaeger* [1959]). One example is the 1-D fluid flow through a bounded domain subjected to constant fluid pressure boundaries with an initial condition of constant fluid pressure (P_o) throughout the domain. The analytical solution between

$$-L \leq x \leq +L, \tag{5.11}$$

for the boundary conditions

$$P(-L, t) = 0, P(L, t) = 0,$$

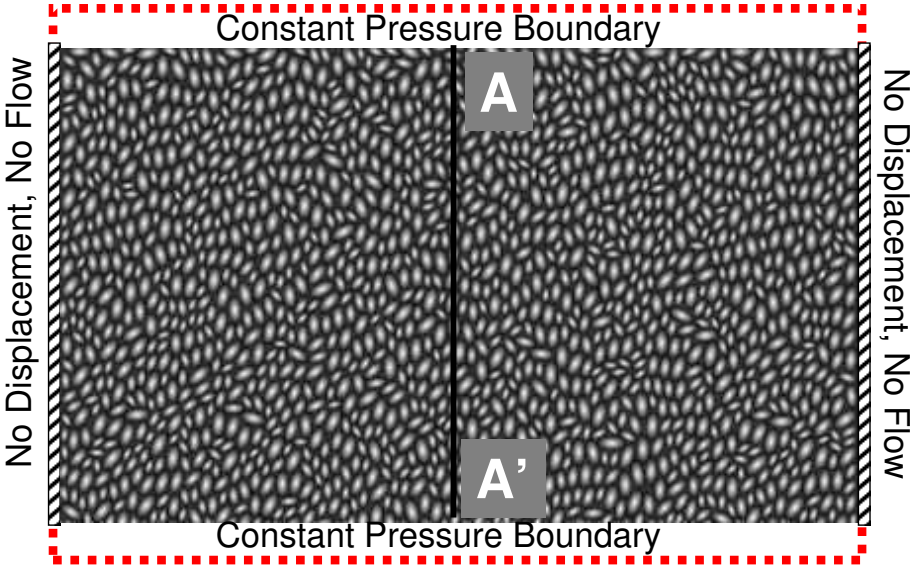

Figure 5.7: Conceptual model for 1-D fluid flow problem through non-stationary media. Line A to A' indicates cross-section depicted in Figure 5.8.

and the above described initial condition is

$$P(x,t) = P_o - P_o \sum_{n=0}^{\infty} (-1)^n \Big\{ erfc \frac{(2n+1)L - x}{2\sqrt{ct}} + erfc \frac{(2n+1)L + x}{2\sqrt{ct}} \Big\}. \tag{5.12}$$

The above analytical solution yields a pressure profile (pressure vs. length) that is diffusion-like. This type of behavior is important because it reflects both the storage and fluid transport properties of porous medium.

Table 5.2: Parameters for transient fluid flow and consolidation problem.

Solid	Values
Friction (-)	0.5
Normal Stiffness (Dyne/cm)	$8.00e+04$
Shear Stiffness (Dyne/cm)	$8.00e+04$
Element Size Range (cm)	0.11-0.07
Fluid Radius (-)	0.8
Fluid	Values
Viscosity ( )	0.1
Relaxation Time (-)	0.875
Node Spacing (cm)	0.0067
Timestep	$5.5e-5$

5.6.2 Transient Fluid Flow Through Porous Media With LBDEM Model

A LBDEM model was built to compare quantitatively the calculated results to expected analytical solution results. An assembly of approximately 1000 ellipse-shaped elements is packed into a 18 cm by 9 cm rectangular region bounded by discrete elements represented as lines (Figure 5.7). Physical properties of the discrete elements were assigned to mimic those of quartz grains (Table 5.2). No cohesion between elements was applied. The packing procedure consists of generating a uniform distribution (see Table 5.2 for range of radii) of elements on a regular lattice and letting them settle under gravity. Upon reaching equilibrium, the assembly is walled off and released from gravitational loading and allowed to come to equilibrium once again. Finally, the assembly is loaded via the walls to a desired stress state in this case, equivalent to atmospheric pressure on the side boundaries.

Because the LBDEM model is currently 2-D, it was necessary to apply different boundary conditions for the solids than those for the fluids to make it possible to compare results to the 1-D analytical solution. The dimension of the LBDEM model perpendicular to the fluid flow direction (horizontal in Figure 5.7) was extended and the boundaries assigned a no-displacement condition for solids and a no-flow condition for fluids. This assumption is similar to that of applying Equation (5.12) to fluid flow in an axi-symmetric right cylinder under similar boundary conditions. The boundary conditions for the fluid-flow parallel direction (vertical in Figure 5.7) for the LBDEM model are identical to those for the analytical solution with the solids given a free boundary. The fluid lattice was assigned dimensions of 735 by 401 for a total number of fluid nodes just under 300,000. The fluid lattice was initialized with a constant density (pressure) of 1 and both boundaries were fixed with a constant density of 0.999 during the simulation. The model was executed until the pressure in the pore spaces came to equilibrium with the boundary condition.

One-dimensional cross-sections through the model were chosen for the purpose of comparison to the analytical solution. A typical cross-section (A-A' on Figure 5.7) is plotted in Figure 5.8, depicting solid ratios as a function of distance along the flow-parallel direction of the model. A single cross section may consist of more than 70% solid particles. Eleven separate vertical cross sections through the model were chosen such that only fluid pressure values from fluid-only nodes (solid ratio =0) were considered. The values were then arithmetically averaged and plotted on an x-y plot with respect to normalized pressure ($\frac{P}{P_o}$) and distance along the flow direction. The results for eight different times during the model run are illustrated for half of the domain in

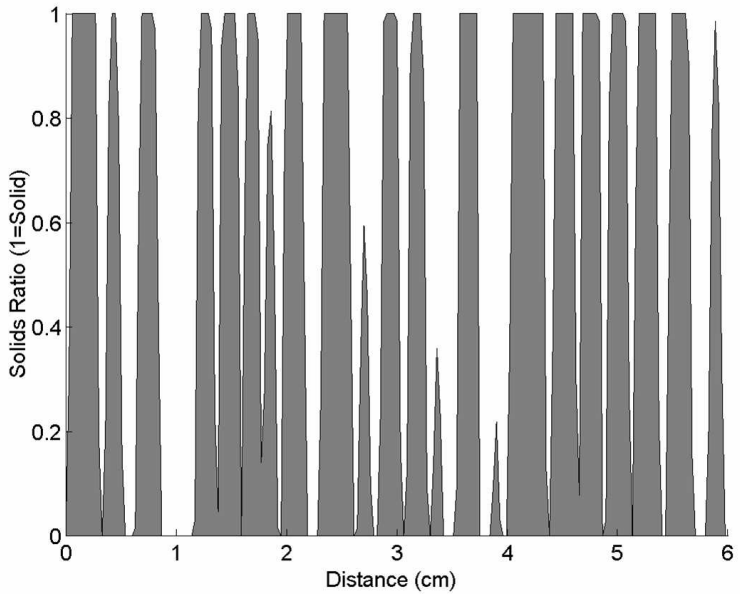

Figure 5.8: The solid ratios along cross-section A-A' in Figure 5.7. An averaging scheme was used such that only completely fluid-filled nodes are analyzed. Gray filled areas are solids.

Figure 5.9, with $x = 0$ corresponding with the outer boundary where the pressure is held constant at 0 (and $x = 4.5$ corresponding with the center of the specimen) . The data portray diffusion-like profiles, where higher fluid pressure is forced to come into equilibrium with lower pressure boundary conditions. In each plotted curve, especially later time curves, small inconsistencies between the smooth analaytical solution and the LBDEM exist. It is hypothesized that heterogeneous pore body and throat size distributions are causing these deviations. Deviations are similar for results plotted at the same location but at different times, suggesting the deviations are location specific. On average, the variability is fairly small with respect to the overall pressure magnitude.

The analytical solutions (solid lines) to Equation (5.12) are plotted

on Figure 5.9. Best fit results were computed with a hydraulic diffusivity of $7.9\frac{cm^2}{s}$. This value is higher than those reported by *Wang* [2000] for sandstone ($c \approx 1\frac{cm^2}{s}$), but not unexpected for a 2-D model with less tortuousity of flow paths that would exist in a real rock. Larger values of hydraulic diffusivity will cause fluid pressure to reach equilibrium faster. It appears that the fit between the calculated fluid pressure and the analytical solution is a strong function of time. Larger discrepancies between the solutions occur at the boundaries. Sources of error in the LBDEM compared to the presented analytical solution may arise from multiple sources. First of all the analytical solution is for a homogeneous material, which this model does not satisfy. Second, assumptions in the analytical solution may not be met near the boundaries of the model.

5.6.3 Conceptual Model of 1-D Consolidation

Consolidation of saturated porous media was first examined by *Terzaghi* [1925, 1943] and later applied to many problems in geomechanics and hydrogeology (e.g. *Domenico and Mifflin* [1965]). In Terzaghi's formulation of 1-D consolidation, a sudden stress of σ_o is applied on the surface of a finite length (L) fluid-saturated porous medium with an impermeable bottom boundary. The top boundary is drained, such that fluid can freely leave the system. The governing equation for this problem is identical to the fluid diffusion problem described above if the stress applied is not a function of time, which is the classic assumption. This allows the pore fluid diffusion equation to be uncoupled from the mechanical equilibrium equations and results in an analytical solution that is similar to Equation (5.12).

As predicted from poroelasticity theory, the instantaneous pressure

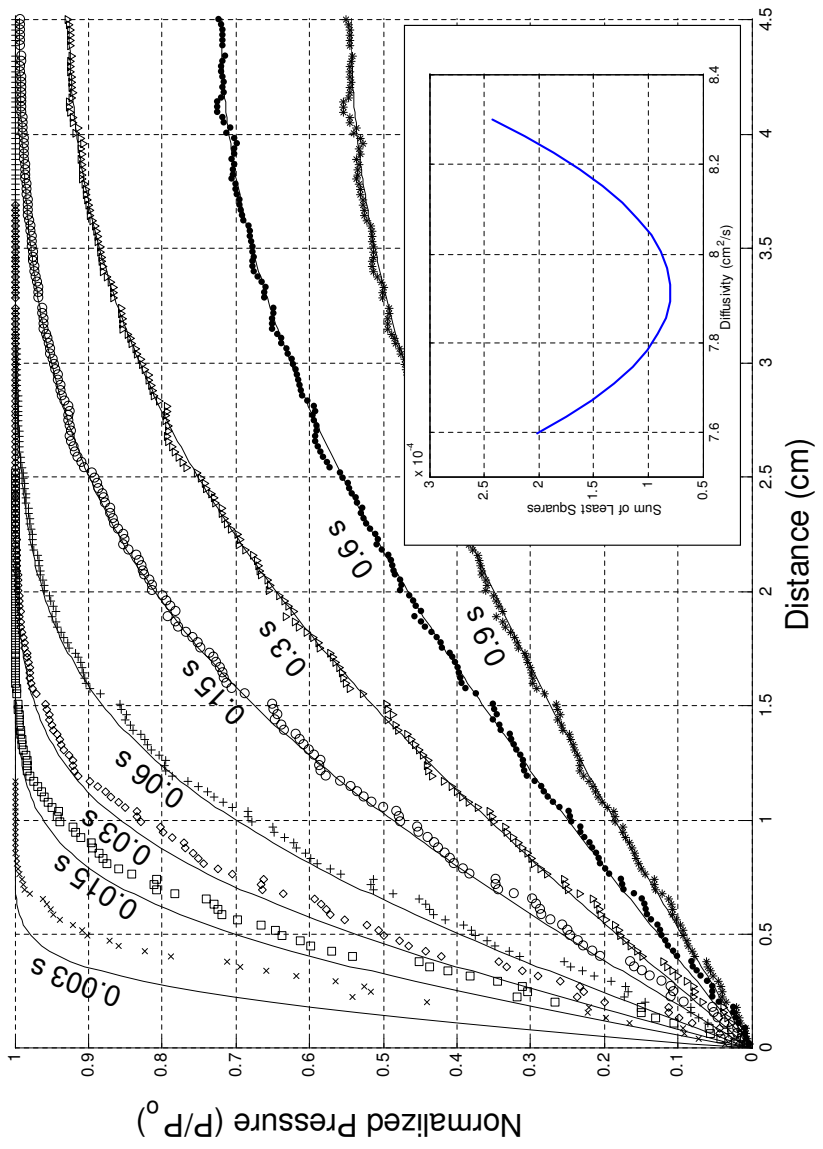

Figure 5.9: Plots of normalized pressure vs. distance for the LBDEM solution are shown as different symbols for eight times during the simulation. Also plotted are the analytical solutions (solid lines) at the same times using a diffusivity of $7.9\frac{cm2}{s}$. Inset: Sum of least squares of diffusivity for model results.

change in the porous medium is described by $\gamma\sigma_o$, where γ is the loading efficiency. Note that the $\gamma\sigma_o$ response is identical to an undrained response. If $\gamma = 1$, the entire applied load is converted into an exactly equivalent pressure change in the porous media. In reality γ is $<< 1$, as some of the load is not directly transmitted to the fluid. *Valliappan et al.* [1995] showed that the effect of the pore fluid is dominant only for fully saturated soils with incompressible solid grains and low permeability. For partially saturated, compressible or very permeable media (this study), the stresses would be largely transferred to the solids. The instantaneous pressure distribution, which is a function of applied stress, is used as the initial condition in the solution of the governing equation. The analytical solution in terms of pore pressure [*Wang*, 2000] is

$$P(x,t) = \gamma\sigma_o - \gamma\sigma_o \sum_{n=0}^{\infty} (-1)^n \Big\{ erfc\frac{(2n+1)L-(x-L)}{2\sqrt{ct}} + erfc\frac{(2n+1)L+(x-L)}{2\sqrt{ct}} \Big\}, \tag{5.13}$$

where x and t are spatial and temporal dimensions. This uniaxial strain formulation assumes elastic reversible deformation in the grain framework with negligible grain compressibility. The increase in fluid pressure due to the consolidation in the sample results in a net pressure gradient in the direction of the drained top boundary. As fluid leaves the sample the system slowly returns to equilibrium. The primary parameter governing how quickly fluid escapes the porous medium is the hydraulic diffusivity (c). These properties of the analytical solution are shown in a depth vs. time plot of the analytical solution for $\gamma = 1$ and $c = 7.9$ in Figure 5.10a. Highest fluid pressures are adjacent to the bottom no-flow boundary.

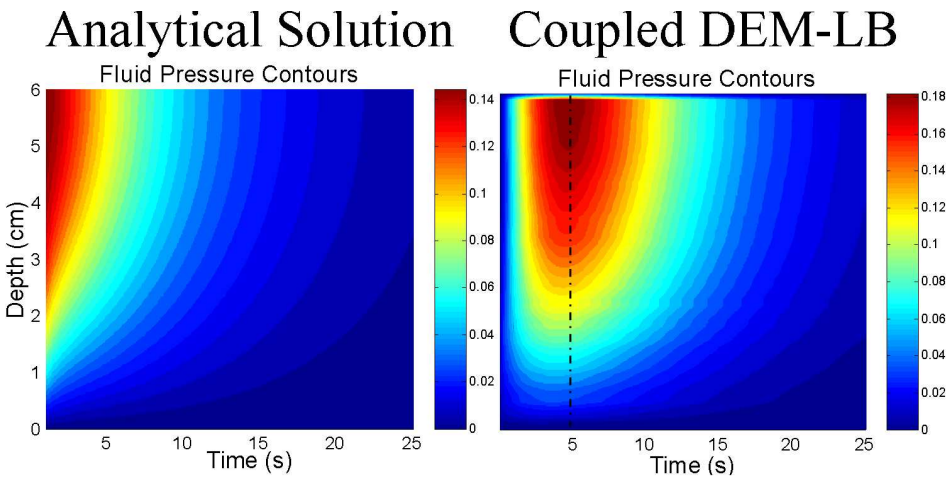

Figure 5.10: Analytical solution and LBDEM solution for Terzaghi's consolidation problem. Analytical solution assumes ideal poroelastic response therefore solutions are not identical.

5.6.4 Results of 1-D consolidation With LBDEM Model

We explored consolidation behavior using the coupled model using the setup depicted in Figure 5.11. An assembly of approximately 1000 discs is packed into a 11 cm by 6 cm rectangular region bounded by discrete elements represented as lines. Physical properties of the discrete elements were assigned to mimic those of quartz grains (Table 5.2). The assembly of elements in Figure 5.11 was prepared identically to the previously described model of Figure 5.7. Since the analytical solutions uses an assumption of idealized poroelastic behavior and hence simplifies the governing equation, the main test for the LBDEM model is to demonstrate fluid pressurization as a result of an applied stress. The top boundary was assigned at a constant applied stress with a porous discrete element such that fluid flow is not impeded by the element. The fluid at this boundary is maintained at zero gauge pressure. The bottom

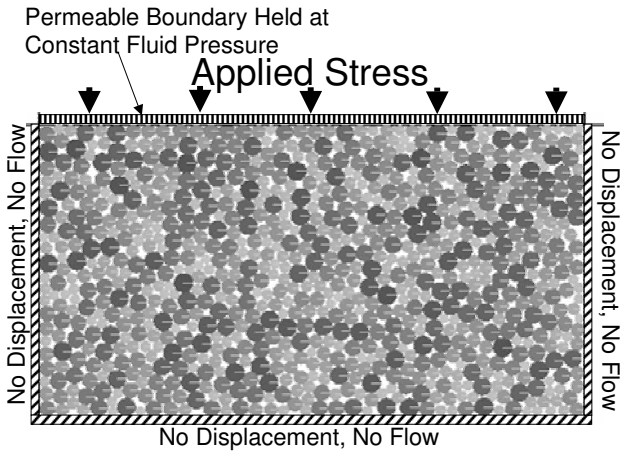

Figure 5.11: Conceptual model for consolidation problem. Top boundary condition is drained and held at constant fluid pressure.

boundary is specified as a no-flow and no-displacement boundary. Initially the solid framework is in equilibrium with boundary conditions and the fluid pressure is constant throughout the assembly.

The simulation begins with an application of the stress boundary condition on the drained boundary (top). In response to this condition, the assembly of cylinders begins to consolidate and fluid pressure rises. Early time results of Figure 5.10b illustrate this behavior for the fluid pressure response. The averaging technique used for the fluid diffusion problem was also applied to the consolidation problem. The smoothed filled contour plot in Figure 5.10b was generated through interpolation of the completely fluid filled nodes from the 11 cross-sections. A comparison of the two results suggests a lag time in the response of fluid pressure in the LBDEM simulation with respect to the maximum value of fluid pressure (dashed line on Figure 5.10b). Unlike the an-

Table 5.3: Fluid wave speeds for simulated fluid and real fluids (at STP)

Fluid	**Fluid Wave Speed ($\frac{m}{s}$)**
LB simulated fluid	2.3
Air	331
Water	1482
Brine	1534

alytical solution (Figure 5.10a), which assumes an ideal poroelastic response of $\gamma\sigma_o$ as an initial condition, the coupled model has a finite wave speed. Therefore, the response of the assembly to the new boundary condition takes a finite amount of time to reach the maximum fluid pressure. In reality, experimental evidence [*Gunaratne et al.*, 1996] using a dynamically applied stress suggests that the time to reach peak fluid pressure is finite and on the order of tenths of seconds depending on material properties. These properties have been suggested [*Gunaratne et al.*, 1996; *Valliappan et al.*, 1995] to include the degree of saturation, permeability, and media compressibility.

The two dynamic wave speeds in LBDEM are the solid wave speed and the fluid wave speed. The solid wave speed is a function of element stiffness, where as the fluid wave speed is related to model viscosity and discretization. The numerical value of fluid wave speed in the LB method is significantly smaller than actual wave speeds in real fluids (Table 5.3). In a model with finite solid and fluid wave speed, attaining a fluid pressure response that is exactly equivalent to that of the initial condition of the analytical solution is impossible. The sensitivity of these two parameters and their pressure response is now explored using the above consolidation problem.

To assess the poroelastic response of the LBDEM model, we analyzed the time it took to reach the maximum value of fluid pressure as a function of both the fluid wave speed and the solid wave speed. The solid wave speed was varied by over 5 orders of magnitude by changing the element-to-element contact stiffness. All other model parameters, including fluid wave speed, were held constant in the simulations. The element stiffness, which is related to the characteristic frequency of the system and inversely related to the numerical timestep, is proportional to the modulus of the material [*Potyondy and Cundall*, In Press]. Thus higher stiffnesses between elements typically yields an effectively stiffer modeled rock. Plotted in Figure 5.12 are the results for the solid wave speed sensitivity as a function of peak fluid pressure following an applied load. This measure was chosen because this response is only a function of the poroelastic properties of the models (see Figure 5.10). As the element stiffness is increased, the time to reach the peak fluid pressure is reduced. The change from a fairly slow response ($\sim$ 6 seconds) to quick response ($\sim$ 0.03 seconds) occurs over a small change in element stiffness. Similar increases in element stiffness do not change the time to reach peak fluid pressure significantly. A two parameter exponential model fits this trend quite well (within the 95% confidence interval). This suggests that some threshold solid wave propagation speed exists at which the fluid pressure response is not significantly affected. Regardless of this fact, element stiffness dramatically affects fluid pressure rise in the consolidation problem. We now explore the fluid wave speed effect on fluid pressure response.

Fluid wave speeds or speeds of sound (c_s) were varied by refining the discretization of the fluid lattice and keeping all other model properties

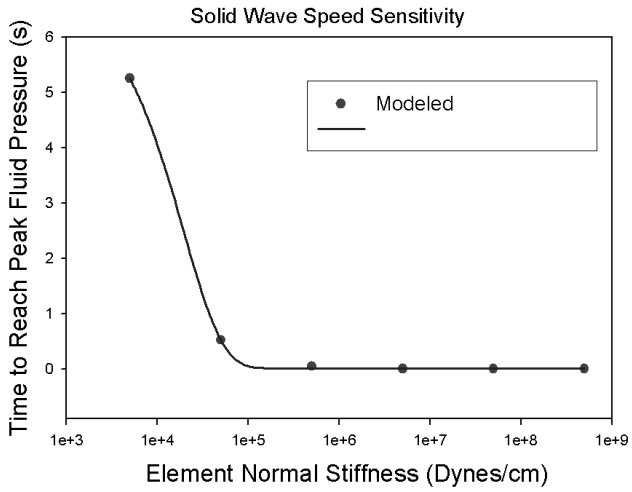

Figure 5.12: The sensitivity of the time for the fluid pressure to reach its peak value is a function of the solid wave speed. With small changes in element stiffness, the time to reach the peak fluid pressure in the system is much smaller.

constant. The numerical fluid speed is the velocity with which information is propagated across the fluid lattice. The sensitivity of the fluid speed of sound on the timing of the peak fluid pressure is plotted in Figure 5.13 for five different fluid wave speeds. The response of the system to the applied loading is clearly a function of the fluid speed of sound, but the response occurs over a much smaller range of values than for the solid wave speed presented above. From the figure it is evident that the peak fluid pressure is reached sooner in the high fluid speed models vs. the low fluid speed models. This behavior results from the faster transfer of changes in boundary conditions (and resulting particle displacements) to the fluid. This response is not linear, but is better fit by a 2 parameter exponential model (solid line).

Recall that the coupling between the LB and the DEM is achieved through a fluid velocity condition on the element boundary. This coupling

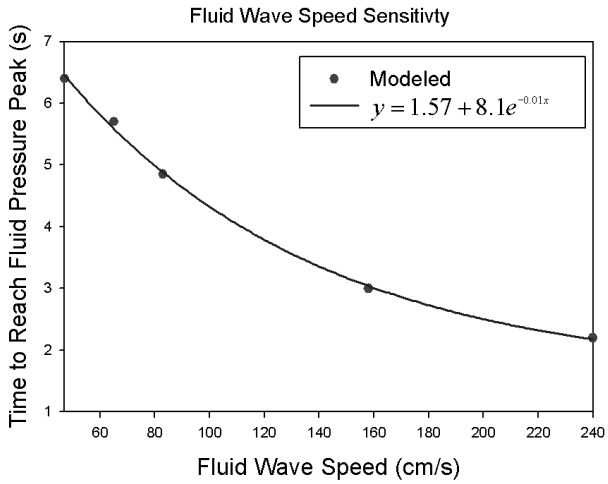

Figure 5.13: The time for the fluid pressure to reach its peak value is much less sensitive to fluid wave speed than solid wave speed. Relative to the solid wave speed sensitivity, the time quickly levels out and fluid speeds well below that of water can approximate this response well.

method together with the evidence presented above suggests that the propagation of boundary conditions to the interior of the model is most important. Secondly, once the change in far-field boundary conditions reaches the element this information is then transmitted to the fluid. Since the fluid occupies a relatively small volume compared to the solid elements, the time constant for that process is small. Overall, the affect of fluid wave speed on the poroelastic response is important on the local element scale and not on the scale of the overall length of the model specimen for the problems of interest. This suggests that the much smaller fluid wave speeds in the LB can produce first order behavior in these types of problems. In LBDEM problems with large fluid voids and cavities, the discrepancy between the fluid wave speed of the LBDEM and real fluids will be more significant.

An additional advantage of this formulation is that it is possible to probe deeper into the model by examining different micromechanical variables associated with the solid and fluid components of the system. Contact forces (a) and fluid speeds (b) are depicted in Figure 5.14 for the whole 2-D section at $15s$. Contact forces (brown indicates normal and gray shear force) show the effect of applying the constant load on the top boundary. Fluid speeds (warm colors indicate higher speeds where as cool colors are lower speeds) indicate that fluid is flowing toward the constant pressure boundary condition. Note the variability in fluid flow throughout the specimen, which is a function of pore throat size.

5.7 Conclusions

This paper presents the application of a robust, direct fluid-solid coupling scheme to the mechanics of fluid-solid coupling in porous media. The model is built on discrete methods of solid (DEM) and fluid (LB) mechanics. Coupling is achieved through momentum transfer from the fluid to the solid and through the enforcement of a no-slip condition of the solid onto the fluid. By handling the coupling directly we avoid the typical assumptions of Darcy flow and effective stress and are able to model a variety of problems including deforming materials (such as fractures). We show the applicability of the model by first examining some idealized flow through stationary porous media and then performing more complex simulations using the full capability of the coupled model.

The previously validated model [*Cook*, 2001] was extended for use in porous media applications by adding boundary conditions and idealizing

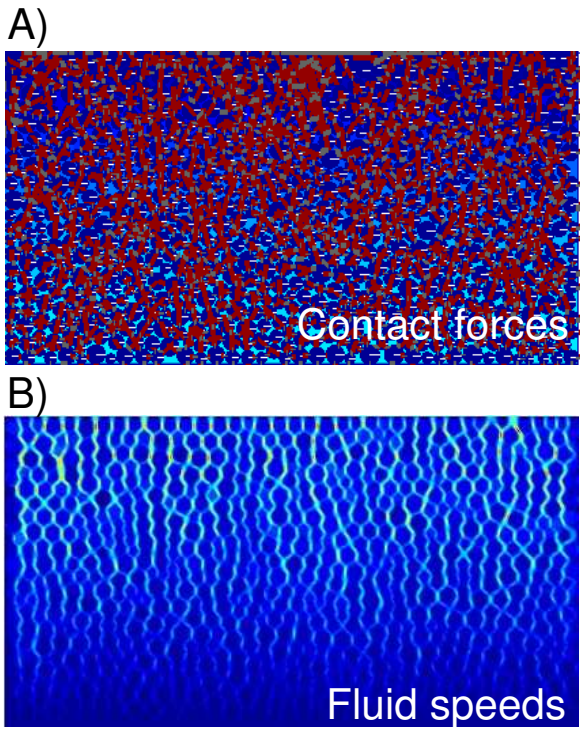

Figure 5.14: Additional data from the consolidation test can give insight into the physics of the coupled system. Shown here are contact forces (A) and fluid speeds (B) for the consolidation test. Normal contact forces are depicted as thick lines parallel to contact normal. Higher fluid velocities are represented as brighter contours that converge on the draining boundary.

the 2-D flow domain. Modeled fluid flow through periodic arrays of cylinders at various Reynolds numbers are shown to match very well with previous experimental and numerical results. For a range of solid concentrations we accurately match the results of previous researchers, indicating that the correct fluid mechanics are being resolved. Simulations of flow through stationary cylinders yield a linear relationship between volumetric fluid flux and pressure gradient across the sample. Comparisons of porosity-permeability relationships predicted by the Kozeny-Carmen equation and the LBDEM model results are consistent for simple geometries.

LBDEM models were developed that enabled the comparison of 1-D analytical solutions of fluid flow in slightly compressible porous media. The results from this comparison indicate that the LBDEM is achieving a good match with the analytical solution. Deviations occur as a result of pore-scale nature of our model. In addition, the hydraulic diffusivity is slightly larger than that of similar geologic material. This may be due to the fact that the models have a fairly small number of particles and their permeability is higher than the equivalent geologic material.

The consolidation of saturated porous media showed the dynamic and poroelastic response of the LBDEM model. Given that we are solving the fully dynamic equations of motion for both the fluid and solid, direct comparisons with instantaneous undrained responses are not possible. With this in mind, the model qualitatively captures consolidation behavior appropriately, including both initial pressurization and fluid flow out of the domain.

The control of the numerical fluid wave speed on the poroelastic re-

sponse is important on the local element scale but not on the scale of the overall length of the model specimen for the problems of interest. This suggests that numerical fluid wave speeds smaller than those of real fluids are not necessary to produce first order behavior in these types of problems. In LBDEM problem domains with large fluid voids and cavities, the discrepancy between the fluid wave speed of the LBDEM and real fluids will be more significant.

5.A Appendix: Lattice-Boltzmann and Coupled Model Theory (excerpted with permission from *Cook* [2001]

In LB techniques, fluid is represented as packets of mass that move about a regular lattice, or grid, defined with appropriate boundary conditions. Collision and redistribution, or streaming, of fluid packets occur at lattice nodes according to specific relationships that conserve mass and momentum, and recover the Navier-Stokes equation to second order in time and space. Most of the computational cost incurred at each timestep is associated with the collision phase, which is local in nature. The only data exchange between lattice nodes occurs during the streaming of the distributions. The model uses the linearized, Bhatnagar-Gross-Krook single-time relaxation form of the LB equation,

$$f_i(\mathbf{x} + \mathbf{e}_i \Delta t, t + \Delta t) = f_i(\mathbf{x}, t) - \frac{\Delta t}{\tau}(f_i(\mathbf{x}, t) - f_i^{eq}(\mathbf{x}, t)), \tag{5.14}$$

where $f_i(\mathbf{x}, t)$ is the fluid particle density distribution with velocity $\mathbf{e}_i$ at a node located at position x for a given time t; τ is the relaxation time; and $f_i^{eq}(\mathbf{x}, t)$ is the equilibrium density distribution for the fluid. *Cook* [2001]'s two-dimensional model uses a square, nine-velocity lattice referred to as the D2Q9 model [*Qian et al.*, 1992]. At each node there are eight density distributions, f_i,

with non-zero velocities. There is also a zero-velocity or rest distribution at each node, f_0. The macroscopic fluid variables at a node, density, ρ, and velocity, $\mathbf{v}$, are found from the moments of the fluid particle density distribution:

$$\mathbf{v} = \frac{\sum_i f_i \mathbf{e}_i}{\rho}, \rho = \sum_i f_i. \tag{5.15}$$

LB simulates a slightly compressible fluid; consequently, fluid pressure, P, is given by the following equation of state

$$P = c_s^2 \rho. \tag{5.16}$$

This simple relationship for pressure gives LB a distinct advantage over traditional Navier-Stokes solvers, which must solve the Poisson equation for pressure. Coupling with discrete elements is accomplished through a moving solid boundary condition. At a minimum, a physically correct condition must impose identical velocities along fluid-solid interfaces. For computational expediency, *Cook* [2001] adopted an immersed moving boundary scheme proposed by *Noble and Torczynski* [1998]. The modified LB equation for solid-covered nodes becomes

$$f_i(\mathbf{x} + \mathbf{e}_i \Delta t, t + \Delta t) = f_i(\mathbf{x}, t) - \frac{\Delta t}{\tau}(1 - B)(f_i(\mathbf{x}, t) - f_i^{eq}(\mathbf{x}, t)) + B\Omega_i^S, \tag{5.17}$$

where B is a weighting function that depends on the local solid fraction or solid ratio, ε, defined here as the fraction of the nodal area covered by a solid(s), and the dimensionless relaxation time according to

$$B(\varepsilon, \tau^*) = \frac{\varepsilon(\tau^* - 1/2)}{(1-\varepsilon) + (\tau^* - 1/2)}. \tag{5.18}$$

Ω^S is an additional collision term that bounces back the non-equilibrium portion of the distribution and is given by

$$\Omega_i^S = f_{-i}(\mathbf{x}, t) - f_i(\mathbf{x}, t) + f_i^{eq}(\rho, \mathbf{v}_s) - f_{-i}^{eq}(\rho, \mathbf{v}), \tag{5.19}$$

where $\mathbf{v}_s$ is the solid's velocity at time t, and $-i$ is used to denote the distribution component having the opposite direction to i. The result from (5.17) is to modify the density distributions at those nodes covered by a solid in such a way that the fluid velocity matches the solid's rigid body motion, thereby enforcing a no-flow condition. An important advantage of this boundary condition is that it allows for the sub-grid resolution of moving boundaries through the solid ratio term.

Fluid dynamics in a particle-fluid system is influenced by the presence of solids, and the displacements of solids (discrete elements) are, in turn, driven by fluid-induced forces. The moving boundary condition presented above accounts for the effect of moving solids on fluid flow; coupling is completed with the computation of the fluid-induced forces on solids. The force of the fluid, F_f, on a discrete element can be found by summing up the momentum transfer that occurs over the m nodes covered by the element as

$$\mathbf{F}_f = \frac{h^2}{\Delta t} \sum_m B_m \sum_i \Omega_i^S \mathbf{e}_i, \tag{5.20}$$

where h is the nodal spacing. Fluid-induced torque, $\mathbf{T}_f$, is calculated similarly,

$$\mathbf{T}_f = \frac{h^2}{\Delta t} \sum_m (\mathbf{x} - \mathbf{x}_s) \times (B_m \sum_i \Omega_i^S \mathbf{e}_i), \tag{5.21}$$

where $\mathbf{x}_s$ is the centroid of the solid particle at time t. Fluid-particle coupling is realized at each timestep by first computing the fluid solution, and then updating solid particle positions through integration of the equations of motion.

References

Bergelin, O., A. Colburn, and H. Hall, *Engineering Experiment Station Bulletin 50*, University of Delaware, 1950.

Boutt, D. F., and B. J. McPherson, Simulation of sedimentary rock deformation: Lab-scale model calibration and parameterization, *Geophysical Research Letters*, *29*, 10.1029/2001GL013,987, 2002.

Boutt, D. F., B. K. Cook, B. J. McPherson, and J. Williams, Application of a directly coupled numerical model of fluid-solid mechanics, in *Soil and Rock America 2003*, edited by T. Culligan, A. Whittle, and H. Einstein, MIT, Cambridge, MA, 2003.

Bruno, M., Micromechanics of stress-induced permeability anisotropy and damage in sedimentary rock, *Mechanics of Materials*, *18*, 31–48, 1994.

Bruno, M., and R. Nelson, Microstructural analysis of the inelastic behavior of sedimentary rock, *Mechanics of Materials*, *12*, 95–118, 1991.

Bruno, M., A. Dorfmann, K. Lao, and C. Honeger, Coupled particle and fluid flow modeling of fracture and slurry injection in weakly consolidated granular media, in *Rock Mechanics in the National Interest*, edited by Elsworth, Tinucci, and Heasley, Swets and Zeitlinger Lisse, Washington, D.C., 2001.

Carmen, P., Fluid flow through a granular bed, *Transactions of the Institute of Chemistry and Engineering - London*, *15*, 150–156, 1937.

Carslaw, H., and J. Jaeger, *Conduction of Heat in Solids*, 2nd ed., Clarendon Press, Oxford, 1959.

Cook, B., D. Noble, D. Preece, and J. Williams, Direct simulation of particle laden fluids, in *Fourth North American Rock Mechanics Symposium.*, A.A. Balkema, Rotterdam, 2000.

Cook, B., D. Noble, D. Preece, and J. Williams, Direct simulation of particle laden fluids, *Journal of Engineering Computations*, in press.

Cook, B. K., A numerical framework for the direct simulation of solid-fluid systems, Doctoral dissertation, Massachusetts Institute of Technology, 2001.

Cundall, P., A computer model for simulating progressive, large-scale movement in block rock systems, in *Rock fracture*, edited by Anonymous, vol. 1, Int. Soc. Rock Mech., France, 1971.

Cundall, P., and O. Strack, A discrete element model for granular assemblies, *Geotechnique*, *29*, 47–65, 1979.

Cundall, P., A. Drescher, and O. Strack, Numercal experiments on granular assemblies: Measurements and observations, in *Deformation and Failure of Granular Materials*, edited by J. Jenkins and H. Luger, A.A. Balkema, Brookfield, VT, 1982.

Domenico, P., and M. Mifflin, Water from low permeability sediments and land subsidence, *Water Resources Research*, *4*, 563–576, 1965.

Edwards, D., M. Shapiro, P. Bar-Yoseph, and M. Shapira, The influence of Reynolds number upon the apparent permeability of spatially periodic arrays of cylinders, *Physics of Fluids A*, *2*, 45–55, 1990.

Flekkoy, E. G., and A. Malthe-Sorenssen, Modeling hydrofracture, *Journal of Geophysical Research*, *107*, 2151–2151, 2002.

Green, D., and H. Wang, Specific storage as a poroelastic coefficient, *Water Resources Research*, *26*, 1631–1637, 1990.

Gunaratne, M., M. Ranganath, S. Thilakasiri, G. Mullins, P. Stinnette, and C. Kuo, Study of pore pressures induced in laboratory dynamic consolidation, *Computers and Geotechnics*, *18*, 127–143, 1996.

Hazzard, J., P. F. Young, and S. Maxwell, Micromechanical modeling of cracking and failure in brittle rocks, *Journal of Geophysics Research*, *105*, 16,683–16,697, 2000.

Helm, D. C., Horizontal aquifer movement in a Theis-Thiem confined system, *Water Resources Research*, *30*, 953–964, 1994.

Hill, R., D. Koch, and A. Ladd, The first effects of fluid inertia on flows in ordered and random arrays of spheres, *Journal of Fluid Mechanics*, *448*, 213–241, 2001.

Klosek, J., The integration of fluid dynamics with a discrete-element modelling system : Algorithms, implementation, and applications, Masters thesis, Massachusetts Institute of Technology IT, 1997.

Koch, D., and A. Ladd, Moderate reynolds number flows through periodic and random arrays of alligned cylinders, *Journal of Fluid Mechanics*, *349*, 31–66, 1997.

Kozeny, J., Uber kapillare leitung des wassers im boden, *Sitzungsber. Akad. Wiss. Wien*, *136*, 207–306, 1927.

Li, L., and R. Holt, Simulation of flow in sandstone with fluid coupled particle model, in *Proceedings of the 38th U.S. Rock Mechanics Symposium: Rock Mechanics in the National Interest*, edited by D. Elsworth, J. P. Tinucci, and A. Heasley, pp. 511–516, A.A. Balkema, Rotterdam, 2001.

McPherson, B., and J. Bredehoeft, Overpressures in the Uinta basin, Utah: Analysis using a three-dimensional basin evolution model, *Water Resources Research*, *37*, 857–872, 2001.

Moore, L. P., and N. R. Iverson, Slow episodic shear of granular materials regulated by dilatant strengthing, *Geology*, *30*, 843–846, 2002.

Neuzil, C., Abnormal pressures as hydrodynamic phenomena, *American Journal of Science*, *295*, 742–786, 1995.

Neuzil, C. E., Hydromechanical coupling in geologic processes, *Hydrogeology Journal*, *11*, 41–83, 2003.

Noble, D., and J. Torczynski, A lattice boltzman method for partially saturated computational cells, *International Journal of Modern Physics*, *C9*, 1189–201, 1998.

O'Connor, R., and J. Fredrich, Microscale flow modeling in geologic materials, *Physics and Chemistry of the Earth (A)*, *24*, 611–616, 1999.

O'Connor, R., J. Torczynski, D. Preece, J. Klosek, and J. Williams, Discrete element modeling of sand production, *International Journal of Rock Mechanics and Mining Sciences*, *34*, 231, 1997.

Potyondy, D., P. Cundall, and C. Lee, Modeling rock using bonded assemblies of circular particles, in *Rock Mechanics: Tools and Techniques*, edited by Aubertin, Hassani, and Mitri, pp. 1937–1944, A.A. Balkema, Rotterdam, 1996.

Potyondy, D. O., and P. A. Cundall, A bonded-particle model for rock, *International journal of rock mechanics and mining sciences*, In Press.

Qian, Y., D. Dhumieres, and P. Lallemand, Lattice BGK models for Navier-Stokes equation., *Europhysics Letters*, *17*, 479–484, 1992.

Rege, N., Computational modeling of granular materials, Doctoral dissertation, Massachusetts Institute of Technology, 1996.

Saffer, D., and B. A. Bekins, Hydrologic controls on the morphology and mechanics of accretionary wedges, *Geology*, *30*, 271–274, 2002.

Sagani, A., and A. Acrivos, Slow flow past periodic arrays of cylinders with application to heat transfer, *International Journal of Multiphase Flow*, *8*, 193–206, 1982.

Sakaguchi, H., and H.-B. Muhlhaus, Hydrid modeling of coupled pore fluid-solid deformation problems, *Pure and Applied Geophysics*, *157*, 1889–1904, 2000.

Simpson, G., Influence of compression-induced fluid pressures on rock strength in the brittle crust, *Journal of Geophysical Research*, *106*, 19,465–19,478, 2001.

Stephansson, O., Theme issue on hydromechanics in geology and geotechnics, *Hydrogeology Journal*, *11*, DOI 10.1007/s10,040–002–0247–z, 2003.

Terzaghi, K., *Erdbaumechanik auf Bodenphysikalischer Grundlage*, Deuticke, Leipzig, 1925.

Terzaghi, K., *Theoretical Soil Mechanics*, John Wiley, New York, 1943.

Valliappan, S., J. Yazdi, and C. Zhao, Analytical solution for two-dimensional dynamic consolidation in frequency domain, *International Journal of Numerical and Analytical Methods in Geomechanics*, *19*, 663–682, 1995.

Wang, H., *Theory of Linear Poroelasticity: with Applications to Geomechanics and Hydrogeology*, Princeton University Press, Princeton, New Jersey, 2000.

Yow, J., and J. Hunt, Coupled processes in rock mass performance with emphasis on nuclear waste isolation, *International Journal of Rock Mechanics and Mining Sciences*, *39*, 143–1150, 2002.

Zou, Q., and X. He, On pressure and velocity boundary conditions for the lattice-Boltzmann method, *Physics of Fluids (A)*, *9*, 1591–1598, 1997.

CHAPTER 6

NUMERICAL AND EXPERIMENTAL INVESTIGATION OF THE ROLE OF FLUID PRESSURE GRADIENTS IN FRACTURE GENESIS

Abstract

Empirical and theoretical criteria define the amount of stress a given body of rock can support before fracturing, but lack a direct connection between fluid transport and mechanical properties. In this dissertation I develop these concepts using poroelasticity theory, and devise a new experimental test to address these issues. This test is employed in a discrete numerical model of coupled fluid and solid physics. The LBDEM formulation couples the lattice-Boltzmann method (LB) for fluid mechanics and the discrete element method (DEM) for solid mechanics. Previous studies demonstrated that LBDEM, a directly coupled, physically based model, captures basic poroelastic behavior. The numerical simulations of fracture formation produce opening mode fractures that are demonstrably fluid driven. The effect of increasing permeability in the models is to increase the fracture propagation rate and to slightly decrease bond breakage. It appears that bulk forcing of the solid by the fluid is one of the factors driving fracture genesis. In models with identical bulk fluid pressure gradients, local fluid pressure gradients strongly influence the state of stress in the solids, and on the fracture growth. Additionally, experimental im-

plementation under the same conditions imposed in the numerical simulations produced similar through going extension fractures.

6.1 Introduction

Pore fluid pressure within the Earth's shallow crust can reach high values relative to the hydrostatic gradient [*Neuzil*, 1995]. Previous research suggests that the fluid pressure can reach levels high enough to fracture the rock. The importance and existence of these so-called natural hydraulic fractures (NHF) in the Earth's crust has been debated for over 30 years [*Secor*, 1965], yet the conditions under which NHFs form remains controversial. Structural geologists commonly interpret extension fractures found in sedimentary basins [*Engelder and Lacazette*, 1990; *Cruikshank et al.*, 1991; *Capuano*, 1993; *Foxford et al.*, 2000; *Bahat et al.*, 2003]. Additionally, NHFs are called upon to mitigate high pore fluid pressure in basins through increased permeability [*McPherson and Bredehoeft*, 2001; *LHeureux and Fowler*, 2000; *Bradley and Powley*, 1994; *Roberts and Nunn*, 1995]. When viewed from either perspective, NHFs form a large piece of the feedback loop between structural (mechanical) and hydrological processes in sedimentary basins. A better understanding of the intrinsic and extrinsic conditions under which NHFs form will allow structural geologists and hydrogeologists to make better estimates of their extent and importance in the geologic record.

The focus of this paper is the hydrological properties of rocks in the genesis of NHF's. This is accomplished through the development of a new set of conditions that cause fluid-induced extension fractures to form with appropriate boundary conditions. The hydraulic fracture setup is implemented in a fully-

coupled numerical model, which is executed for a variety of rock permeabilities.

6.2 Previous Work

Recent work by *Renshaw and Harvey* [1994] addressed the quasi-static growth rates of NHFs. They simulated NHFs in poroelastic media using a displacement discontinuity boundary element method. They noted that poroelastic effects may limit the rate of fracture growth, but growth may still accelerate. In their model, the growth rate of isolated NHF within many rock types is a function of the characteristic time.

$$\frac{Kt}{S^* a_o^2}, \tag{6.1}$$

where K is hydraulic conductivity, S^* is matrix storage, and a_o is fracture aperture. Characteristic time is dictated by the hydraulic conductivity; the conductivity determines how quickly fluid is transmitted to the fracture. Plots of the dimensionless growth rate (fracture length / time) of an isolated NHF for various values of the dimensionless parameter ϕ are presented in Figure 6.1. The ratio of the amount of water required to sustain propagation (i.e. the change in area of the fracture per unit extension) to the amount of fluid readily available (i.e. the matrix storage),

$$\phi = \frac{(1-\nu)\rho g}{\mu S^*}. \tag{6.2}$$

The ratio $\frac{(1-\nu)}{\mu}$ controls the change in area. As S^* increases, more fluid is available to flow into the fracture. Note that unlike induced hydraulic fractures, the fluid pressure within natural hydraulic fractures is less than the ambient fluid pressure after propagation begins.

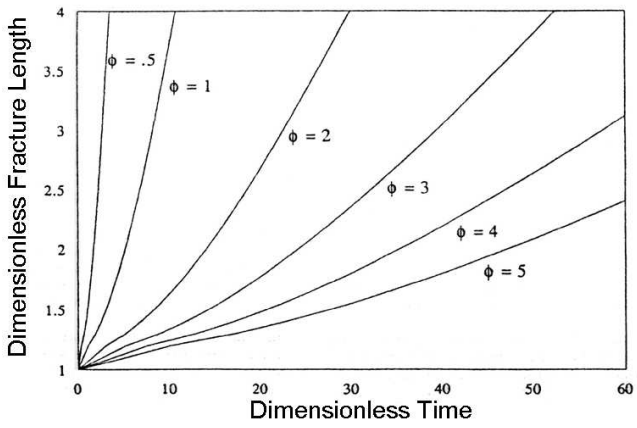

Figure 6.1: Plots of normalized fracture half-length (with respect to initial flaw length) versus dimensionless time show that rocks with higher ratios (ϕ) of amount of fluid required to sustain propagation (the change in area of the fracture per unit extension) to amount of fluid readily available (matrix storage) have fractures that grow slower. From *Renshaw and Harvey* [1994].

Recent literature has focused on the subject of induced hydraulic fracturing for enhanced geothermal and oil extraction. The propagation of fractures explicitly depends on the stress distribution around the fracture tip. Thus, many papers (e.g. *Rice and Cleary* [1976]; *Advani et al.* [1987]) address pore fluid pressure at the crack tip. In general, theoretical arguments underpredict the amount of pressure it takes to propagate an induced hydraulic fracture [*Advani et al.*, 1997]. A small region of reduced pressure at the tip of a propagating fracture can significantly reduce the stress intensity and require renewed abnormally high fluid pressure to propagate. This lower-pressure region, or the fluid lag region, is usually attributed to excessive fluid leak-off into the formation. This suggests that fluid flow into the fracture may be a limiting process in geologic fracture generation.

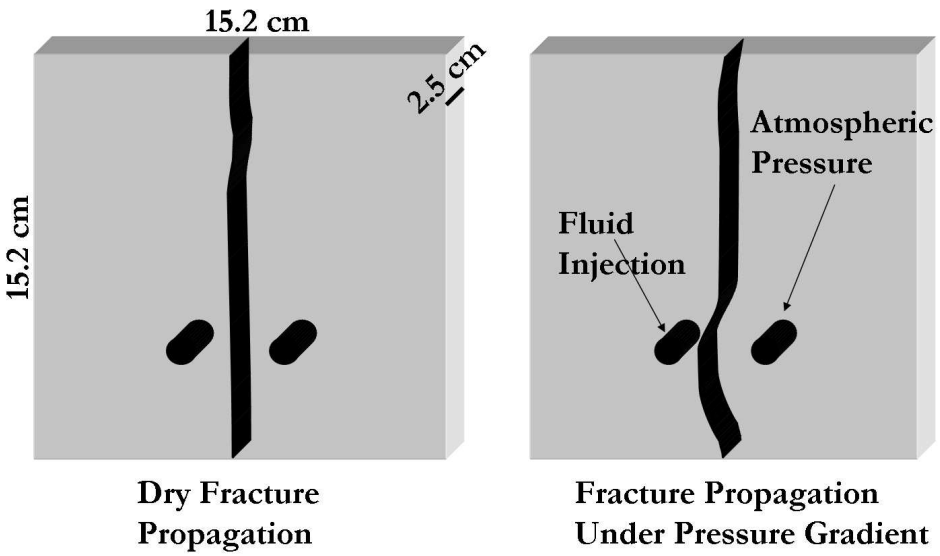

Figure 6.2: Deviation of fracture induced by pore pressure gradient. Adapted from *Bruno and Nakagawa* [1991].

Petroleum engineering studies suggest that hydraulic fracturing may be controlled by inducing local regions of high pore pressure via fluid injection. *Bruno and Nakagawa* [1991] showed that induced hydraulic fractures will propagate toward regions of higher local pore pressure, or lower effective stress (Figure 6.2). Higher injection pressures introduced greater deviation in fracture propagation direction. *Bruno and Nakagawa* [1991] found that stress concentrations at crack tips are locally influenced by pore pressure magnitude. *Berchenko and Detournay* [1997] used a numerical model to demonstrate that pore pressures can alter the propagation path of an induced hydraulic fracture.

The work presented in this paper is a logical extension of the above-described work. We take a different numerical and theoretical approach to the physics of the problem compared to *Renshaw and Harvey* [1994]. We use

a fully coupled discrete technique that simulates the full dynamics of porous media at the grain scale. This enables us to relax assumptions associated with porosity-permeability relationships and lets the porous media fully evolve with changes in boundary conditions. Fractures are modeled as breakage of bonds placed at boundaries between neighboring grains. No crack distribution inside the model is assumed; fractures initiate and propagate where dictated by the physics. Since fracture genesis (or damage) is modeled explicitly, feedback to both fluid flow and the mechanics of the simulated rock is also explicit. An additional advantage to using this numerical technique is its ability to carry out sensitivity analyses by holding key parameters constant (i.e. grain-size distribution), which is difficult to do in the laboratory. This is demonstrated with a sensitivity analysis of rock permeability on fracture behavior.

6.3 Theory of Natural Hydraulic Fracturing

Replicating the conditions under which NHFs are thought to form in sedimentary basins is difficult in the laboratory. *Secor* [1965] showed that if the fluid pressure was greater than the least minimum stress σ_3, the effective minimum stress σ_3^* became tensile. This can be shown through

$$\sigma_3^* = \sigma_3 - p. \tag{6.3}$$

If this relation is correct, than either a decrease in σ_3 or an increase in p is needed to fracture a rock. This relationship is widely used throughout geology and hydrogeology and is referred to as the hydraulic fracture criterion. The physics of this criterion are now examined.

6.3.1 Fluid Pressure and Confining Stresses

Consider a 2-D, box-shaped, fluid-filled, homogeneous and isotropic porous solid with negligible tensile strength, dimensions of infinite extent, and remote minimum far-field boundary conditions of σ_1^r on top and bottom and σ_3^r and the left and right. Also assume that the fluid is stationary (no pressure gradients) and is held at a pressure greater than σ_3^r. This meets the failure condition that described by *Secor* [1965]. Where are the net tensile stresses located? Stress is a tensor and has a magnitude as well as a directional component, whereas fluid pressure is a scalar with finite magnitude and acts in all directions uniformly. With the condition of constant fluid pressure, this implies that on all planes (normal to σ_3^r) internal to the fluid filled solid, fluid pressure magnitudes and their resulting forces on the solid framework (assuming 100% efficiency) act to cancel one another out. The only place a net tensile force exists is at the remote location where σ_3^r is applied. Note that this is also the location of the highest fluid pressure gradient in the system. In this case fractures would form at the boundary of σ_3^r. This is not intuitively obvious since *Secor* [1965]'s original condition is met everywhere internal to the solid. It is important to note that *Secor* [1965]'s condition neglects the confining effects of the fluid on the solid mechanics.

This concept may also be demonstrated by considering the local σ_3 in a commonly used set of conditions (e.g., [*Lorenz et al.*, 1991; *Engelder and Lacazette*, 1990; *Roberts and Nunn*, 1995; *Wang*, 2000; *Bessinger et al.*, 2003]) for a tectonically relaxed basin (one in which horizontal stress is only the result of vertical stress, or uniaxial strain conditions) with hydrostatic fluid pressure

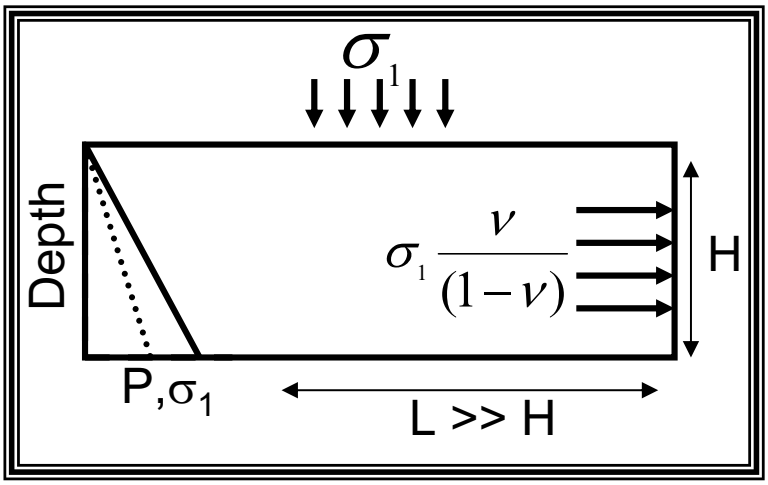

Figure 6.3: Schematic of commonly used conditions to evaluate the likelihood of natural fracturing in sedimentary basins. These conditions assume a very long basin relative to it's height with no applied confining stress and minimum stress only a result of the vertical load. On left hand side of the figure are the assumed pore pressure (dotted line) and stress (solid line) vs. depth curves. No horizontal flow is allowed.

during burial in a sedimentary basin (Figure 6.3). The constitutive equations (in terms of stress-strain and pore pressure) for uniaxial strain [*Wang*, 2000] are

$$\sigma_3 \mid_{\varepsilon_3=0} = \frac{2G\nu}{1-2\nu}\varepsilon_1 + \alpha p, \tag{6.4}$$

and

$$\sigma_1 \mid_{\varepsilon_3=0} = \frac{2G(1-\nu)}{1-2\nu}\varepsilon_1 + \alpha p, \tag{6.5}$$

where σ_1 is gravitational loading stress, G is shear modulus, ν is Poisson's ratio, and α is Biot-Willis coefficient. The Biot-Willis coefficient is a measure of the efficiency with which pore pressure counteracts confining pressure to produce volumetric strain. The coefficient is assumed to be equal to 1 as *Terzaghi*

[1925] first assumed. We can solve Equation (6.4) for ε_1 and substitute into Equation (6.5) to show that

$$\sigma_3 \mid_{\varepsilon_3=0} = \left[\frac{\nu}{(1-\nu} \left(\sigma_1 - \alpha p\right) \right] + \alpha p. \tag{6.6}$$

Simplifying the above equation produces

$$\sigma_3 \mid_{\varepsilon_3=0} = \frac{\nu}{(1-\nu)} \sigma_1 + \frac{1-2\nu}{(1-\nu)} \alpha p. \tag{6.7}$$

The uniaixal strain case predicts that σ_3 increases linearly with pore pressure, but it is a strong function of Poisson's ratio and the Biot-Willis parameter. The Biot-Willis parameter not only affects the amount of pressure added to the confining stress, but also influences the amount of offset of the effective stress. This is illustrated in Figure 6.4, a contour plot of effective stress as a function of pore fluid pressure and Biot-Willis parameter values. Four different values of Poisson's ratio are presented for a depth of 3 kilometers in a basin with a lithostatic gradient of $23 \frac{MPa}{km}$ and a hydrostatic gradient of $10 \frac{MPa}{km}$. Fluid pressure ranges between the hydrostatic and the lithostatic. If the tensile strength of the rock is neglected, the critical fluid pressure needed for fracturing is located where the effective stress is zero. For all four values of ν, this fluid pressure is identical. For a constant α, ν serves to change the magnitude of the effective stress. If a tensile strength greater than 0 is assumed, the critical fluid pressure will be different, as a function of ν. If the confining term in Equation (6.7) is neglected, much lower fluid pressure is needed for fracturing (Figure 6.5). At low values of ν, the critical fluid pressure is greater than the hydrostatic pressure.

These pertain to an idealized, tectonically relaxed basin with no horizontal fluid pressure gradients. If a finite horizontal force is externally applied,

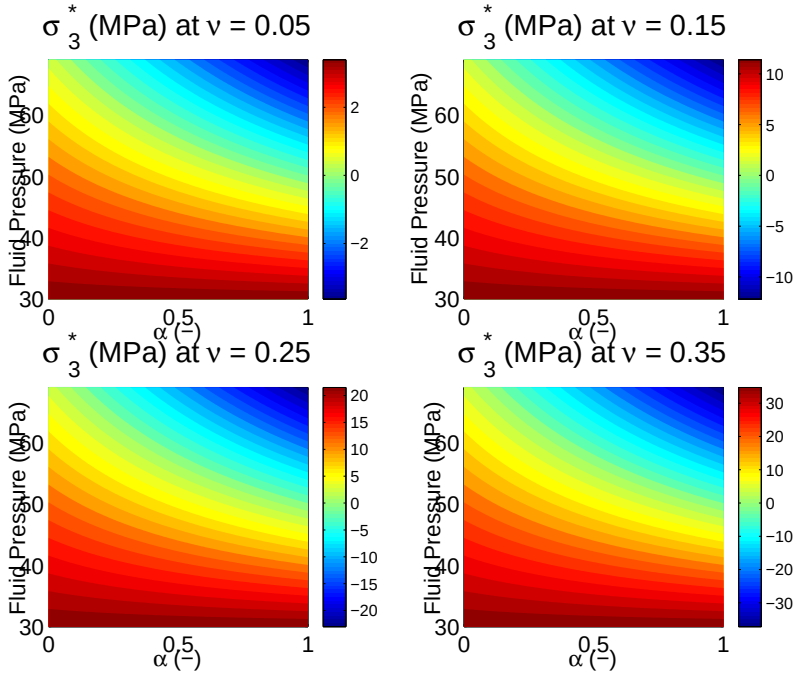

Figure 6.4: The least minimum stress (σ_3) in a tectonically relaxed basin is a strong function of σ_1 and fluid pressure. Poroelastic effects severely influence the resulting effective stress distribution (σ_3^*). This is shown for values of ν and α as a function of fluid pressure using Equation (6.7). Critical fluid pressure values, where effective stress = 0, are the same for all ν.

meaning that σ_3 is not a function of σ_1, the fluid pressure needed for fracturing is significantly higher. In the case of the box example presented at the beginning of this section, the σ_3^r is not a function of the σ_1^r and the boundary conditions used this analysis is not valid for the problem. For values of Poisson's ratio that are close to 0 and a Biot-Willis coefficient that is equal to 1, as in the 2-D box analysis, the effective stress will not go to 0 except at the boundaries. In situations where σ_3 is not a strong function of σ_1 or cases with large fluid pressure gradients, physical boundaries will strongly influence effective stress conditions and thus natural hydraulic fracturing. The presence of fluid pressure gradients will reduce the amount of confining stress added to Equation (6.7), because the assumption in the solution is that of spatially constant fluid pressure.

Nur and Byerlee [1971] concluded in their classic study that the effective stress law was valid. Their experimental setup consisted of a cylindrical rock specimen subjected to an axial load, with a circumferential confining fluid. Pore fluid in the rock was isolated from the confining fluid by a thin impermeable membrane. A series of tests performed with different pore pressure in the samples were analyzed with plots of volumetric strain vs. effective stress. Plots of volumetric strain versus effective stress for different internal pore pressures plotted along similar lines, suggesting that the effective stress law is valid. The boundary between the sample and the thin membrane played a significant role. For the case of a confining stress equal to a constant pore fluid pressure, the rock does not "feel" the boundary. Any increase in stress above static fluid pressure at the boundary is transferred to the rock. Therefore, even though no fluid flow takes place, a large gradient in pressure exists at the boundary. This

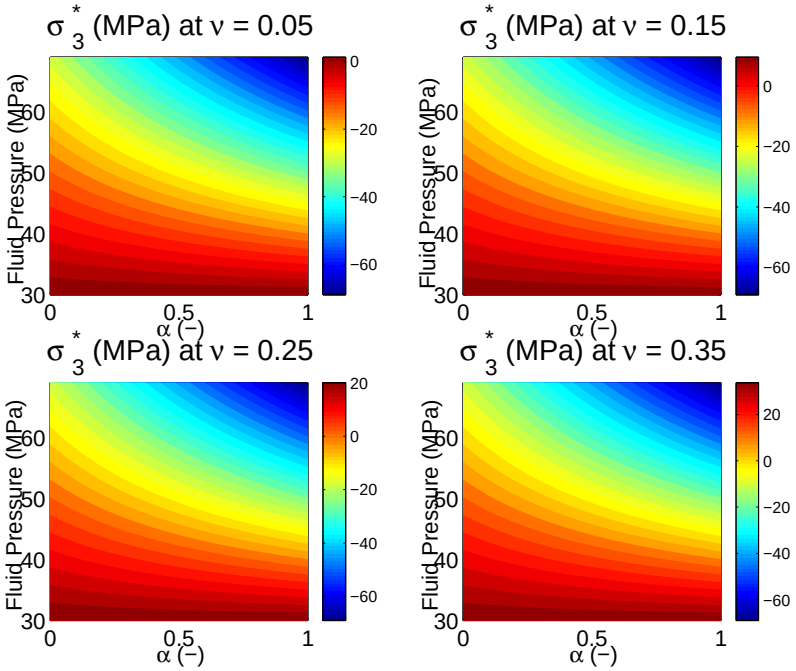

Figure 6.5: Plots illustrating the effect of fluid pressure on confining stress in a tectonically relaxed basin. Contours are results of solving Equation (6.7) neglecting the last term. This reduces the critical fluid pressure needed to drop effective stress (σ_3^*) to 0.

pressure gradient (or stress gradient) is responsible for the observed effective stress. It is the boundaries (or features that cause stress or pressure gradients) that are controlling the system behavior.

In induced hydraulic fracturing (IHF), boundaries also play an important role. IHFs are produced under conditions of elevated pressure in the flaw or well bore compared to the formation pore pressure. Under these conditions, hydraulic fractures are created because large pressure gradients between the well bore and the formation are present. The boundary or pressure difference between the well bore and the formation plays a critical role in the propagation of the fractures.

6.3.2 Fluid Pressure Gradients and Drag Forces

In saturated flow through a porous medium, force is exerted by the fluid on the solid particles (See Section 5.4.1). Following *Terzaghi* [1943], three forces act on the solid particles through which flow occurs. The first is the weight of the overlying solids $\mathbf{F_1}$ acting downward. This is given by

$$\mathbf{F_1} = -\gamma_\mathbf{s}(\mathbf{1} - \mathbf{n})\nabla \mathbf{z}, \tag{6.8}$$

where γ_s is the specific weight of the dry solid particles, n is the porosity, and ∇z is the gradient in elevation (parallel to the gravitational field). The second force is the buoyancy force $\mathbf{F_2}$, defined as

$$\mathbf{F_2} = -(\mathbf{1} - \mathbf{n})\nabla \mathbf{p}, \tag{6.9}$$

in terms of force per unit volume. The final force is the drag (or seepage) force $\mathbf{F_3}$ which, per unit volume of porous medium, is equal to

$$\mathbf{F_3} = -\mathbf{n}\gamma_\mathbf{f}\nabla\psi, \tag{6.10}$$

where γ_f is the fluid's specific weight, and $\nabla\psi$ is the fluid potential defined as

$$\nabla(z + \frac{p}{\gamma_f}). \tag{6.11}$$

The fluid potential is a measure of the available energy per unit weight of fluid and is dissipated as viscous friction at fluid-solid interfaces. As this energy is dissipated, a force is exerted on the solid matrix in the direction of fluid flow. The first two terms in Equation (6.10) can be attributed to properties of the porous medium in question. The porosity is obviously a property of the porous medium, but the potential gradient can also be attributed to the medium through the permeability. *Terzaghi* [1943] neglected any external applied forces, but these can easily be incorporated through force summation over a volume of porous media. The three forces can be summed and evaluated for conditions of piping (sand production) and quicksand (where $\mathbf{F_3} > \mathbf{F_1} + \mathbf{F_2}$) phenomena [*Bear*, 1972]. Note that if $\nabla p = 0$ (i.e. no flow) then $\mathbf{F_3} = \mathbf{F_2} = \mathbf{0}$. This implies that the static fluid pressure, P, is not a significant hydraulic fracture criterion if the Biot-Willis coefficient is equal to $1(\alpha = 1)$. The value of ∇p determines the stress state in the solid and may be a more effective criterion. Thus, it may be possible to define a critical gradient (similar to that for quicksand conditions [*Bear*, 1972]) for hydraulic fracturing, based on rock parameters. The two processes are similar in that both require effective stress to tend towards zero, although in quicksand problems the vertical stress is the

stress of importance. Parameters of importance in the hydraulic fracturing problem are the rock tensile strength and the Biot-Willis parameter.

In summary, fluid pressure gradients play a significant role in creating net tensile stresses in porous solids. Many different factors cause pore pressure gradients in rocks. These include transients caused by the spatial heterogeneity of the expulsion of connate water during compaction, in-situ sources of fluid pressure, and local gradients driving fluid flow. Spatial heterogeneity, at all scales, may play an important role in dictating where fractures nucleate. These issues are explored below through development of a new numerical test design and simulation.

6.4 Numerical Test Design

The conditions outlined in the above section are not simple to impose in a laboratory test. Dropping σ_3 while maintaining a condition of higher p is impossible in a standard cylindrical triaxial pressure cell. This is because these setups typically apply σ_3 with a loading piston axially attached to the endcaps of the sample. It is inevitable that when σ_3 is dropped lower than p, fluid will leak between the endcaps and the rock, creating an "extension fracture" between them. An alternative technique of applying a minimum stress would be through a confining pressure surrounding the long axis of the specimen, but when σ_3 is dropped lower than p, fluid will break the seal between the sample and the confining fluid. Without designing a new testing apparatus, dropping σ_3 and holding p constant is not possible. It is also apparent that a resulting increase in p while holding σ_3 constant suffers from the same problems as discussed above.

A new method to generate fluid-pressure-induced fractures was designed to overcome the limitations of imposing laboratory boundary conditions. The test, shown in Figure 6.6, is a combination of both end member cases discussed above. Initial conditions on the cylindrical sample of rock saturated with a fluid pressure P_o are typical of traditional triaxial tests with the exception that the $\overline{\sigma_3}$ is axial and σ_1 laterally confines the sample. At the start of the test, both P_o and $\overline{\sigma_3}$ are instantaneously lowered. These conditions will not cause leaking at the boundaries or through the sample jackets since (1) P is lower than σ_3 at the boundary and (2) P is lower than σ_1 everywhere. The drop in both stress and fluid pressure at the boundary will create conditions conducive to the generation of extension fractures in the sample. These conditions consist of fluid pressure at the center of the sample greater than the local axial stress which, assuming quasi-equilibrium with new boundary conditions, should be σ_3. As a result, extension fractures should form perpendicular to σ_3 in areas of high p and low σ_3. In NHFs, unlike induced hydraulic fractures, ambient fluid pressure is higher surrounding the fracture than inside the fracture itself. This condition imposes several constraints on how resulting fractures initiate and interact.

Differing time constants governing fluid flow and mechanical equilibrium are responsible for creating a condition of high p and low σ_3 at the sample center. Specifically, the fluid diffusion time constant is much lower (i.e. slower) than the mechanical equilibrium time constant. In porous media, the time it takes for a given fluid pressure to come to equilibrium with a change in boundary conditions is a function of the rock's hydraulic diffusivity. In groundwater hydrogeology studies, uniaxial strain and constant vertical stress are typically

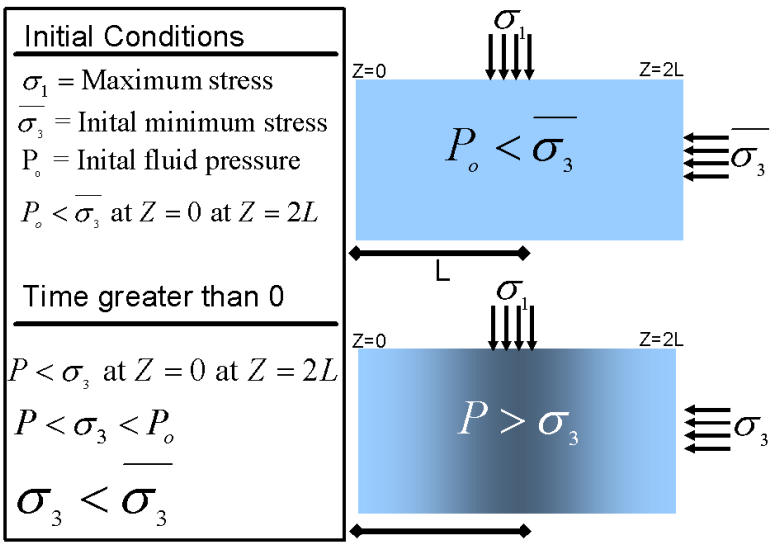

Figure 6.6: Initial and boundary conditions for experimental approach to generating natural hydraulic fractures. Fluid pressure in the system is kept elevated relative to the minimum stress by the lag time that occurs as a result of fluid flow (pressure gradients).

assumed, and hydraulic diffusivity (κ) is thus defined as

$$\kappa = \frac{k\rho g}{\mu S_s}, \tag{6.12}$$

where S_s is the one-dimensional specific storage, k is the intrinsic permeability, ρ is the fluid density, g is gravitational acceleration, and μ is fluid kinematic viscosity. Note that κ has mks units of $\frac{length^2}{time}$ - $m^2 s^{-1}$. A time of $\frac{L^2}{\kappa}$ is required for a pressure change to propagate a distance L. The diffusion time is function of the rocks hydrologic properties (k, S_s) and it relies on the fluid properties (ρ, μ). In this study, we will focus on the role that κ plays in the initiation and propagation of fractures using the experimental test designed above.

6.5 Modeling Approach

We analyzed hydraulic fracturing processes with a direct simulation method developed by *Cook et al.* [2000] and *Cook* [2001]. The approach couples the Discrete Element Method (DEM) for solid mechanics with the lattice Boltzman (LB) for fluid mechanics. Since the LB approximates the Navier-Stokes equations of fluid flow, no empirical relations are necessary to relate fluid flux to pressure drop at the pore scale (i.e. Darcy's law). Also, the DEM does not require *a priori* assumptions about the relationship between fluid permeability and porosity. The hydrodynamics develop with the evolving solid matrix. These techniques are briefly reviewed below.

6.5.1 Discrete Element Method

The DEM technique has been successfully used to approximate the behavior of non-cohesive, granular systems under low stress conditions [*Cundall*

et al., 1982] and lithified sedimentary rocks [*Bruno and Nelson*, 1991; *Potyondy et al.*, 1996; *Hazzard et al.*, 2000; *Boutt and McPherson*, 2002]. In this paper we are employing an existing two-dimensional DEM application [*Rege*, 1996]. DEM simulates the mechanical behavior of porous media by idealizing the system as a collection of separate particles that interact at their contact points. The method consists of (1) identifying elements in contact and (2) resolving the contact physics. The calculations performed in the DEM alternate between the application of Newton's Second Law and a force-displacement law (simple contact models) at the contacts between particles. The force-displacement law relates components of force to the corresponding components of the relative displacements through a generalized contact constitutive model. The contact constitutive model has two parts, a stiffness model and a slip model. The motion equations are integrated explicitly with respect to time to obtain particle positions, then used in the force-displacement calculations, and the calculation cycle starts over again. A advantage of this approach is that the DEM constitutive behaviors (stress and strain relations) are results rather than assumptions.

6.5.2 Lattice-Boltzmann and Coupled Model Theory

Fluid coupling with DEM was developed by *Cook* [2001] and *Cook et al.* [in press] through the integration of LB with the DEM framework described above. A detailed development and validation of the coupled method can be found in *Cook et al.* [2000], *Cook* [2001], and *Cook et al.* [in press]. The two-dimensional simulations reported by *Cook* [2001] include such complex phenomena as drafting-kissing-tumbling in multi-particle sedimentation simulations and the saltation phase of bed erosion. An extended description of

the method was presented in Chapter 5.

6.6 LBDEM Conceptual Model

Unlike continuum formulations, discrete models require significant up-front effort to build a model domain. The first step in the LBDEM is to develop a mechanical model out of discrete elements. Models used in this study were built using a space-filling algorithm that packs the discrete elements into a rectangular space (see (Chapter 2). Roughly 1000 ellipse-shaped elements with an aspect ratio of 0.5 were packed into a 7 cm long by 3.5 cm wide box (Figure 6.7). Ellipse-shaped elements were chosen for their superior frictional and mechanical properties compared to circular elements. Similar to a laboratory test, boundary conditions are applied to the discrete element assembly with platens (rectangular discrete elements) until a specified stress is reached.

To simulate the behavior of a cohesive rock, individual discrete elements were bonded to one another. Bonds are modeled as point-to-point constraints between neighboring particles using the spring formulation as

$$F_b = k_b \Delta x, \tag{6.13}$$

where F_b is the force in the bond, k_b is bond stiffness, and Δx is relative displacement of the neighboring particles. Bonds are aligned with the surface normals and connect the closest surfaces of the two particles of interest. If F_b is greater than or equal to the bond strength F_b^{crit} the constraint is removed and bonded elements are allowed to move freely. A limitation of this bonding approach is that it has no implicit shear strength. In reality, the bond has some finite shear strength since it is modeled as a surface-to-surface contact,

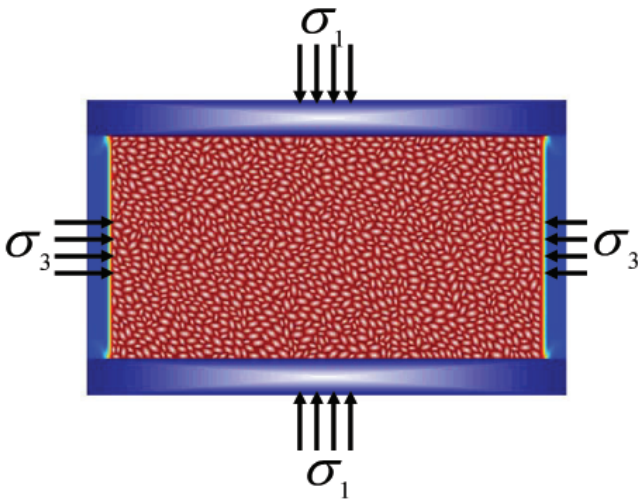

Figure 6.7: Base discrete element model for all fracture simulations. Roughly 1,000 ellipse-shaped elements were packed into a 7 by 3.5 cm area.

and any offset (normal or tangential) great enough to exceed the F_b^{crit} will cause the bond to fail. Another limitation of the bonding scheme is that it has no interaction with the flowing fluid. Properties of the discrete element portion of the simulations are listed in Table 6.1.

The simulated LB fluid has a dynamic viscosity of $0.2\frac{cm^2}{s}$, similar to that of water (Table 6.2). Each simulation consisted of approximately 500,000 fluid nodes. The fluid lattice, shown as the colored area in Figure 6.7, extends beyond the edge of the discrete elements to allow straining of the element assembly during fracturing. The sample in Figure 6.7 was tested under a constant fluid pressure drop and the resulting steady-state discharge through the system recorded. Resulting permeability of the model specimen was $1.3 * 10^{-4} cm^2$ or $1.3 * 10^{-8} m^2$, a high value relative to cemented rocks ($10^{-9} - 10^{-19}$). This is attributed to the model being only 2-D. Specific properties of the fluid

Table 6.1: Parameters of Solid Assembly

Parameter	Value
Friction (-)	0.5
Element Normal Stiffness (Dyne/cm)	$1 * 10^5$
Element Shear Stiffness (Dyne/cm)	$6 * 10^5$
Element Size Range (cm)	0.11-0.07
Bond Strength, F^{crit_b} (Dyne)	700
Bond Stiffness, k_b (Dyne/cm)	$1 * 10^5$

Table 6.2: Parameters of Fluid Lattice

Parameter	Value
Viscosity ($\frac{cm^2}{s}$)	0.2
Relaxation Time (-)	0.625
Node Spacing (cm)	0.009
Fluid Radius (-)	0.6
Timestep (s)	$1e-5$

lattice are given in Table 6.2.

The initial conditions described above for the fracturing test applied to the LBDEM model are shown in Figure 6.7. Initially the sample is loaded hydrostatically to an effective stress of $50\frac{dynes}{cm^2}$ (500 kPa), then the effective axial stress (sample short axis) is dropped to $40\frac{dynes}{cm^2}$ while holding the lateral stress constant. The lateral (sample long axis) stress is maintained via platens while the axial stress is applied through the discrete elements along the boundary of the model. This allows both the application of a stress and movement of fluid through the boundary. The initial fluid pressure within the sample is constant. The bond strength of the elements is 700 dynes for all models. This value is

reasonable when compared to the initial fluid pressure drop across the sample, $1.7\frac{dynes}{cm^2}$. In relative terms, the bond strength is akin to a tensile strength of 7 MPa for a fluid pressure drop of $\sim$ 17 MPa across the sample.

The test begins with a drop in both the axial stress and fluid pressure at the boundaries. For all tests, the axial stress is dropped to $0.1\frac{dynes}{cm^2}$ and the fluid pressure difference $(P_o - P)$ is $1.7\frac{dynes}{cm^2}$. Fluid pressure and fluid velocity were monitored along a cross-section parallel to the long axis of the model specimen. In addition, screenshots of the model were taken at 0.001 second intervals.

6.7 Fluid-Induced Fracture Results

The model (Figure 6.7) was executed under the conditions described above for 2 seconds of model time, about the time required for the system to come to a new equilibrium state. Snapshots of model state are presented in Figure 6.8 for early through late time model behavior. As the axial stress is dropped on both boundaries, forces between individual elements are lowered, resulting in an overall extensional strain in the elastic framework. The additional fluid pressure drop on the boundaries causes large pressure gradients toward the ends of the discrete element assembly. The overall pressure gradient is sufficiently high to cause breakage of the element bonds. These individual bond breakages coalesce into larger macroscopic features that split the assembly parallel to the maximum stress direction. Figure 6.9 highlights these fractures, emphasizing element speeds, and illustrating that individual blocks within the assembly are moving as coherent groups.

Test runs of dry models with identical boundary and initial conditions were performed with no resulting fractures but with less than 1% axial strain. Saturated models with no fluid pressure drop on the boundaries, but with a drop in the axial stress, also did not form fractures.

The fracture growth results in Figure 6.8 demonstrate that bond breakages are initiated closer to the boundaries before the central fractures form. Although this may be counterintuitive, fast wave speeds through the discrete element assembly cause elements near the boundaries to relieve force first, and the fluid pressure gradients then cause bond breakages. These bond breakages rarely coalesce into the larger macroscopic fractures seen in the center of the assembly. This is probably because pressure gradients near the boundaries drop faster than those in the middle of the model (see Figure 6.13a).

The orientations of both the large through-going fractures and smaller fractures are roughly perpendicular to the minimum stress direction. This result is consistent with predictions from a Mohr circle analysis. Slight deviations in fracture orientation are local in nature and represent preferential breakage of weak bonds around stronger bonds. In appears that the preferential path of a given fracture is through areas where elements are oriented with their long axis normal (broadside) to the overall fluid pressure gradient direction. One proposed mechanism for this is because such elements have more surface area exposed to prevailing fluid pressure gradients, resulting in larger net forces on the elements (Figure 6.10). Disc-shaped elements will not exhibit this phenomenon. It is also possible that mechanical anisotropy could be causing this phenomena. Additional tests using different packing geometries could discern

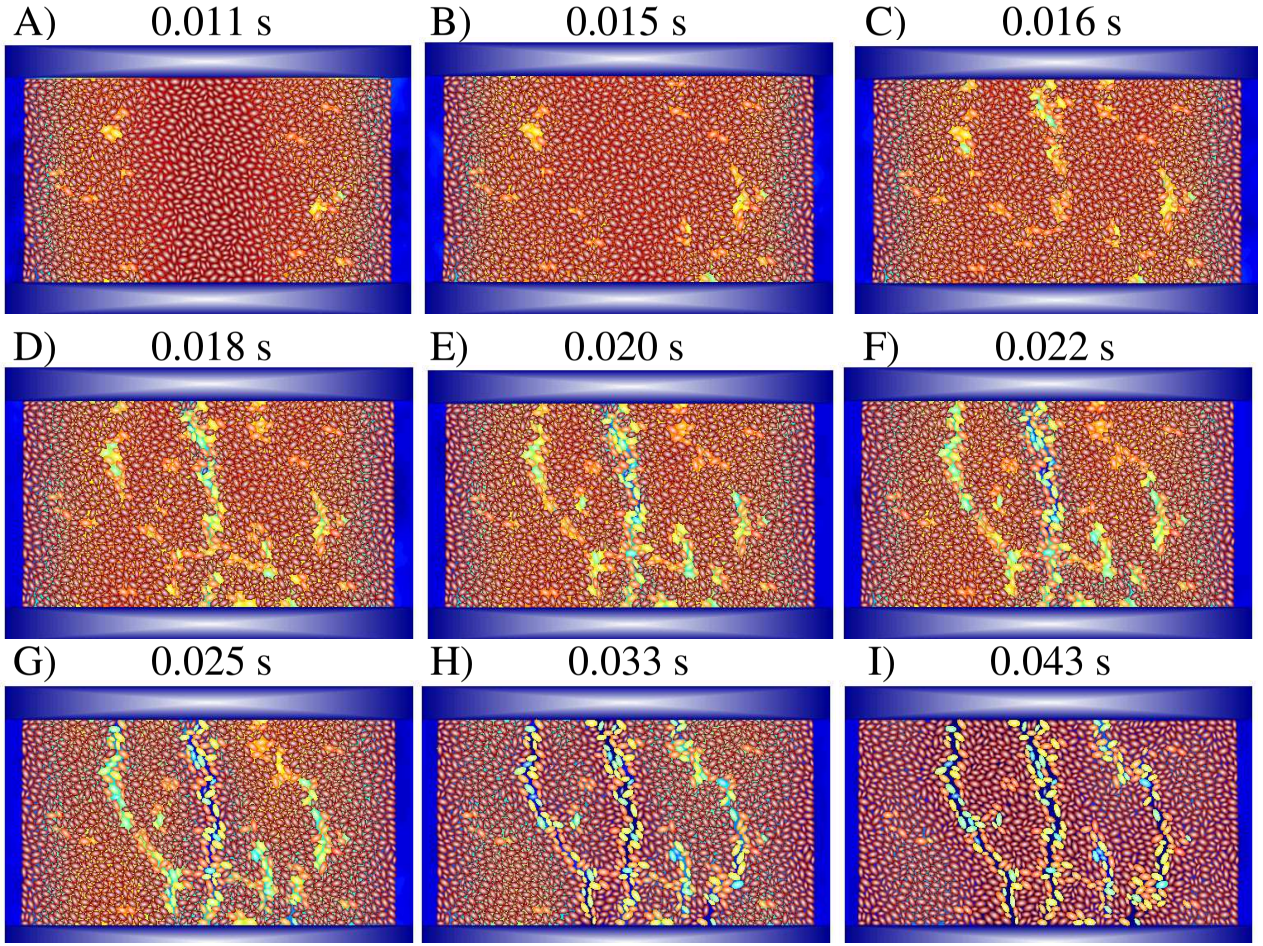

Figure 6.8: Time series of fracture initiation and propagation under realistic laboratory boundary conditions show a complex evolution of the model. In this and all models presented in this section, element color is % bonds broken and color shading behind elements is fluid pressure.

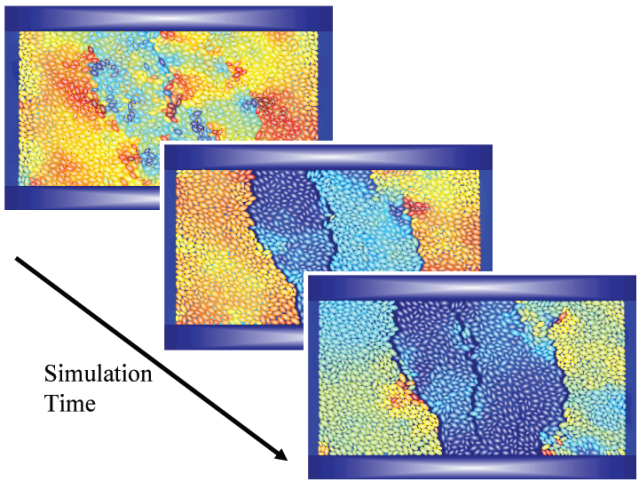

Figure 6.9: Time series of particle speeds (hot element colors indicate higher speed) illustrating fracture development as the simulation progresses. Outer blocks are moving at higher rates than inner blocks.

between the two hypotheses. The effect of anisotropy in element packing on resulting fracture orientations has not yet been studied in detail but the orientation used in these simulations does affect the orientation of fractures.

6.7.1 Fracture Initiation

One important physical fracture process that the LBDEM technique can capture is fracture initiation. Continuum-based formulations require assumptions about initial crack or fracture length that limit model applicability or generality. The LBDEM method's smallest length scale (element size) has a first-order control on initial fracture length. The relative location and orientation of the elements also controls where the fractures are located (i.e., fracture spacing less than element size is not possible). Most extension fractures form along grain boundaries [*Kranz*, 1983]. Thus, if the element size is assumed to

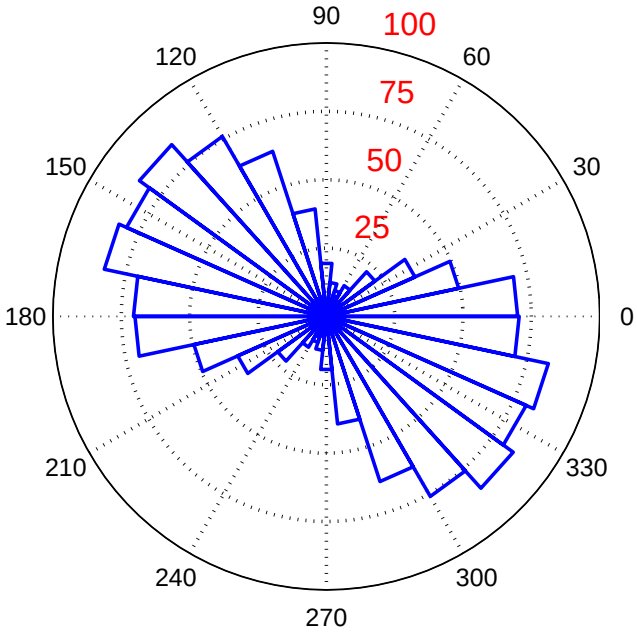

Figure 6.10: Element long axes are plotted in a rose diagram to visualize trends. The numbers correspond to the quantity of elements with the indicated orientation This preferred orientation of elements is coincident with the orientation of some of the major fractures in the model.

be equivalent to the grain size, this assumption is appropriate.

Fluid pressure gradients develop as a result of low pressure at the boundaries and higher pressure within the system. The gradients induce inter-particle stresses sufficient to break bonds. Figure 6.11 focuses on a particle pair central to the model in Figure 6.7. Pre- and post-bond breakage plots are shown together with a contour plot of the fluid velocity field. These particles are being forced apart through bulk loading of fluid on the assembly. The velocity magnitudes in the pre-bond breakage plot of Figure 6.11 reveal a low velocity zone in the vicinity of the impending bond breakage. After the bond is broken, fluid adjacent to the particles is influenced by the particle movement. The velocity vectors in the high pressure zones on either side of the bond point in opposite directions, causing a bulk loading in the assembly, which pulls apart the two particles. Velocity vectors beneath the particles indicate an extensional failure of the bond.

6.7.2 Fracture Propagation

Propagation or growth of fractures in the LBDEM is more explicit than in an equivalent continuum model. No remeshing or damage parameters are introduced to simulate a growing fracture. Fractures are visualized as the grouping of bond breakages. An advantage to this method is that when fractures form, no modification to the fluid lattice needs to occur to handle the change in local permeability.

After initial bond breakage, fluid pressure drops in the newly opened fracture and causes positive fluid-pressure gradients toward the fracture (Fig-

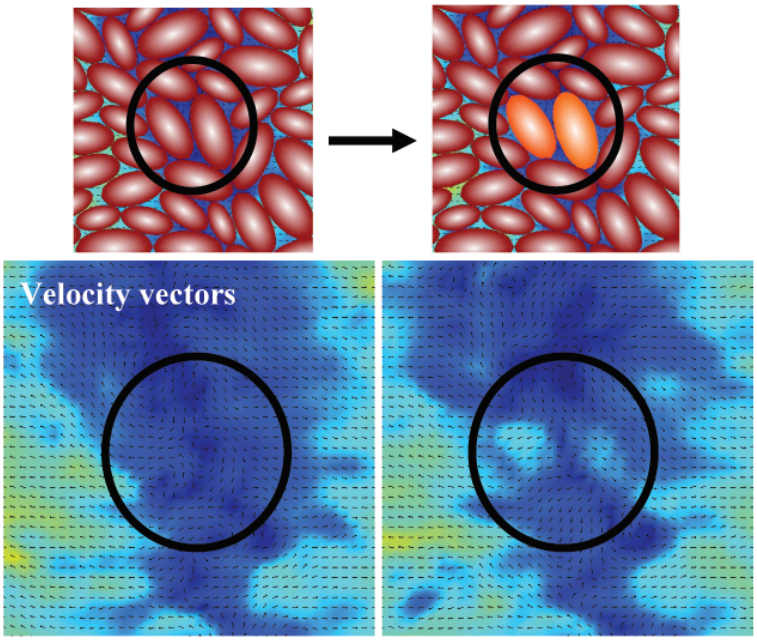

Figure 6.11: Pre- and post-bond (shaded particles) breakage is illustrated (top images) for a pair of particles in the central portion of the assembly. In the bottom images velocity magnitudes (dark shading is low velocity) and velocity vectors indicate a bulk extensional loading on the assembly. The bottom images are of the same region indicated in the top image, but blown up to show vectors more cleary.

ure 6.8). Despite this local forcing (Figure 6.12), macro-scale fluid pressure gradients are large enough to cause the particles to move apart. The plot in Figure 6.12 indicates that local fluid forces are not high enough to cause the bond breakage. This suggests that local-scale pressure gradients are not important in fracture propagation at the macro-scale. As the simulation progresses, the fractures are pulled further apart until the system returns to equilibrium. A small oscillation between fracture opening and closing in the system was observed as system energy was attenuated.

6.8 Role of Rock Permeability

In this section the role of rock permeability in fracture generation is explored. Three additional models with initial permeabilities varying over 2 orders of magnitude were executed under identical initial and boundary conditions as for the 1st simulation. Model permeabilities were modified by varying the discrete element's fluid radius. Changing the fluid radius does not change the solid (DEM) porosity, but it does change the amount of space available for fluid. By changing the "fluid-porosity" of the sample, the amount of sample storage changes slightly. Table 6.3 lists the properties of the models used for the permeability sensitivity study. Permeabilities of the samples were calculated using Darcy's law with a steady-state, constant pressure drop. Storage of the samples is evaluated using a transient technique described in Chapter 5. Even though permeabilities of the samples vary by more than 2 orders of magnitude, storage of the samples shows less variance. Hydraulic diffusivities of the samples vary no more than one order of magnitude. The time constants for the samples are correspondingly different by an order of magnitude. Run

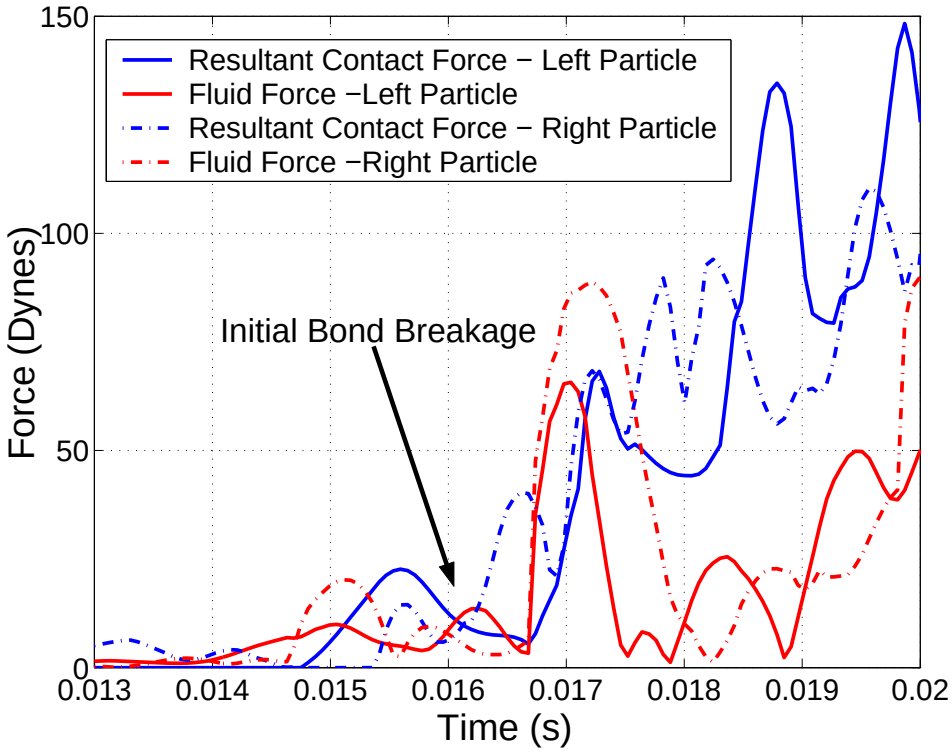

Figure 6.12: Contact forces and fluid-induced forces for two particles central to the model (See Figure 6.11) are shown here. After initial bond breakage, local fluid pressure in the fracture is lower, giving rise to fluid pressure gradients that are towards the fracture. Fluid loading on the assembly appears to be responsible for further fracture propagation.

Table 6.3: Properties of models used for permeability sensitivity study

ID	LB Radius	Porosity (%)	Permeability (cm^2)	Diffusivity ($cm^2 s^{-1}$)	Storage (cm^{-1})	Time Constant (s)
1	0.6	62.6	1.2E-4	23.5	0.027	0.41
2	0.725	49.3	7E-5	15.5	0.009	0.62
3	0.8	40.4	2.39E-5	5.4	0.0067	1.78
4	0.95	19.5	1E-6	1.9	0.0027	5.06

times to reach mechanical equilibrium in the assemblies were different because of different sample diffusivities.

Results of the four models with varying hydraulic diffusivities are presented in Figure 6.13 and Figure 6.14. The top model in Figure 6.13 is the base model described above. The additional three models are positioned in the order of decreasing permeability. Two main features of the base model are important (Figure 6.13, top). The first is the time delay in the response of the fluid pressure as a function of distance from the pressure boundary condition. This time delay is directly related to the hydrologic properties of the models. The slight change from a deep red hue to a more cherry red is a poroelastic pressure drop associated with reduced stress on the boundary. In this model, most of the fluid pressure has decayed to the boundary condition pressure by 0.2 seconds of time. This delay is important with respect to fracture propagation and initiation.

The second important feature of the base model includes the location and timing of fluid pressure drops with distance. These pressure drops correlate with the location of hydraulic fractures forming throughout the model. As pre-

viously described, the fluid pressure within the fractures drops as the fracture is formed. Local gradients surrounding the fracture are pointing inward acting to hinder fracture propagation. A high velocity zone that can be attributed to fluid flowing into a newly opened fracture is evident at later time in the fluid speed plot.

Fracture patterns and damage at 0.2 seconds are different for the 4 models. The most obvious difference is in the apertures of the fractures. The highest permeability model had the largest apertures, while the lowest permeability model had the smallest. The number of fractures (or number of bond breakages) in the model increases as a function of hydraulic diffusivity. This is in agreement with the fact that as the diffusivity decreases, fluid pressure within the pore spaces is higher for a longer duration, providing more opportunity for fracture growth. The highest permeability model has very localized deformation completely surrounding the main hydraulic fractures. As the hydraulic diffusivity of the model is decreased, deformation becomes less localized. Fracture propagation was faster in the higher permeability than in the lower permeability models.

Similar observations of fluid pressure and speed plots can be made in the lower permeability models of Figure 6.13 and Figure 6.14. Differences between lower and higher permeability models are due to the fact that high pressure resides longer in the lower permeability models. This result is intuitive from time constant calculations. Timing of fluid pressure drops is consistent in all models. The locations of these drops are different, and may be attributed to the location of the fractures that develop. Another interesting aspect is

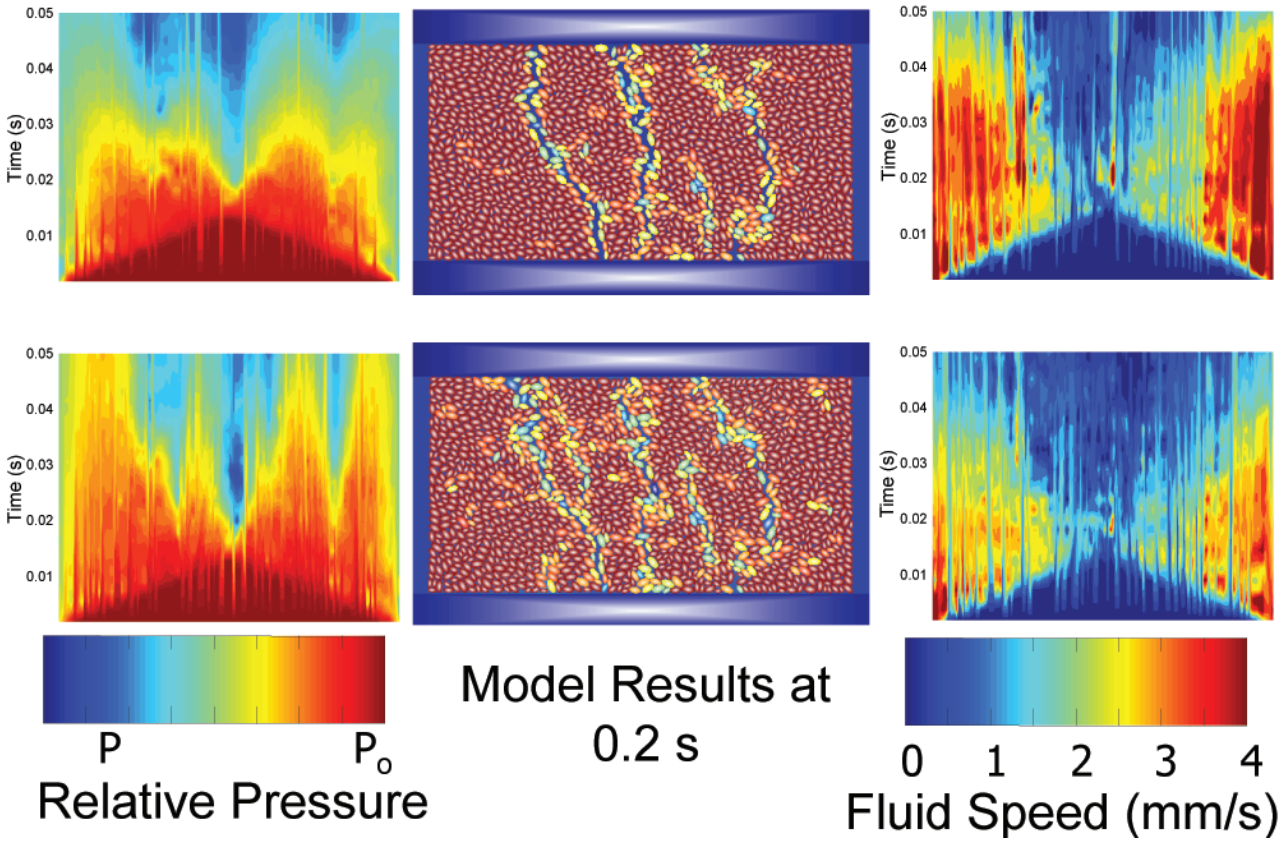

Figure 6.13: Results of fracturing simulations for $k = 1.2E-4cm^2$ (top) and $k = 7E-5cm^2$ (bottom) permeability models. Contoured fluid pressure results are also plotted on axes of time vs. distance for a stationary line along the center of the each model domain. In the center of each figure is a screenshot of the model state at 0.2 s. To the right of the screenshots is a filled contoured plot of fluid speed on axes of time vs. distance along the same centerline. All plots are scaled to the same ranges in order to compare differences between models.

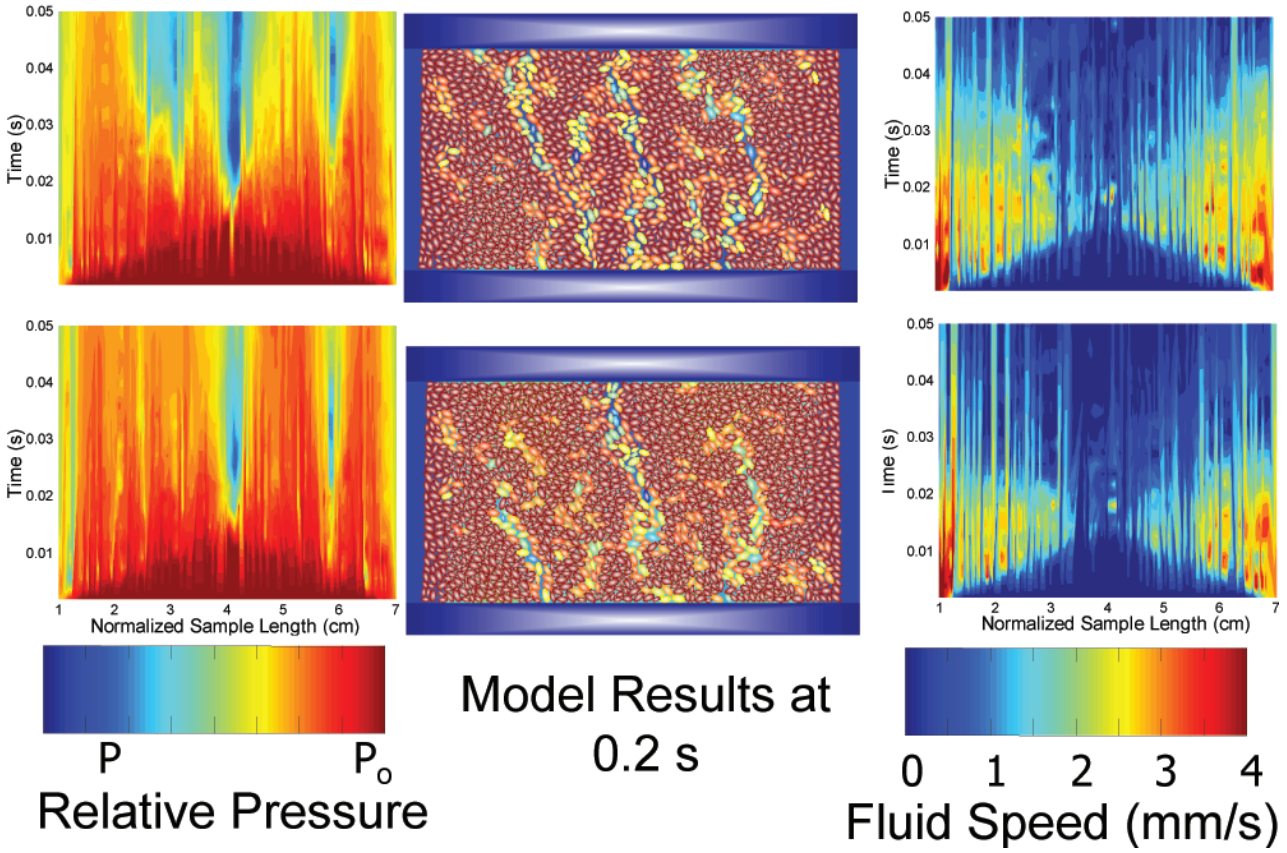

Figure 6.14: Results of fracturing simulations for $k = 2.39E-5cm^2$ (top) and $k = 1E-6cm^2$ (bottom) permeability models. In the center of each figure is a screenshot of the model state at 0.2 s. Contoured fluid pressure results are also plotted on axes of time vs. distance for a stationary line along the center of the each model domain. To the right of the screenshots is a filled contoured plot of fluid speed on axes of time vs. distance along the same centerline. All plots are scaled to the same ranges in order to compare differences between models.

that although the magnitude of fluid speeds at early times are similar in the high permeability and lowest permeability model, the later time magnitudes are strikingly different. This attribute, which is tied to fracture development, reflects differences in permeabilities of the models.

Fluid forcing on the solid framework plays a major part in the generation of these fractures. In Section 6.3.2, the force of fluid on the solid was shown to be proportional to the porosity of the rock and the fluid pressure gradient. In the permeability sensitivity study, the fluid pressure drop across the sample was constant. This implies that the initial fluid pressure gradient in the system was the same for each model. Assuming this, the porosity differences between the models (see Table 6.3) should indicate the relative force applied to the solids. The highest porosity model (also highest permeability) has 3 times more fluid force applied to the solid framework than the lowest porosity model. These differences in applied forces result in a difference in fracture generation and distribution, resulting in 3 distinct macroscopic fractures and little other deformation in the high porosity to the low porosity model (Figure 6.15). The low porosity model has fewer macroscopic fractures and more evenly distributed deformation.

The overall pressure gradients are the same amoung the models, but the pressure gradients at the multiple grain scale are different. This is a function of pore throat size, which varies from the high permeability model to the low permeability model. Figure 6.13 and Figure 6.14 show that the internal pressure gradients throughout the low permeability models were much higher than the high permeability models. I contend that these "local" gradients are responsible

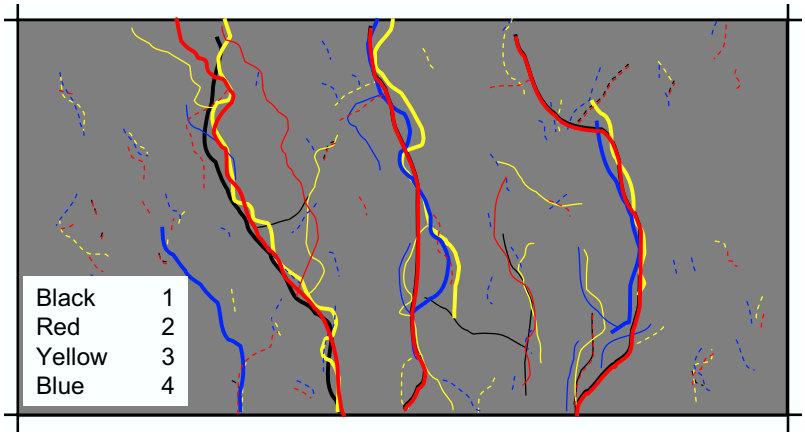

Figure 6.15: Interpretation of fractures for the permeability sensitivity study. Colors correspond to models with different permeabilities, 1 the highest and 4 the lowest. The thickest solid lines indicate large open fractures, whereas thin solid and dashed lines indicate smaller and minor fractures respectively.

for the more distributed deformation in the lower permeability models. This is explored in the next section through the imposition of hydrologic heterogeneity in the models.

6.8.1 Hydrologic Heterogeneity

Six additional numerical models of fracture genesis were developed to explore the competing roles of hydrologic heterogeneity, defined here as variations in pore throat size (which is related to fluid permeability), and mechanical properties. Two cases were examined, one in which pore throat sizes is increased (from a LB radius of $0.95 \rightarrow 0.6$, which effectively decreases element size) relative to the surrounding matrix and the other where pore throat sizes is decreased (from a LB radius of $0.6 \rightarrow 0.95$) relative to the matrix. Each one of the cases was performed with a vertical, a positively angled, and a negatively

angled heterogeneity. The locations of these heterogeneities are presented in Figure 6.16 as black lines. The vertical case contains a heterogeneity oriented perpendicular to the overall fluid pressure gradient. The negatively angled heterogeneity is parallel to the orientation of the major mechanical anisotropy (ellipse long axes) and the positively angled heterogeneity is tilted in the opposite direction. These heterogeneities mimic the planer features (such as bedding) commonly found in sedimentary rocks. The insertion of these variations introduces an anisotropy in the system. These results could be interpreted within the context of having both heterogeniety and anisotropy.

The simulations in which pore throat size is increased relative to the matrix (Figure 6.16) demonstrates a dramatic impact of permeability variations on damage and fracture orientation. Vertical and negatively angled heterogeneities appear to aid in the generation of fractures compared to the homogeneous case. These models exhibit a significant increase in damage and fractures. Fractures are most abundant in the simulations with vertical heterogeneity. The fractures are sub-parallel to the heterogeneities and nucleate at the boundaries between changes in pore throat size. The overall fluid pressure gradient in the system is parallel to these features, possibly maximizing their effect. Fractures in the negatively angled case are less abundant than the vertical case but also appear to be influenced by the spatial distribution of heterogeneity. The mean axis of the ellipses used in the numerical models is (qualitatively) coincident with the negatively angled heterogeneity. This relationship seems to aid the generation of fractures in the negatively angled case, since the major mechanical and hydrologic heterogeneities are aligned. The positively angled heterogeneities model contains only one large fracture

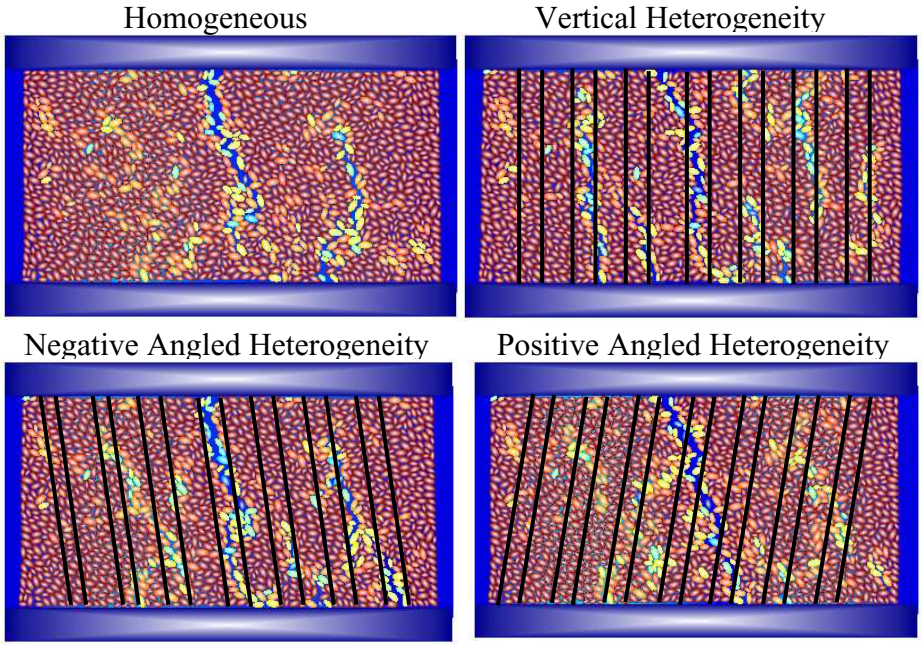

Figure 6.16: Results from increasing the pore throat size relative to the matrix. Black lines indicate the location of changes in pore throat size, where from left to right the lines enclose the changes. Models with imposed heterogeneities have similar porosities. Large differences between the "homogeneous" and heterogeneous models are evident. See text for further discussion.

and a similar amount of minor damage. This model includes the only fracture that cuts across multiple bands of permeability heterogeneity, indicating the heterogeneity is a weak control on the fracture formation. Lack of coincidence between the major mechanical control and the hydrological variation seems to be important in this case.

Figure 6.17 presents the results for simulations in which heterogeneities are represented by decreases in pore throat sizes relative to the matrix. The imposed vertical and steeply dipping heterogeneities have little effect on the fractures produced in these models. A minor amount of bond breakage is observed in the higher gradient (smaller pore throat) regions. Local deviations of the fractures in the vertical and negatively angled models, although minor, are coincident with the imposed heterogeneities. Consistent with this result is the observation that the homogeneous model fractures propagate more cleanly, with less bond breakages. This is similar to observations in the increased pore throat models. Overall, the reduction in size of pore throats in an overall high permeability matrix slightly increases the amount of resulting damage. This is in contrast to the increased pore throat size case, where significant differences between the homogeneous case and the heterogeneous case are observed.

6.9 Experimental Demonstration of Numerical Simulations

The design presented in Section 6.4 was implemented experimentally to provide a proof of concept of the technique. The exact conditions of Figure 6.6 were performed on cylindrical samples of rock in the Sandia National Laboratories Rock Mechanics laboratory. A cemented fine-grained channel sand was collected from the Abo Formation, where it outcrops east of Socorro,

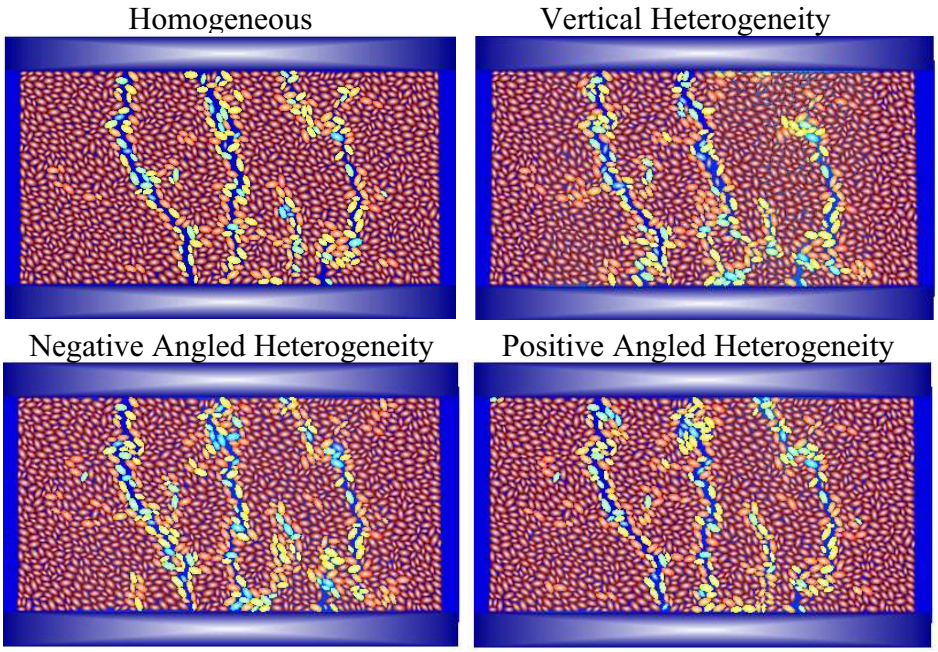

Figure 6.17: Results from decreasing the pore throat size relative to the matrix. Models with imposed heterogeneity have similar porosities. Very small differences in fracture patterns between the models are observed. See text for further discussion.

New Mexico, USA. The Abo Formation includes a variety of generally low permeability clastic sediments, ranging from mudstone to sandstone. The sample was chosen for this suite of tests because of its low permeability, lack of slaty cleavage, and clastic origin. A core of this sample was made, with the long axis of the core oriented at a high angle to bedding. The first test on this sample was successful, with one large mesoscopic fracture and many small fractures visible in thin section. The mesoscopic fracture formed parallel to bedding.

6.9.1 Sample Characteristics

The sample taken from the Abo Formation has a permeability (normal to bedding) of $10^{-13} cm^2$ as calculated by a steady state flow test. This permeability and assumed low storage (given a porosity of 12%) makes the sample an ideal rock for this test. The tensile strength of the sample was measured at 8 MPa using a standard brazil test with a 2.54 cm diameter sample. As discussed throughout this dissertation, the time required for fluid pressure to come to equilibrium with a change in boundary conditions is related to the sample permeability and storage. For the conditions of this test, the longer the time for the fluid to come to equilibrium the more likely the fracture will sample. This is because the time needed to change boundary conditions in the laboratory is finite. A plot of the time for pressure equilibrium vs. rock permeability can give an estimate on the lower limit at which the change in stress must take place. This is depicted in Figure 6.18 for fluids with 4 different viscosities. As the viscosity is increased, so does the reaction time of the fluid to the change in boundary conditions. The solid line placed at 1 second is the assumed reaction time of the laboratory equipment. For the lowermost viscosity

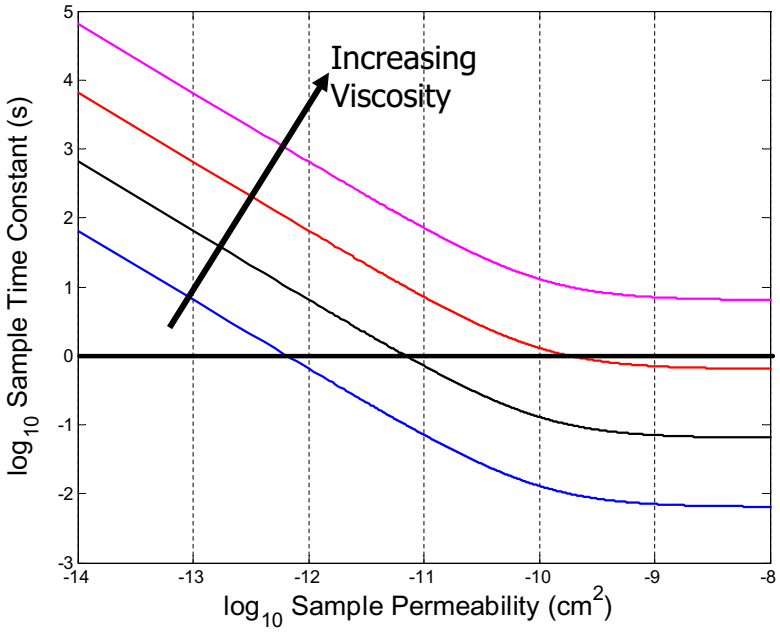

Figure 6.18: A log-log plot of sample time constants and fluid permeability defines the lower limit in which the stress on the rock can be removed. Four curves are shown here, each for a unique fluid viscosity. The lowermost curve is for that of water and the upper curves are for a viscosity of 10x, 100x, and 1000x of water. The solid line at 1 second is the assumed response time of the laboratory equipment.

curve (viscosity of water) any rock with a permeability greater than $10^{-12} cm^2$ will have a fluid pressure reaction time greater than that of the machine. The Abo sandstone is well above this value. The time constant of the sample, with a pore fluid viscosity 50 times that of water, is roughly 200 seconds.

6.9.2 Experimental Setup

The experimental design introduced in Section 6.4 relied on the confining pressure to be the maximum principal stress. This requires a special experimental setup that allows for such a differential stress. The rock mechanics lab at Sandia National Laboratories (SNL) has these facilities. All tests described in this section were performed at the rock mechanics lab at SNL by technician Bob Hardy. The endcaps, shown in Figure 6.19, were designed to allow significant axial extension while restricting the confining fluid to infiltrate the sample. The specimen was first jacketed with polyolefin heat shrink tubing and then coated with a polyurethane epoxy to the sample endcaps. The sample was also equipped for measuring axial and lateral displacements via LVDT (linear variable differential transducers). Two LVDTs were placed along the long axis of the sample to measure axial displacements and a circumferential split ring enables an additional LVDT to measure circumferential displacements.

The sample (with end cap assembly) was loaded into the pressure vessel and the 220 KIP load frame (Figure 6.20). The sample was loaded hydrostatically to 20 MPa and the axial load was dropped to 18 MPa. For each test, a dry run was executed where the sample was loaded hydrostatically and the axial load dropped to 0 MPa. This was done to determine if the amount of differential stress, 20 MPa, was great enough to induce a fracture. A silicone-based pore fluid (Dow 250 - 50 centistokes) was pumped into the bottom of the sample while maintaining a 10 MPa pressure drop until breakthrough out of the top was observed. Pump directions were then reversed and fluid is pumped until the sample reached a fluid pressure of 15 MPa. Valves were attached to

Figure 6.19: The endcaps used in the extension tests are able to support differential stresses, such that the maximum stress is the confining stress. Total assembly height is approximately 20 inches tall.

the top and bottom inlets to the pressure vessel, to allow for the simultaneous dropping of fluid pressure to atmospheric pressure at both ports.

6.9.3 Testing Results

The design dictates that both the fluid pressure at the end caps and the axial stress are dropped simultaneously. As mentioned above this is not possible with the available equipment, thus we use the slower fluid equilibrium time to adjust for this. Fluid pressure is always dropped first and then the stress is dropped. The duration between the drops usually took about a second. A plot of fluid pressure, confining pressure, and axial stress, vs. time is presented

Figure 6.20: Pressure vessel and load frame used for generating hydraulic fractures. Tubing on right hand side allows for the simultaneous dropping of fluid pressure at top and bottom end caps.

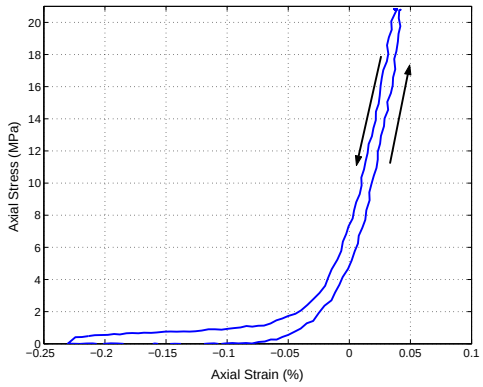

Figure 6.21: A plot of percent axial strain vs. axial stress for a dry extensional test. A small amount of elastic strain takes place as the axial stress is dropped. Arrows indicate unloading and reloading of the speciment. A small amount of hysteresis is observed.

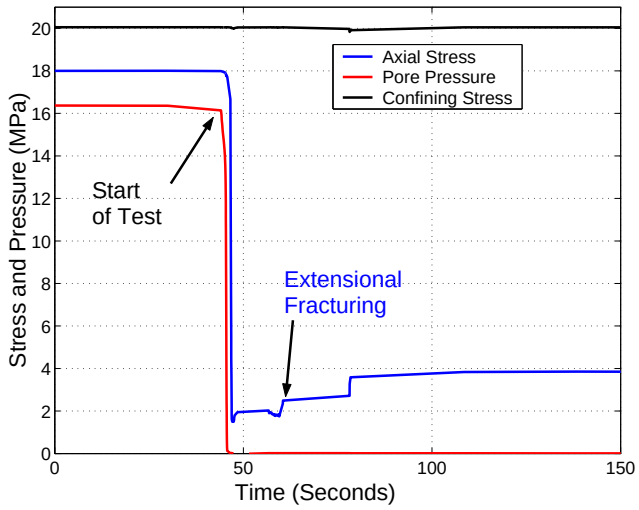

Figure 6.22: A plot of pore pressure, confining pressure, and axial stress, vs. time shows the relative timing of dropping the fluid pressure and the axial stress. Two prominent increases in axial stress after the start of the test mark the extensional fracturing and the slippage of a major extension fracture. A dip in the confining stress is coincident with the slippage due to perturbation of the confining fluid.

in Figure 6.22. Before the fluid pressure is dropped at the end caps, the values are holding steady. After the fluid pressure is vented to the atmosphere, the axial stress is lowered. This reduction is stress was achieved by moving the loading piston away from the sample end caps (about 1 millimeter). After about 10 seconds, the loading ram was moved an additional tenth of a millimeter. Soon after. a sharp jump in axial stress occurred and marked the time at which the rock fractured in extension. Draining of fluid out of the rock and straining of the rock resulted in an increase in axial stress. The additional increase in axial stress resulted from the rock failing in shear. As the rock failed in shear, the confining fluid pressure was perturbed slightly and a small

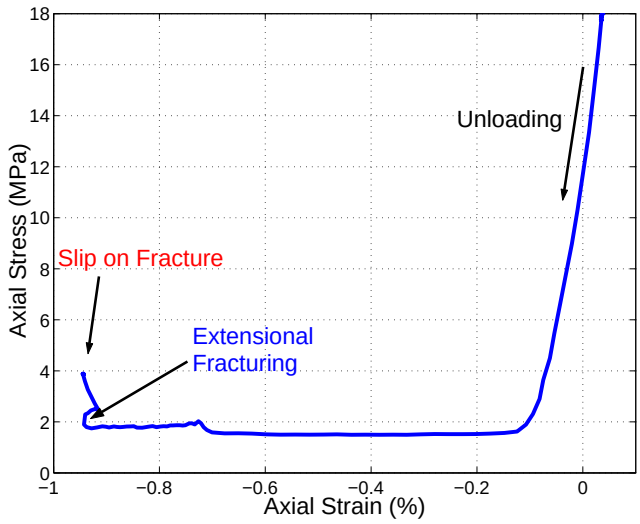

Figure 6.23: As the sample is unloaded, measurable extension (negative strain) of the rock occurs. The strain in the fluid saturated test is 4 times greater than the dry test. A sharp increase in the axial stress marks the time where the extension fractures were formed.

dip in confining pressure was coincident with the second jump in axial stress. The rock was allowed to drain for 4 hours before the sample assembly was removed from the pressure vessel.

A plot of axial stress vs. axial strain is given in Figure 6.23 to highlight the above-described features of the test. This plot looks similar to the dry test, but 4 times more strain took place in the saturated test. This was expected because the fluid pressure contributes to the strain as the fluid drains toward the boundaries. At -0.7% axial strain, a jump in the axial stress signifies the contribution of fluid drainage to the axial strain of the specimen. At -0.9% axial strain the platen was backed off slightly to decrease the axial load, indicated by a drop in stress, and soon afterward a sudden increase in stress

represented an extension of the specimen interpreted as the formation of fractures. An increase in axial strain also marked this event. At the end of the test, an increase with axial stress and slight extension marks the time of shearing of the extension fracture. A plot of axial stress vs. lateral strain (Figure 6.25) also indicates an expansion (negative strain) of the rock coincident with the timing of the shear fracture. The macroscopic feature is shown in Figure 6.24. The initial extension fracture was angled relative to the long axis of the specimen, creating a component of shear along its surface. Even though the confining pressure was acting equally on all sides of the rock, this angle was large enough to cause slip on the fracture plane. In addition to the macroscopic fractures, a significant amount of microscopic damage was observed in the rock. A series of extension cracks perpendicular to the fluid pressure gradient were present (Figure 6.26). This orientation is coincident to the major mechanical anisotropy (and heterogeneity) in the rock, the bedding planes. The bedding planes are at a high angle to the long axis of the specimen (roughly 80º% to the vertical). Observations in thin section suggest that these planes may be the areas where the fractures are localized. Brazilian style extension tests performed to isolate the strength of the bedding planes indicate that the planes may be up to 50 % weaker than the rock between the planes.

6.10 Discussion

The conditions presented in Section 6.4 were successful in producing hydraulic fractures in numerical simulations and in laboratory experiments. Despite this fact, it is unclear whether the existence of elevated pore fluid pressure (i.e. static pressure) or fluid pressure gradients are responsible for

Figure 6.24: Generation of a shear fracture along a pre-existing extension fracture is the result of the angle of the extension fracture. The slip on the fracture is limited by the amount of stretching in the jacket of the specimen.

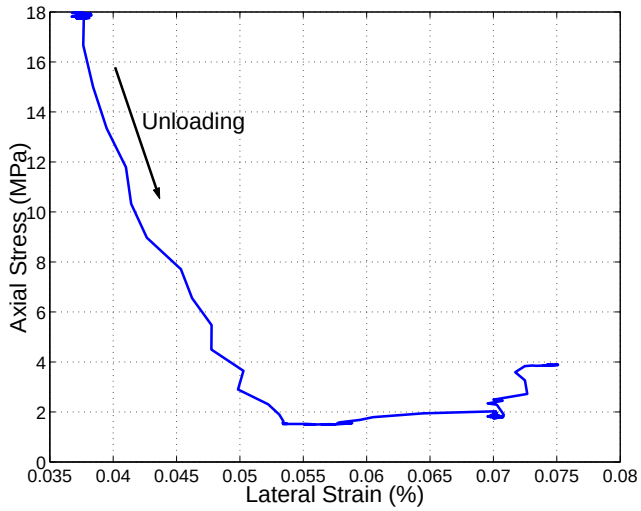

Figure 6.25: As the rock is relieved of axial load, the rock compresses in the lateral direction. This plot of axial stress vs. lateral strain shows this relationship. The fracturing of the sample cause local changes in the amount of compression.

Figure 6.26: Large numbers of extension fractures are observed parallel to bedding and sub-parallel to the fluid pressure gradient. Thin section analysis will be used to quantify the number of fractures in the future.

facilitating fracturing. Analysis of the LBDEM simulations indicate that the bulk loading of fluid flow on the solid matrix was a key factor in producing the observed extension fractures. The LBDEM model does not include static pressure components and will not capture static behavior. Analysis of the experimental data has not yielded convincing support for either fracturing mechanism and it is unclear whether it can be determined from this type of data. It is possible that mechanical heterogeneity and anisotropy are responsible for the location and rough orientation of the numerically simulated and laboratory fractures. More work, particularly in the numerical simulations, on the role of these variables, is necessary. Regardless, both the numerical simulations and experimental results suggest tensile failure as a result of fluid pressure.

In Section 6.3 it is argued that elevated fluid pressure alone is not sufficient to cause fracturing, and that pressure gradients are needed for frac-

turing. In this case the fluid acts against a boundary (which must be virtually impermeable) in which the net force is outward (in tension), resulting in fracturing of the rock. An additional mechanism is a process where flowing fluid imposes a body force in the rock skeleton causing net forcing in the direction of the flow. Flow diverging from a central location in a rock will cause extensional strain about that location. The conditions presented in Section 6.4 included both of these processes, thus separating their effects is impossible. Additional tests designed to isolate these competing effects can be performed numerically or experimentally. A numerical simulation to test the feasibility of static-pressure-induced fracture formation could include the pressurization of a small impermeable cavity in the LBDEM. Such a test, analogous to the hypothesized internal source due to oil/gas generation, does not include fluid flow (and thus bulk forcing) and would provide some insight into the process of fluid pressure-induced fracturing.

It is well known that the processes of rock fracture and fluid flow operate across many ranges of spatial and temporal scales. The ability to scale the results presented here in both space and time is intimately tied to understanding the importance of static pressure versus bulk loading of fluid. Understanding the underlying processes responsible for generating hydraulic fractures and how they scale in space and time is important for any discussion of the broader implications of this work. Once this information is discerned, possibly using the tests described above, the sensitivity of the results to both spatial and temporal scales can be grasped. Additional numerical tests to explore the scaling of the mechanics discussed in this dissertation could also be performed. To investigate spatial scaling larger LBDEM models comprising

similar numbers of elements could be tested under identical fluid pressure gradient conditions. Since the model lacks the ability to capture the static pressure response of materials, it is anticipated that the results of the modeling will scale poorly as the spatial scale is increased. Additionally, some understanding of the scaling properties of the bulk material parameters, such as hydraulic diffusivity, may yield insight into the scaling of the processes involved. Recent reviews by *Bonnet et al.* [2003]; *Neuman and Di Federico* [2003] in the fields of fracture mechanics and hydrogeology respectively suggest that our understanding of the scaling of these systems is improving. The work in this chapter is solely focused on the spatial scale of centimeters (core-scale) and temporal scales of seconds. Until these issues of scales are well-understood, direct comparisons to field examples should initially be limited to cases where similar spatial and temporal scales are present.

6.11 Conclusions

I have shown that fluid pressure gradients may play a significant role in the genesis of natural hydraulic fractures. Theoretical and numerical arguments suggest the importance of properties that govern fluid pressure gradients in rock in both generation and propagation of fractures. Properties that are deemed the most important are the hydraulic diffusivity (controlling timing of fracturing) and rock permeability. Numerical modeling of a newly developed experimental approach to hydraulic fracturing investigates the role of grain-scale processes involved in the genesis and propagation of these fractures. Constructive interference between mechanical anisotropy and hydrologic heterogeneities is important to fracture genesis. Experimental verification of the

conditions used in the numerical tests corroborates the genesis of a hydraulic extension fracture.

Theoretical considerations using poroelasticity and force-balance equations suggest interpreted fracture locations are strongly dependent on the types and locations of boundaries. Force-balance considerations suggest that fluid pressure effects can act to limit the presence of net tensile forces needed for extensional fracture generation. Poroelastic effects, such as the Biot-Willis parameter, in addition to stress coupling (the Poisson effect) may aid in the formation of net tensile forces. Bulk loading induced via high fluid pressure gradients may play an important role in the generation of net tensile forces. These forces arise out of drag of fluid on the bulk medium and indicate that fluid pressure gradients should be quantified for systems of interest. This highlights the importance of measuring fluid permeability of the rocks of interest.

LBDEM numerical models were developed to evaluate fracture genesis as a result of different permeabilities. Although the initial fluid pressure gradients of the systems were identical, local gradients created where initial fractures formed affected the time-evolution of damage in the numerical specimens. The lower permeability models showed more damage and less overall development of the main fractures. The higher permeability models were less sensitive to local fluid pressure gradients and the primary fractures propagated without hindrance. This suggests that local-scale pressure gradients are not that important in driving these fractures to propagate at the macro-scale. These points are also emphasized in the hydrologic heterogeneity study, where 3 types of heterogeneity were imposed on the systems. Heterogeneities oriented

perpendicular to the maximum fluid pressure gradient direction aided the formation of fractures. Heterogeneities with orientations coincident with planes of mechanical weakness also influenced fracture development. Cases where the heterogeneities decreased the local permeability had very little effect on fracture development, whereas heterogeneities that increased the local permeability were very important.

The experimental method presented in Chapter 6 was executed in the laboratory. The test, on a low permeability siliclastic rock (the Abo sandstone), was successful in generating a number of extension fractures throughout the specimen. One large macroscopic fracture was formed and subsequently sheared, as the generated extension fracture was preferentially oriented to the confining stresses. This is consistent with and corroborates the numerical results presented, but also adds the complexity of mechanical anisotropy and heterogeneity. Initial analyses of thin sections suggest that multiple extension fractures are present in the rock sample. Fractures are parallel to bedding planes, and are therefore possibly localized at sites of mechanical anisotropy (and heterogeneity). The planes of bedding are at a high angle to the long axis of the specimen (roughly $80^o\%$ to the vertical). These zones of mechanical weakness could be nucleation sites for fractures. The results of this test will enable us, with confidence, to apply similar tests to rocks of different permeabilities and explore their responses.

These results are of great importance to understanding fracture development in sedimentary basins. This includes the space-time evolution of such systems due to the strong link between hydrological and mechanical processes.

Other instances of importance are faulting problems, where abnormal fluid pressure may play role. The addition of the time dependence of fluid flow may give more insight into the temporal and spatial evolution of fault and damage zones. In addition, problems of fracturing in hot and pressurized hyperthermal aquifers may be addressed by a model similar to that developed above [*Natale et al.*, 1998; *McTigue*, 1986; *Merlani et al.*, 2001; *Natale and Salusti*, 1996].

References

Advani, S., J. Torok, J. Lee, and S. Choudhry, Explicit time-dependent solutions and numerical evaluations for penny-shaped hydraulic fracture models, *Journal of Geophysical Research*, *92*, 8049–8055, 1987.

Advani, S., T. Lee, R. Dean, C. Pak, and J. Avasthi, Consequences of fluid lag in three-dimensional hydraulic fractures, *International Journal of Numerical and Analytical Methods in Geomechanics*, *21*, 229–240, 1997.

Bahat, D., P. Bankwitz, and D. Bankwitz, Preuplift joints in granites: Evidence for subcritical and postcritical fracture growth, *GSA Bulletin*, *115*, 148–165, 2003.

Bear, J., *Dynamics of Fluids in Porous Media*, Dover, New York, 1972.

Berchenko, I., and E. Detournay, Deviation of hydraulic fractures through poroelastic stress changes induced by fluid injection and pumping, *International Journal of Rock Mechanics and Mining Sciences and Geomechanics Abstracts*, *34*, 1009–1019, 1997.

Bessinger, B., N. Cook, L. Myer, S. Nakagawa, K. Nihei, P. Benito, and R. Suarez-Rivera, The role of compressive stresses in jointing on vancouver island, british columbia, *Journal of Structural Geology*, *25*, 983–1000, 2003.

Bonnet, E., O. Bour, N. Odling, P. Davy, I. Main, P. Cowie, and B. Berkowitz, Scaling of fracture systems in geological media, *Review of Geophysics*, *39*, 347–383, 2003.

Boutt, D. F., and B. J. McPherson, Simulation of sedimentary rock deformation: Lab-scale model calibration and parameterization, *Geophysical Research Letters*, *29*, 10.1029/2001GL013,987, 2002.

Bradley, J. S., and D. E. Powley, *Pressure Compartments in Sedimentary Basins: A Review*, Memoir 61: Basin Compartments and Seals, AAPG, Tulsa, OK, 1994.

Bruno, M., and F. Nakagawa, Pore pressure influence on tensile fracture propagation in sedimentary rock, *International Journal of Rock Mechanics and Mining Sciences and Geomechanics Abstracts*, *28*, 261–273, 1991.

Bruno, M., and R. Nelson, Microstructural analysis of the inelastic behavior of sedimentary rock, *Mechanics of Materials*, *12*, 95–118, 1991.

Capuano, R., Evidence of fluid flow in microfractures in geopressured shales, *AAPG Bulletin*, *77*, 1303–1314, 1993.

Cook, B., D. Noble, D. Preece, and J. Williams, Direct simulation of particle

laden fluids, in *Fourth North American Rock Mechanics Symposium.*, A.A. Balkema, Rotterdam, 2000.

Cook, B., D. Noble, D. Preece, and J. Williams, Direct simulation of particle laden fluids, *Journal of Engineering Computations*, in press.

Cook, B. K., A numerical framework for the direct simulation of solid-fluid systems, Doctoral dissertation, Massachusetts Institute of Technology, 2001.

Cruikshank, K., G. Zhao, and A. Johnson, Analysis of minor fractures associated with joints and faulted joints, *Journal of Structural Geology*, *13*, 865–886, 1991.

Cundall, P., A. Drescher, and O. Strack, Numercal experiments on granular assemblies: Measurements and observations, in *Deformation and Failure of Granular Materials*, edited by J. Jenkins and H. Luger, A.A. Balkema, Brookfield, VT, 1982.

Engelder, T., and A. Lacazette, Natural hydraulic fracturing, in *Rock Joints*, edited by N. Barton and O. Stephansson, A.A. Balkema, Brookfield, 1990.

Foxford, K., R. Nicholson, D. Polya, and R. Hebblethwaite, Extensional failure and hydraulic valving at Minas da Panaaqueira, Portugal: evidence from vein spatial distributions, displacements and geometries, *Journal of Structural Geology*, *22*, 1065–1086, 2000.

Hazzard, J., P. F. Young, and S. Maxwell, Micromechanical modeling of cracking and failure in brittle rocks, *Journal of Geophysics Research*, *105*, 16,683–16,697, 2000.

Kranz, R. L., Microcracks in rocks: A review, *Tectonophysics*, *100*, 449–480, 1983.

LHeureux, I., and A. D. Fowler, A simple model of flow patterns in overpressured sedimentary basins with heat transport and fracturing, *Journal of Geophysical Research*, *105*, 23,741–23,752, 2000.

Lorenz, J. C., L. W. Teufel, and N. R. Warpinski, Regional fractures i: A mechanism for the formation of regional fractures at depth in flat-lying reservoirs, *AAPG Bulletin*, *75*, 1714–1737, 1991.

McPherson, B., and J. Bredehoeft, Overpressures in the Uinta basin, Utah: Analysis using a three-dimensional basin evolution model, *Water Resources Research*, *37*, 857–872, 2001.

McTigue, D., Thermoelastic response of fluid-saturated rock, *Journal of Geophysical Research*, *91*, 9533–9542, 1986.

Merlani, A. L., G. Natale, and E. Salusti, Fracturing processes due to temperature and pressure non-linear waves propagating in fluid-saturated porous rocks, *Journal of Geophysical Research*, *106*, 11,067–11,081, 2001.

Natale, G., and E. Salusti, Transient solutions for temperature and pressure waves in fluid saturated rocks, *Geophysical Journal International*, *124*, 15,325–15,338, 1996.

Natale, G., E. Salusti, and A. Troisi, Rock deformation and fracturing processes due to nonlinear shock waves propagating in hyperthermal fluid pressurized domains, *Journal of Geophysical Research*, *103*, 15,325–15,338, 1998.

Neuman, S. P., and V. Di Federico, Multifaceted nature of hydrogeologic scaling and its intepretation, *Review of Geophysics*, *41*, 4–1 – 4–31, 2003.

Neuzil, C., Abnormal pressures as hydrodynamic phenomena, *American Journal of Science*, *295*, 742–786, 1995.

Nur, A., and J. Byerlee, An exact effective stress law for elastic deformation of rock with fluids, *Journal of Geophysical Research*, *76*, 6414–6419, 1971.

Potyondy, D., P. Cundall, and C. Lee, Modeling rock using bonded assemblies of circular particles, in *Rock Mechanics: Tools and Techniques*, edited by Aubertin, Hassani, and Mitri, pp. 1937–1944, A.A. Balkema, Rotterdam, 1996.

Rege, N., Computational modeling of granular materials, Doctoral dissertation, Massachusetts Institute of Technology, 1996.

Renshaw, C. E., and C. F. Harvey, Propagation velocity of a natural hydraulic fracture in a poroelastic medium, *Journal of Geophysical Research*, *99*, 21,667–21,677, 1994.

Rice, J., and M. Cleary, Some basic stress diffusion solutions for fluid-saturated elastic porous media with compressible constituents, *Rev. Geophys. Space Physics*, *14*, 227–241, 1976.

Roberts, S. J., and J. A. Nunn, Episodic fluid explusion from geopressured sediments, *Marine and Petroleum Geology*, *12*, 195–204, 1995.

Secor, D. T., Role of fluid pressure in jointing, *American Journal of Science*, *263*, 633–646, 1965.

Terzaghi, K., *Erdbaumechanik auf Bodenphysikalischer Grundlage*, Deuticke, Leipzig, 1925.

Terzaghi, K., *Theoretical Soil Mechanics*, John Wiley, New York, 1943.

Wang, H., *Theory of Linear Poroelasticity: with Applications to Geomechanics and Hydrogeology*, Princeton University Press, Princeton, New Jersey, 2000.

CHAPTER 7

CONCLUSIONS AND RECOMMENDATIONS

7.1 Conclusions

The work presented in this dissertation focuses on specific problems of coupled fluid-solid mechanics in porous media. These types of problems have been studied for many years with continuum methods. Continuum methods yield insightful information about the macro-scale behavior of systems but rarely provide significant insight into the underlying physics. Detailed understanding of the micromechanical physics will allow the development of better conceptual models of processes and mechanisms. The work presented here is a departure from continuum methods in that I explore the application of discrete physics to coupled fluid-solid mechanics in porous media. The testing and application of these discrete methods have utility outside of fluid-solid mechanics problems. The ability to understand and relate micro-mechanical processes and properties to macroscopic behavior has wide ranging applications. The variability inherent in discrete-based particle models, much like that in nature, is expressed in mathematically simple relationships. Capturing this variability may prove to be the most useful application of these types of methods. This dissertation provides a foundation to apply discrete methods to fluid-solid mechanics problems.

I used discrete methods to examine the behavior of both dry and fluid

saturated rock. My specific interest was in identifying the role of fluids in the genesis of natural hydraulic fractures (NHFs) in the subsurface. Much debate exists over the importance of NHFs in the geologic record, with a considerable amount of effort devoted towards understanding the conditions under which they may form. This effort includes the application of continuum methods to the problem with limited success, typically due to the constraints from over-restricting assumptions or limitations of the numerical analysis. This type of problem is inherently discrete and thus numerical discrete methods are a good tool. This dissertation is the first body of work to use discrete methods to analyze NHFs.

Discrete particle methods are relatively new and less mature than their equivalent continuum based methods, such as the finite element method. In this respect, discrete methods require more testing and understanding to appropriately apply them to realistic problems in geology and hydrology. Many details of the model are still be explored [*Potyondy and Cundall*, In Press]. Issues associated with the appropriate representation and parameterization of dry granular material in the DEM are investigated using a commercial code through a number of specifically designed numerical experiments. The understanding of the dry case is the first step in developing appropriate models of the coupled fluid-solid system.

There are many advantages to using discrete rather than continuum methods to study natural hydraulic fracturing. First, the representation of damage or fracturing in the material is straightforward in discrete methods. In a continuum formulation, a significant amount of computational overhead

is applied to model fracture initiation and propagation. Second, the coupling of fluid flow to solid mechanics with LBDEM allows complex variations in permeability to be represented without relying on assumed porosity-permeability relationships. This is an important aspect, since the time-space evolution of microscale flow paths will locally control fluid pressure values and gradients and thus may impact fracture propagation. Most previous numerical models of NHFs do not treat the dynamics associated with fluid flow. This dissertation is the first modeling of NHFs to resolve the fully coupled physics associated with the initiation and propagation of fluid-induced fractures under geologically consistent boundary and initial conditions.

Experimental analysis of the role of fluid pressure in the initiation and propagation of fractures had been limited to the induced hydraulic fracture. Induced hydraulic fractures differ from NHFs in that the fluid pressure inside the fracture is always greater than fluid pressure within the surrounding matrix. The conditions under which NHFs are thought to form involve a fluid pressure in the incipient fracture that is similar to that outside the fracture. Imposing the conditions to form an NHF in this way are difficult to perform in the laboratory, but a new test relying on the relative speed of fluid flow to stress wave propagation is developed. This test is the first to experimentally demonstrate that natural hydraulic fractures are possible.

7.1.1 Contributions to the Scientific Community

The overarching goal of this dissertation is to develop an understanding of the process of natural hydraulic fracturing and to develop a modeling methodology to simulate the process. The methods in this work used a com-

bination of discrete numerical techniques and focused experimental tests. The contributions of this dissertation can be subdivided into four main parts: (1) contributions to our understanding of the role of particle shapes and initial conditions in discrete-based particle models, (2) development of an application methodology of a discretely coupled fluid-solid model through comparisons to known solutions, (3) development of a laboratory-based test of natural hydraulic fracturing, and (4) numerically exploring the role of microscale properties in controlling the initiation and propagation of natural hydraulic fractures through the numerical replication of the above experimental test.

In the beginning chapters of this dissertation, dry discrete-based models were developed using PFC2D to explore the sensitivity of various model parameters on modeled bulk material properties. The use of non-circular particle shapes (through clustering) allowed a better match to observed laboratory data for a variety of loading conditions. The DEM micro-parameters were found to be fairly non-unique unless care was taken to compare multiple types of laboratory data to elastic and inelastic model behaviors. Initial conditions of the DEM models, through the initial packing and force distribution, have significant impact on resulting behavior. Consistent model development with discrete models requires the careful preparation of the initial model specimen. Regardless of this observation, a number of plausible and justifiable techniques to create initial specimens could be used. A large number of models should be developed and executed to perform statistical calculations. These concepts were incorporated into the development of more models used to explore the micromechanics of natural hydraulic fracturing.

A relatively new model [*Cook*, 2001] based on the coupling between the lattice-Boltzmann method for fluid mechanics and DEM for solid mechanics was compared to basic poroelastic solutions. It is of importance that the selected numerical technique be able to handle the large variations in fluid pressure that are necessary for fracturing. An exploration of errors arising from large pressure gradients in the LB suggest that the error is reasonable for a wide range of pressure gradients. Another important poroealstic phenomenon, the compressibility of the simulated fluid, was determined using a simple test and found to be proportional to the numerical lattice speed. The consolidation of saturated porous media showed the appropriate dynamic and poroelastic response of the LBDEM model. Given that the model solved the fully dynamic equations of motion for both the fluid and solid, direct comparisons with instantaneous undrained responses were not possible. Sensitivity studies, with respect to both fluid and solid wave speed, suggested that in the limit the model can approach an idealized undrained. From this series of tests we conclude that the LBDEM can be safely applied to fluid flow in porous media and can handle dynamic poroelastic problems.

An experimental method was developed to form natural hydraulic fractures under laboratory conditions. The test, on a low permeability siliclastic rock (the Abo sandstone), was successful in generating a number of extension fractures throughout the specimen. One large macroscopic fracture was formed and subsequently sheared, as the generated extension fracture was preferentially oriented to the confining stresses. This is consistent and corroborative with the numerical results presented in Chapter 6. Initial analyses of thin sections suggest that multiple extension fractures are present in the rock

sample. The results of this test will enable us, with confidence, to apply similar tests to rocks of different permeabilities and explore their response.

Numerical tests replicating the above experimental setup indicated that fluid pressure gradients play a significant role in the genesis of natural hydraulic fractures. Theoretical arguments also suggested a strong role of properties that govern fluid pressure gradients in rock. Properties that are deemed most important are the hydraulic diffusivity (controls timing) and related rock permeability and storage. The conceptualization of boundary conditons for the problem of interest is of utmost importance. In tests with varying permeability, the initial fluid pressure gradient of the systems were identical, but the local gradients created when initial fractures form played an important role in the time-evolution of damage in the numerical specimens. The lower permeability models show more damage and less overall development of the main fractures. The higher permeability models were less sensitive to the local gradients and the main fractures propagated without hindrances. This suggests that local scale pressure gradients under these conditions are not important in driving these fractures to propagate at the macro-scale. Constructive interference of mechanical and hydrologic heterogeneities also plays a role in the genesis of fractures. Situations with heterogeneities that are oriented perpendicular to the maximum fluid pressure gradient direction aided the formation of fractures. Heterogeneities with orientations coincident to planes of mechanical weakness also influenced fracture development. Cases where the heterogeneities decreased the local permeability had little effect on fracture development, whereas heterogeneities that increased the local permeability had major effects on fracture development. These results suggest that rocks with higher permeability (and

thus higher hydraulic diffusivity) should have fewer, more developed fractures with larger spaces between them. Lower permeability (and thus lower hydraulic diffusivity) rocks will have many smaller, less developed fractures with smaller spacing between them. Strong hydrologic heterogeneities in rock will serve to assist or inhibit fracture development depending on whether they increase or decrease the local permeability.

The dissertation provides traditional hydrogeologic contexts and interpretations of results, but these can be misleading since the models utilized in the work are founded on micro-scopic phenomenon and not continuum behavior. Microscopic properties are more fundamental, are not subjected to REV constraints, and are easily observed in the LBDEM model. Despite this, the quantification of these parameters is not straightforward. For example, pore shapes and grain shapes are extremely challenging and complex to quantify and qualitative descriptions referring to the distribution of voids and grains are relied upon. Here I briefly review some of the important conclusions of the work with respect to micromechanical concepts and constructs. As described in the introduction there are a set of micromechanical processes that give rise to the bulk hydrogeologic behavior observed in the laboratory and the field. The most important micromechanical parameters are the amount, shape, and distribution of the pore space (including pore throat size), fluid compressibility, grain compressibility (stiffness), and porous matrix compressibility. Results from the porous media consolidation problem suggested that the speed of pressurization is a strong function of the grain and matrix compressibility. In numerically modeled hydraulic fractures, the amount of pore space and the size of the pore throat controled the timing of the fracturing. Fluid pressure gradients in the

low permeability models, the result of smaller pore throat sizes, controled the time necessary for the fluid to reach the boundaries of the model.

7.2 Limitations and Future Work

Limitations of the analyses in this work are briefly discussed in the context of future improvements to the techniques and methods used within the dissertation. Recommendations for future analyses lie in two categories. The first, are improvements to the analyses themselves, such as the extension of the methods to 3-dimensions. The second are extensions of the work to a broader category of problems and conditions, including both experimental and numerical analysis. The application of the numerical techniques discussed within is currently being applied to larger scale problems of sand production. They are anticipated to have applicability to a wide range of problems, the most attractive of them being liquefaction and problems with a significant amount of dynamic motion and multiphase (particle-fluid) interaction.

7.2.1 Limitations

One of the most limiting aspects of the LBDEM modeling scheme is the assumption of a two-dimensional system. However, many fundamental problems can still be addressed. In a compacted or very densely packed two-dimensional assembly of discrete elements, a physically unrealistic situation arises in the form of no connected paths for fluid to flow through. To facilitate the use of fluid coupling in this context, an assumption about the fluid flow paths must be made. This problem has been addressed before for the case of flow network models [*Bruno and Nelson*, 1991; *Bruno*, 1994; *Li and Holt*, 2001]

and continuum Darcy's models [*O'Connor et al.*, 1997]. In both cases, fluid is assumed to flow out of the plane and around solids. In this case, I take a similar approach to *O'Connor et al.* [1997] and assumed that fluid was flowing out the plane. The LB is assumed to only interact with a defined percentage of the discrete elements. This effectively resulted in a smaller radius used to resolve the fluid through the assembly. Changing the "effective" fluid radius resulted in changes in pore throat sizes, pore volumes, and the macroscopic parameters (porosity, permeability, and storage capacity).

Unlike poroelastcity theory, which assumes an instantaneous response of fluid pressure to a change in pore volume, the coupled LBDEM model has a finite response based on the wave speed of the simulated fluid. Simulated fluid wave speeds in the LB technique are much smaller than real fluids and are dependent on the discretization level. Therefore, the response of any assembly to a boundary condition change takes a finite amount of time to reach the maximum fluid pressure. In reality, experimental evidence [*Gunaratne et al.*, 1996] using a dynamically applied stress suggests that the time to reach peak fluid pressure is finite and is on the order of tenths of a second depending on material properties. The two dynamic wave speeds in LBDEM are the solid wave speed and the fluid wave speed. The solid wave speed is a function of element stiffness, whereas the fluid wave speed is related to model viscosity and discretization. The numerical value of fluid wave speed in the LB method is significantly smaller than actual wave speeds in real fluids (Table 5.3). The sensitivity of these two parameters and their pressure response was explored using Terzaghi's consolidation problem in Chapter 5. Results indicated that this assumption was acceptable, but caution should still be used when applying

the this modeling approach to dynamic problems.

In the LBDEM formulation it is assumed that a fluid force is only applied to the discrete elements if the fluid has a non-zero velocity. This implies that static pressure, on the whole, is not captured. Conceptually, issues with this assumption are avoided by treating changes in pressure within the model to be dynamic pressure or changes from a static pressure condition. This was accomplished by setting initial and boundary conditions to effective stress conditions, which was done by taking the total stress and subtracting off the static pressure. This limitation resulted in the poroelastic condition of setting the Biot-Willis coefficient (discussed in Chapter 1) equal to 1.

Although the experimental test was successful, it is still unclear what the underlying mechanism responsible for the generation of the fracture was. Two hypothese remain as to the source of forces responsible for inducing the observed extension fractures. Fluid pressure gradients are a plausible explanation in that they induce net fluid forces on the solid grains and create an extension of the rock. In the numerical model, these are unequivocally the forces responsible for failure, because of the lack of effective stress. In theory, any arbitrary plane of homogeneous and isotropic rock the absence of a fluid pressure gradient causes a zero net fluid force. This implies that the fluid pressure is 100% efficient in counteracting the granular skeleton force. We know that for rocks this is not the case, hence the presence of the Biot-Willis coefficient. Thus it is possible for a net fluid force to exist on the granular skeleton of rock in the absence of a fluid pressure gradient. It is then plausible that the extension of the rock sample (due to the removal of the end load) and con-

tributions from the Biot-Willis will be large enough to initiate and propagate fractures. Without knowledge of Biot-Willis coefficient for the Abo sandstone, calculating this effect is not possible.

The importance of mechanical heterogeneities on fracture initiation is well known. These heterogeneities can take on many forms, such as bedding planes, and can also act as mechanical anisotropies. The bedding planes in the sample of Abo Formation most likely were responsible for determining the location of fracturing. Additional tests on samples of Abo Formation will be performed parallel to bedding to gain a better understanding of these bedding planes.

7.2.2 Future Work

Obvious conceptual issues with the 2D current analyses will be overcome with 3D implementations. With a move to 3D problems, the computational load becomes more burdensome. To maintain a similar type of resolution for the 2D fracturing problems that are presented in this dissertation will require more than 1000 times the computational effort. A 3D framework for the LBDEM is currently being developed. This will allow relaxation of assumptions with respect to the fluid radius and allow us to resolve 3D structures are most assuredly associated with fracturing. As we interpret in naturally formed extension fractures, local deviations of fractures are abundant and may be the result of local stress fields. Work with the 3D implementation will help quantify this for fluid induced fractures. Despite the increased effort, this functionality is not easily modeled with linear elastic fracture mechanics-based codes.

The extension of the LBDEM code to multiphase fluid flow is of considerable importance when applying the model to the deep subsurface. Most deep aquifers contain some amount of oil and gas and require the consideration of capillarity effects in fluid flow processes. For example, the generation of oil from kerogen (a commonly assumed source of abnormal fluid pressure) will create a multiphase system. In order to understand the fluid dynamics and its resulting effects on the mechanical system, a multiphase flow simulator is needed. The incorporation of multiphase aspects in the LBDEM, in principle, is straightforward. A variety of multiphase LB formulations are currently available. The most challenging aspect is handling capillary forces and the incorporation of those forces into the mechanical framework of DEM. Nonetheless, a wide variety of problems could then be examined with this type of model. Most attractive are some of the problems associated with wormhole development in reactive multiphase flow. These problems are characterized by local regions of non-Darcian flow, which include strong mechanical degradation of the porous media.

The experimental work presented in this dissertation is in the early stages. The demonstration of the proof of concept of the technique will allow us to explore more rocks and different types of rocks. A test design will be developed to help discern the role of fluid pressure gradients versus static pressure in the genesis of fractures. More detailed measurements of the poroelastic parameters, such as the Biot-Willis coefficient, of the tested rocks will be made to enable further analysis of test results. The use of acoustic emissions to monitor rock fracture through time during the experimental test will allow us to constrain the timing of fracturing versus the time characteristics of fluid flow.

This will enable insight into the extension fracturing process and may provide more details on the fluid pressure gradients in rock extension.

The ability to scale (both spatially and temporally) the results of this chapter is intimately tied with understanding the role of static pressure vs. bulk loading of fluid on fracture genesis. Once this information is discerned, possibly using the tests described above, the sensitivity of the results to both spatial and temporal scales can be grasped. Additional numerical tests to explore the scaling of the mechanics argued in this dissertation could also be performed. To investigate spatial scaling, larger LBDEM of the models presented in Chapter 6 comprising similar numbers of elements could be executed under identical fluid pressure gradient conditions. Since the model lacks the ability to capture the static pressure response of materials, it is anticipated that the results of the modeling will scale poorly as the spatial scale is increased. Further work on understanding the importance of the different parameters in the LBDEM model, such as element stiffness and the effective radius, on resulting behavior may lead to insight into model scaling parameters

Additionally, some understanding of the scaling properties of the bulk material parameters, such as hydraulic diffusivity, may help discern the scaling of the processes involved. Recent reviews by *Bonnet et al.* [2003]; *Neuman and Di Federico* [2003] in the fields of fracture mechanics and hydrogeology respectively, suggest that our understanding of the scaling of these systems is drastically improving.

Further testing of the Abo formation will yield details on the control of bedding planes on fracture genesis. Testing the rock with the parallel-to-

bedding direction oriented with the major fluid pressure gradient will allow an understanding of the range of applicability of the experimental setup. With the ultimate goal of probing the relative importance of mechanical heterogeneities vs. hydrologic heterogeneities in fluid induced fracture genesis, a suite of experiments of rocks with varying degrees of permeability and storage will be investigated. With this knowledge a better conceptual model of fracture orientations and distributions will be gleaned. Also relevant are the implications that this information may have on fault and fracture zones, where the spatial distribution of fractures and their apertures will have some control on fault behavior.

The quantitative relationships between microscopic processes and macroscopic phenomena in hydrogeology, such as hydraulic diffusivity, remain ambiguous. A significant amount of work is now being performed in an attempt to quantify the microscopic parameters that are relevant for observed macroscopic permeability variations. It is anticipated that some of the same microscopic controls on permeability will be important for understanding storage capacity and associated parameters that control transients in fluid pressure in hydrogeology. One avenue of future research would be to further study the microscopic controls on storage capacity and hence hydraulic diffusivity. Current microscopic techniques, such as laser confocal microscopy, could be used to observe fluid pressure transients (through the displacement of rock framework) in small sections of rock. Ultimately, information from these and other methods could be used to develop improved conceptual models, scaling relationships, and the parameterization of discrete models such as the LBDEM.

References

Bonnet, E., O. Bour, N. Odling, P. Davy, I. Main, P. Cowie, and B. Berkowitz, Scaling of fracture systems in geological media, *Review of Geophysics*, *39*, 347–383, 2003.

Bruno, M., Micromechanics of stress-induced permeability anisotropy and damage in sedimentary rock, *Mechanics of Materials*, *18*, 31–48, 1994.

Bruno, M., and R. Nelson, Microstructural analysis of the inelastic behavior of sedimentary rock, *Mechanics of Materials*, *12*, 95–118, 1991.

Cook, B. K., A numerical framework for the direct simulation of solid-fluid systems, Doctoral dissertation, Massachusetts Institute of Technology, 2001.

Gunaratne, M., M. Ranganath, S. Thilakasiri, G. Mullins, P. Stinnette, and C. Kuo, Study of pore pressures induced in laboratory dynamic consolidation, *Computers and Geotechnics*, *18*, 127–143, 1996.

Li, L., and R. Holt, Simulation of flow in sandstone with fluid coupled particle model, in *Proceedings of the 38th U.S. Rock Mechanics Symposium: Rock Mechanics in the National Interest*, edited by D. Elsworth, J. P. Tinucci, and A. Heasley, pp. 511–516, A.A. Balkema, Rotterdam, 2001.

Neuman, S. P., and V. Di Federico, Multifaceted nature of hydrogeologic scaling and its intepretation, *Review of Geophysics*, *41*, 4–1 – 4–31, 2003.

O'Connor, R., J. Torczynski, D. Preece, J. Klosek, and J. Williams, Discrete element modeling of sand production, *International Journal of Rock Mechanics and Mining Sciences*, *34*, 231, 1997.

Potyondy, D. O., and P. A. Cundall, A bonded-particle model for rock, *International journal of rock mechanics and mining sciences*, In Press.